

THESIS FOR THE DEGREE OF DOCTOR OF PHILOSOPHY

**Synthesis and Characterization of Acceptor Polymers for All-Polymer Solar Cells and Photodetectors**

ZHAOJUN LI



Department of Chemistry and Chemical Engineering

CHALMERS UNIVERSITY OF TECHNOLOGY

Gothenburg, Sweden 2018

# **Synthesis and Characterization of Acceptor Polymers for All-Polymer Solar Cells and Photodetectors**

ZHAOJUN LI

© ZHAOJUN LI, 2018.

ISBN 978-91-7597-706-5

Doktorsavhandlingar vid Chalmers tekniska högskola

Ny serie nr 4387

ISSN 0346-718X

Division of Applied Chemistry

Department of Chemistry and Chemical Engineering

Chalmers University of Technology

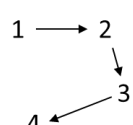
SE-412 96 Gothenburg

Sweden

Telephone + 46 (0)31-772 1000

Cover:

1. Actual all-PSC device picture ( the size is seen by reference to the coin)
2. Schematic illustration of conventional device structure
3. Simplified schematic illustration of active layer morphology, charge generation and charge transprot
4. Ideal molecular packing



Chalmers Reproservice  
Göteborg, Sweden 2018

# Synthesis and Characterization of Acceptor Polymers for All-Polymer Solar Cells and Photodetectors

ZHAOJUN LI

Department of Chemistry and Chemical Engineering  
CHALMERS UNIVERSITY OF TECHNOLOGY  
Gothenburg, Sweden

## ABSTRACT

The development of polymer semiconductors has become an important topic due to its advantages of low cost, easy fabrication, light weight, and capability to fabricate flexible large-area devices. For example, as the need for new clean energy sources is increasing, polymer solar cells (PSCs) are being developed rapidly and becoming a promising alternative to silicon solar cells. This thesis focuses on the applications of polymer semiconductors in two active fields of polymeric optoelectronics: PSCs and polymer photodetectors (PPDs). Heretofore, PSCs and PPDs were fabricated commonly using a blend of a conjugated polymer and a fullerene derivative as the active layer. Despite the wide use of fullerene derivatives, their limitations such as low absorption, morphological instability, and high costs, created a strong need to develop new acceptor materials. Therefore, all-polymer solar cells (all-PSCs) and all-polymer photodetectors (all-PPDs) based on a blend of conjugated polymers acting as both electron donor and acceptor are being actively pursued.

We have made concerted efforts to prepare high-performance all-PSCs and all-PPDs, by specifically modifying the acceptor molecular structure, and rationally choosing suitable donor and acceptor combinations. This aspect of our work had two main facets:

- Material synthesis: the design, synthesis and characterization of novel acceptor polymers.
- Device engineering: the fabrication, optimization and characterization of all-PSCs and all-PPDs.

Our efforts in the design of novel acceptor polymers focused on crystallinity and energy level engineering via structural modifications like backbone and sidechain modulation. Also, a comprehensive comparison of the characteristic functional properties of acceptor polymers was undertaken. Binary devices using donor and acceptor polymers with complementary absorption or suitable energy level offset, and ternary devices were studied to further improve the performance of all-PSCs. High efficiencies of 8.0% and 9.0% are achieved for binary all-PSCs and ternary all-PSCs, respectively. Additionally, high-performance all-PPDs exhibiting low dark current density ( $J_d$ ) and high responsivity ( $R$ ) under -5 V bias were demonstrated. Based on the results presented herein, we are now moving closer to understanding the correlation between the polymer structure, blend morphology, and device performance. This thesis also provides a guideline for developing all-PSCs and all-PPDs with improved performance.

**Keywords:** conjugated polymers, all polymer solar cells, all polymer photodetectors, morphology, charge recombination

## LIST OF PUBLICATIONS

---

This thesis is based on the following scientific papers, referred to by their Roman numerals in the text.  
The papers are appended at the end of the thesis.

**Paper I. High Performance All-Polymer Solar Cells by Synergistic Effects of Fine-Tuned Crystallinity and Solvent Annealing**

Zhaojun Li, Xiaofeng Xu, Wei Zhang, Xiangyi Meng, Wei Ma, Arkady Yartsev, Olle Inganäs, Mats. R. Andersson, René A. J. Janssen, Ergang Wang  
*Journal of the American Chemical Society*, 2016, 138(34), 10935-10944

**Paper II. High-Photovoltage All-Polymer Solar Cells Based on a Diketopyrrolopyrrole-Isoindigo Acceptor Polymer**

Zhaojun Li, Xiaofeng Xu, Wei Zhang, Zewdneh Genene, Wendimagegn Mammo, Arkady Yartsev, Mats R. Andersson, René A. J. Janssen, Ergang Wang  
*Journal of Materials Chemistry A*, 2017, 5, 11693-11700

**Paper III. High-Performance and Stable All-Polymer Solar Cells Using Donor and Acceptor Polymers with Complementary Absorption**

Zhaojun Li, Wei Zhang, Xiaofeng Xu, Zewdneh Genene, Dario Di Carlo Rasi, Wendimagegn Mammo, Arkady Yartsev, Mats. R. Andersson, René A. J. Janssen, Ergang Wang  
*Advanced Energy Materials*, 2017, 7, 1602722

**Paper IV. 9.0% Power Conversion Efficiency from Ternary All-Polymer Solar Cells**

Zhaojun Li, Xiaofeng Xu, Wei Zhang, Xiangyi Meng, Zewdneh Genene, Wei Ma, Wendimagegn Mammo, Arkady Yartsev, Mats. R. Andersson, René A. J. Janssen, Ergang Wang  
*Energy & Environmental Science*, 2017, 10, 2212-2221

**Paper V. 8.0% Efficient All-Polymer Solar Cells with High Photovoltage of 1.1 V and Internal Quantum Efficiency near Unity**

Xiaofeng Xu, Zhaojun Li, Wei Zhang, Xiangyi Meng, Xianshao Zou, Dario Di Carlo Rasi, Wei Ma, Arkady Yartsev, Mats. R. Andersson, René A. J. Janssen, Ergang Wang  
*Advanced Energy Materials*, 2018, 8, 1700908

**Paper VI. High-Performance All-Polymer Solar Cells Based on Fluorinated Naphthalene Diimide Acceptor Polymers with Fine-Tuned Crystallinity and Enhanced Dielectric Constants**

Xiaofeng Xu, Zhaojun Li, Junke Wang, Baojun Lin, Wei Ma, Mats. R. Andersson, René A. J. Janssen, Ergang Wang  
*Nano Energy*, 2018, 45, 368-379

**Paper VII. High-Performance Broadband All-Polymer Photodetectors with Low Acceptor Content**

Zhaojun Li, Giulio Simone, Xiaofeng Xu, Dario Di Carlo Rasi, Mats. R. Andersson, René A. J. Janssen, Ergang Wang  
*Manuscript*

## **CONTRIBUTION REPORT**

---

Paper I. Performed all the synthesis and characterization of acceptor polymers, fabrication and characterization of solar cell devices (except GIWAXS, R-SoXS and TRPL measurements), and wrote the manuscript together with co-authors. Data was analyzed together with Xiaofeng Xu.

Paper II. Performed all the synthesis and characterization of acceptor polymers, fabrication and characterization of solar cell devices (except TRPL measurements), and wrote the manuscript together with co-authors.

Paper III. Performed all the fabrication and characterization of solar cell devices (except absolute fluorescence quantum yield and TRPL measurements), and wrote the manuscript together with co-authors. The synthesis and characterization of acceptor polymers and data analysis were completed together with Xiaofeng Xu. The IQE measurements were conducted together with Dario Di Carlo Rasi (TU/e).

Paper IV. Performed all the fabrication and characterization of solar cell devices (except GIWAXS, R-SoXS and TRPL measurements), and wrote the manuscript together with co-authors. The synthesis and characterization of acceptor polymers, and data analysis were completed together with Xiaofeng Xu.

Paper V. Co-author. Performed all the fabrication and characterization of solar cell devices (except GIWAXS, R-SoXS and TRPL measurements). Contributed in the polymer characterization, data analysis and manuscript writing. The IQE measurements were conducted together with Dario Di Carlo Rasi (TU/e).

Paper VI. Co-author. Performed all the fabrication and characterization of solar cell devices (except GIWAXS measurements). Contributed in the polymer characterization and data analysis. The impedance measurement was performed together with Junke Wang (TU/e).

Paper VII. Performed all the fabrication and characterization of photodiode devices and wrote the manuscript. TPC measurement was carried out together with Giulio Simone (TU/e).

## PUBLICATIONS NOT INCLUDED IN THE THESIS

---

**Paper A. Effects of Side Chain Isomerism on the Physical and Photovoltaic Properties of Indacenodithieno[3,2-*b*]thiophene–quinoxaline Copolymers: toward a Side Chain Design for Enhanced Photovoltaic Performance**

Xiaofeng Xu, Zhaojun Li, Olof Bäcke, Kim Bini, David I. James, Eva Olsson, Mats R. Andersson, Ergang Wang

*Journal of Materials Chemistry A*, 2014, 2, 18988-18997

**Paper B. Molecular Doping and Trap Filling in Organic Semiconductor Host–Guest Systems**

Guangzheng Zuo, Zhaojun Li, Olof Andersson, Hassan Abdalla, Ergang Wang, Martijn Kemerink

*The Journal of Physical Chemistry C*, 2017, 121(14), 7767-7775

**Paper C. High Seebeck Coefficient and Power Factor in n-Type Organic Thermoelectrics**

Guangzheng Zuo, Zhaojun Li, Olof Andersson, Ergang Wang, Martijn Kemerink

*Advanced Electronic Materials*, 2018, 4, 1700501

**Paper D. Energy-Effectively Printed All-Polymer Solar Cells Exceeding 8.61% Efficiency**

Yuanbao Lin, Sheng Dong, Zhaojun Li, Wenhao Zheng, Junyu Yang, Alei Liu, Wanzhu Cai, Feng Liu, Yufeng Jiang, Thomas P. Russell, Fei Huang, Ergang Wang, Lintao Hou

*Nano Energy*, 2018, 46, 428-435

## ABBREVIATIONS AND ACRONYMS

---

AFM	Atomic Force Microscopy
All-PSC	All-Polymer Solar Cell
All-PPD	All-Polymer Photodetector
BDT	Benzodithiophene
BHJ	Bulk-Heterojunction
CB	Chlorobenzene
CF	Chloroform
CN	1-Chloronaphthalene
CV	Cyclic Voltammetry
d	Film thickness
DIO	1,8-Diiodooctane
DPE	Diphenyl Ether
DPP	Diketopyrrolopyrrole
D-A	Donor-Acceptor
DSC	Differential Scanning Calorimetry
D*	Specific Detectivity
EA	Electron Affinity
EQE	External Quantum Efficiency
ETL	Electron Transporting Layer
$E_{\text{ox}}$	Oxidation Potential
$E_{\text{red}}$	Reduction Potential
$E_g$	Electronic Energy Bandgap
$E_g^{\text{opt}}$	Optical Energy Bandgap
FF	Fill Factor
GIWAXS	Grazing-Incidence Wide-Angle X-ray Scattering
GPC	Gel Permeation Chromatography
HTL	Hole Transporting Layer
HOMO	Highest Occupied Molecular Orbital
h	Plank constant
IID	Isoindigo
IP	Ionization Potential
IQE	Internal Quantum Efficiency
ITO	Indium Tin Oxide
I	Incident Light Intensity
$I_{\text{ph}}$	Photocurrent
J	Current Density
$J_d$	Dark Current Density
$J_{\text{sc}}$	Short-Circuit Current Density
$J_{\text{ph}}(\lambda)$	Photocurrent Density
$J_{\text{sat}}$	Saturated Photocurrent Density
$J_{\text{tmax}}$	Theoretical Maximum Photocurrent Density

$L_{in}(\lambda)$	Incident Light Intensity
LUMO	Lowest Unoccupied Molecular Orbital
LiF	Lithium Fluoride
$L_D$	Exciton Diffusion Length
MEH-PPV	Poly[2-methoxy-5-(2-ethylhexyloxy)-1,4-phenylenevinylene]
$M_n$	Number-Average Molecular Weight
$M_w$	Weight -Average Molecular Weight
NDI	Naphthalene Diimide
NEP	Noise Equivalent Power
NIR	Near Infrared
<i>o</i> -DCB	1,2-Dichlorobenzene
PCE	Power Conversion Efficiency
PC <sub>71</sub> BM	[6,6]-Phenyl-C <sub>71</sub> -Butyric Acid Methyl Ester
PD	Polydispersity Index
PDI	Perylene Diimide
PL	Photoluminescence
PPD	Polymer Photodetector
PSC	Polymer Solar Cell
Pd <sub>2</sub> (dba) <sub>3</sub>	Tris(dibenzylideneacetone)dipalladium(0)
P( <i>o</i> -tol) <sub>3</sub>	Tri( <i>o</i> -tolyl)phosphine
PEDOT:PSS	Poly(3,4-ethylenedioxythiophene):Poly(styrenesulfonate)
q	Elementary Charge of the Electron
R-SoXS	Resonant Soft X-ray Scattering
$R$	Responsivity
SA	Solvent Annealing
SCLC	Space Charge Limited Current
SWV	Square-Wave Voltammetry
TDQ	Thiadiazoloquinoxaline
TEM	Transmission Electron Microscopy
UV-Vis	Ultraviolet-Visible
$V_{oc}$	Open-Circuit Voltage
$V$	Applied Voltage
$V_{bi}$	Built-in Voltage
$\nu$	The Frequency of Light
$\alpha$	Absorption Coefficient
$\epsilon_0$	Absolute Dielectric Constant of Vacuum
$\epsilon_r$	Dielectric Constant of Polymers
$\mu_e$	Electron Mobility
$\mu_h$	Hole Mobility
$\eta_{BR}$	Bimolecular Recombination Efficiency
$\eta_{GR}$	Geminate Recombination Efficiency
$\eta_T$	Total Recombination Efficiency

# Contents

---

ABSTRACT.....	III
LIST OF PUBLICATIONS .....	IV
CONTRIBUTION REPORT .....	V
PUBLICATIONS NOT INCLUDED IN THE THESIS .....	VI
ABBREVIATIONS AND ACRONYMS .....	VII
1 Introduction .....	1
1.1 A Brief Overview of Semiconducting Polymers.....	1
1.2 A Brief Overview of All-Polymer Solar Cells and Photodetectors .....	2
1.3 Aim and Outline of the Thesis .....	3
2 Conjugated Polymers.....	5
2.1 Optical and Electrochemical Properties .....	5
2.2 Molecular Design towards Energy Bandgap Control .....	6
2.3 Synthesis of Conjugated Polymers.....	8
2.3.1 Stille and Suzuki Reactions .....	9
3 All-Polymer Solar Cells and Photodetectors .....	11
3.1 Working Principle and Device Structures .....	11
3.2 Figures of Merit.....	13
3.2.1 Figures of merit for PSCs .....	13
3.2.2 Figures of merit for PPDs .....	16
3.3 Development of All-PSCs.....	17
3.4 Development of All-PPDs.....	20
3.5 Charge Recombination.....	21
3.5.1 Geminant Recombination.....	21
3.5.2 Non-geminate Recombination .....	22
3.6 Morphology Engineering .....	23
3.6.1 Desired Active Layer Morphology .....	23
3.6.2 Optimization of Active Layer Morphology .....	24
3.7 Active Layer Polymers Design Criteria .....	26
4 Synthesis and Characterization of Naphthalene Diimide-based Acceptor Polymers for All-PSCs .....	27
4.1 Background and Motivation.....	27
4.2 Acceptor Polymers Synthesis and Characterization.....	28
4.3 Results and Discussion on All-PSCs.....	34
4.3.1 Crystallinity Modification Approach to Improve the FF.....	34

---

4.3.2	The Complementary Absorption Approach to Increase the $J_{sc}$ .....	38
4.3.3	Energy Level Manipulation to Improve the $V_{oc}$ .....	41
4.3.4	Ternary Approach .....	43
5	Synthesis and Characterization of Diketopyrrolopyrrole- and Isoindigo-based Acceptor Polymers for All-PSCs.....	47
5.1	Background and Motivation.....	47
5.2	Acceptor Polymers Synthesis and Characterization.....	47
5.3	Results and Discussion on All-PSCs.....	49
5.3.1	All-PSCs based on acceptor polymers PIID-PyDPP and PTDPP-PyDPP .....	50
5.3.2	All-PSCs based on the acceptor polymers PPyDPP-FT and PIID-FT.....	52
5.3.3	All-PSCs based on the acceptor polymers PNDI-DPP and PTNDI-TDPP .....	53
6	Synthesis and Characterization of Thiadiazoloquinoxaline-based Acceptor Polymers for All-PSCs and All-PPDs .....	57
6.1	Background and Motivation.....	57
6.2	Acceptor Polymers Synthesis and Characterization.....	57
6.3	Preliminary Evaluation in All-PSCs .....	60
7	Characterization of Naphthalene Diimide-based Acceptor Polymers for All-PPDs .....	63
7.1	Background and Motivation.....	63
7.2	Reduction of Dark Current.....	63
7.3	Comparison Between All-Polymer- and Fullerene-based Photodetectors.....	64
8	Summary and Outlook.....	67
9	Methods .....	71
9.1	All-PSCs and All-PPDs Fabrication .....	71
9.2	EQE Measurements .....	72
9.3	SCLC Mobility Measurements .....	72
9.4	Photon Absorptance Simulation.....	72
References.....		74
Appendix I .....		82
Appendix II .....		83
Acknowledgements.....		84

# 1 Introduction

---

Knowledge of the relation between light and electricity has existed since the eighteenth century. However, widespread use of the interaction of light with electricity has become practical only within the last few decades, primarily due to the development of advanced semiconductor materials technology.<sup>[1]</sup> Since the climate change associated with the use of fossil fuels and the looming worldwide energy crisis has spurred the investment in renewable energy harvesting, the development of solar cells (SCs) has gained a lot of attraction. Hardly surprising, since the Sun is the most abundant energy source.<sup>[2]</sup> Moreover, as the need of light detection applications, such as optical measurements, sensing (remote control, biology and environmental monitoring), and imaging (digital cameras) is increasing in our technological society, research towards the development of photodetectors (PDs) is also increasing.<sup>[3]</sup>

Compared to inorganic semiconductor materials like silicone, polymer semiconductors bear the potential to develop a long-term technology that is economically viable for large-area production. The desired flexibility of polymeric materials also provides the possibility of using flexible plastic substrates in an easily scalable high-speed printing process.<sup>[4]</sup> Polymeric materials can possess an extremely high optical absorption coefficient ( $\alpha$ ), which offers the possibility of very thin SC production.<sup>[5]</sup> Moreover, the low processing temperature and thin device structure can further reduce the cost of semiconductor devices, resulting in a much shorter energy pay-back time.<sup>[6]</sup> As the need of novel clean energy sources is increasing, polymer solar cells (PSCs) are developing rapidly and becoming a promising alternative to silicon solar cells. The power conversion efficiency (PCE) of the single junction PSCs has reached 11%-13%.<sup>[7]</sup> Polymeric semiconductors are also very appealing for light detection applications as their spectral sensitivity can be tuned panchromatic or selective to specific wavelength in the region from UV to near infrared (NIR) light, and considerable improvements have been achieved in polymer photodetectors (PPDs).<sup>[8]</sup> Notably, the progress in PPDs is strongly coupled to the development in PSCs field, particularly in the use of new active layer materials and device structures.<sup>[9]</sup>

## 1.1 A Brief Overview of Semiconducting Polymers

A semiconducting material has an electrical conductivity value falling between that of a conductor, such as copper and gold, and an insulator, such as glass. Traditionally, polymers are considered as insulators. However, in 1977, Heeger *et al.* reported a tremendous increase in the conductivity of polyacetylene (Scheme 2.1) by doping the polymer with iodine.<sup>[10]</sup> This discovery changed the traditional concept, and Heeger was one of the recipients of the 2000 Nobel Prize in Chemistry for this achievement. Since then, the research in the field of conjugated semiconducting polymers has grown considerably. A conjugated polymer is a macromolecule with the main chain consisting of a sequence of conjugated

double or triple bonds.<sup>[11]</sup> Electron delocalization along the conjugated backbone is responsible for the semiconducting property of these materials. Some examples of conjugated polymer structures are illustrated in Figure 1.1.

Conjugated polymers combine the optoelectronic properties of conventional semiconductors with the excellent mechanical and processing properties of “plastic” materials. Additionally, they possess an unprecedented flexibility in their syntheses, allowing for alteration of a wide range of properties, such as electronic energy bandgap ( $E_g$ ), molecular orbital energy level as well as structural properties. However, conjugated polymers bear low dielectric constants ( $\epsilon_r$ ), compared to inorganic semiconducting materials, leading to increased charge recombination and energy loss. Moreover, an electron-withdrawing material working as electron acceptor is required in PSC and PPD devices to facilitate the generation of photocurrent, which further complicates the process. The structural aspects of conjugated polymers are described in Chapter 2, and detailed working mechanism of PSCs and PPDs is presented in Chapter 3.

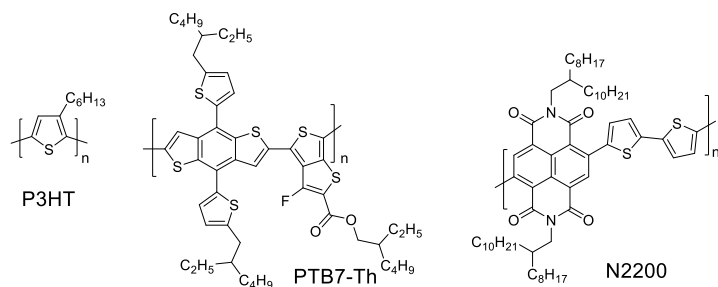


Figure 1.1 Examples of classic conjugated conducting polymer chemical structures.

## 1.2 A Brief Overview of All-Polymer Solar Cells and Photodetectors

Among the various types of PSCs and PPDs, the most widely studied devices consist of a bulk heterojunction (BHJ) structure, in which a conjugated donor polymer is mixed with a fullerene derivative such as [6,6]-phenyl-C<sub>71</sub>-butyric acid methyl ester (PC<sub>71</sub>BM). Despite the attractive properties of fullerene derivatives in PSCs and PPDs, their limitations such as low absorption, morphological instability, and high costs necessitate the development of alternative acceptors to overcome some of the disadvantages. Hence, there is a growing interest in the design of polymer acceptors for high-performance all-polymer solar cells (all-PSCs) and all-polymer photodetectors (all-PPDs). The flexible molecular design of not only donor polymers, but also the acceptor polymers provide an extensive scope for tuning the optical, electronic, morphological, and mechanical properties of the resulting devices.<sup>[12]</sup> For instance, conjugated polymers tend to harvest more photons as they exhibit higher  $\alpha$  values in the visible and NIR spectral regions compared to PC<sub>71</sub>BM.<sup>[13]</sup> Also, the  $E_g$  of acceptor polymers can readily be tuned using the alternating donor-acceptor (D-A) approach with different combinations of monomers, which is successfully used to control the  $E_g$  of donor polymers.<sup>[14]</sup> Finally, the mechanical robustness of polymers is extremely beneficial for realizing flexible PSCs and PPDs with high stabilities.<sup>[15]</sup>

However, all-PSCs and all-PPDs often suffer from increased charge recombination, induced by suboptimal morphology with large phase separation (Details on morphology engineering are presented in Chapter 3). Thus, the overall performances of all-PSCs and all-PPDs are still lower than any of their commercially available inorganic competitors, which is one of the primary challenges hindering their commercial application.

### 1.3 Aim and Outline of the Thesis

As mentioned above, the low efficiency of all-PSCs and all-PPDs is one of the primary challenges and it is mainly limited by charge recombination due to suboptimal morphologies. Therefore, the aim of this thesis is to address approaches towards high-performance all-PSCs and all-PPDs, especially by modifying the acceptor molecular structure, and rationally choosing a suitable donor and acceptor combination. The research work addresses two aspects: acceptor polymer synthesis and device engineering. Overall, the focus is on understanding the subtle interplay between acceptor molecular structure, morphology and device performance.

Since the naphthalene diimide (NDI)-based acceptor polymers have been the most popular acceptors in all-PSCs, the first research question is then: *How to further improve the performance of all-PSCs using NDI-based acceptor polymers?* This question is related to three hypotheses:

1. By incorporating flexible units in the acceptor polymer backbone, the *crystallinity* can be tuned, which will have a direct effect on the morphology of the targeted donor:acceptor (D:A) blend. As such, the blend morphology can then be optimized, leading to improved performance of all-PSCs.
2. By utilizing properly matched donor and acceptor polymers, the *absorption* spectra can be broadened or the *open-circuit voltage* can be modified, further improving the performance of the all-PSCs in the optimal morphology condition.
3. Good miscibility with nano-scale phase separation can be achieved in *ternary systems* by choosing suitable donor and acceptor polymers, in combination with proper device engineering. As such, ternary blends incorporating two donor polymers and one acceptor polymer with complementary absorption can overcome the absorption limit and boost the PCE of all-PSCs.

On the other hand, NDI-based acceptors bear intrinsic drawbacks like low absorption coefficient and low-lying LUMO level. The second related research question is: *Is there any other promising acceptor building block except NDI, which can further boost the performance of all-PSCs?* The hypothesis is that:

4. Other electron-deficient units which have been successfully utilized in donor polymers can be promising as building blocks for acceptors, featuring *suitable LUMO levels and higher absorption coefficients* in comparison with NDI-based polymers.

The third research question is related to all-PPDs and is: *Is it possible to reduce the dark current of all-PPDs using NDI-based acceptor polymers while maintaining the high EQE achieved in all-PSCs?* The related hypothesis is:

5. Decreasing the content of acceptor polymer can be an effective way to reduce the dark current under the desired morphology condition without sacrificing the photoresponsivity.

Before delving into a discussion of the results achieved based on the above hypotheses, a detailed introduction is given to conjugated polymers (Chapter 2), and all-PSCs and all-PPDs (Chapter 3). The first three hypotheses are discussed in Chapter 4. Different approaches to achieve high-efficiency all-PSCs are highlighted, including modulation of acceptor polymer crystallinity, matching energy levels and absorption spectra of donor and acceptor materials, and the ternary approach. The detailed studies are described in Paper I, III, IV, V and VI. The fourth hypothesis is addressed in Chapters 5 and 6. Chapter 5 discusses the use of diketopyrrolopyrrole (DPP)- and isoindigo (IID)-based acceptor polymers in all-PSCs, focusing on the study reported in Paper II. Some unpublished results are also discussed in Chapter 5. In addition, the preliminary study of thiadiazoloquinoxaline (TDQ)-based acceptor polymers in all-PSCs are discussed in Chapter 6. The final hypothesis is discussed in Chapter 7. The study and discussion about all-PPDs using NDI-based polymers as acceptors are based on Paper VII. Chapter 8 summarizes the previous Chapters and brings up the major challenges all-PSCs and all-PPDs face. For the interested readers, the relevant experimental methods are described in Chapter 9.

## 2 Conjugated Polymers

---

---

### 2.1 Optical and Electrochemical Properties

The  $E_g$  of a molecule corresponds to the energy difference between the ionization potential (IP) and electron affinity (EA), referring to the minimum energy required to create an electron-hole pair that is not bound together. The optical energy bandgap ( $E_g^{\text{opt}}$ ) of a molecule is defined as the energy of the lowest electronic transition accessible via absorption of a single photon.<sup>[16]</sup> As the electron and hole remain electrostatically bound to each other in the first excited state ( $S_1$ ),  $E_g^{\text{opt}}$  is generally lower than  $E_g$ , and the difference between  $E_g$  and  $E_g^{\text{opt}}$  is defined as electron-hole pair binding energy ( $E_B$ ). The relation between  $E_g$ ,  $E_g^{\text{opt}}$ ,  $E_B$ , IP, and EA is schematically illustrated in Figure 2.1.

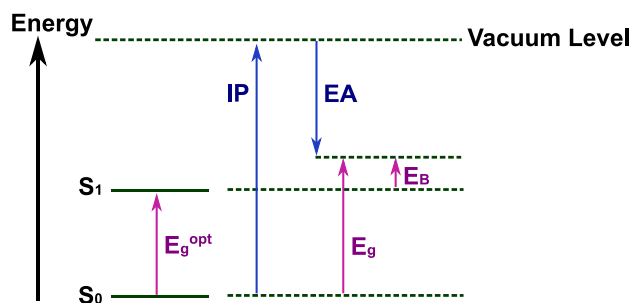


Figure 2.1 Illustration of bandgap energies.

As shown in Figure 2.2,  $E_g^{\text{opt}}$  is experimentally estimated by the onset of the absorption spectra ( $\lambda_{\text{onset}}$ ) according to the following equation:<sup>[17]</sup>

$$E_g^{\text{opt}}(\text{eV}) = \frac{h \times c}{\lambda_{\text{onset}}} \approx \frac{1240}{\lambda_{\text{onset}} (\text{nm})} \quad (2.1)$$

where  $h$  is the Plank constant ( $6.6 \times 10^{-34} \text{ J s}$ ), and  $c$  is the speed of light ( $3.0 \times 10^8 \text{ m s}^{-1}$ ).

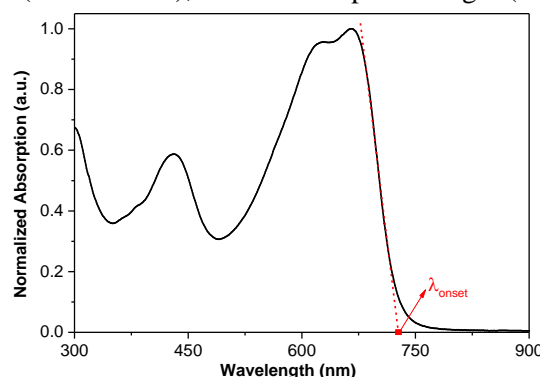


Figure 2.2 Schematic representation of an absorption spectrum and the respective  $E_g^{\text{opt}}$  estimation.

As EA and IP can be estimated from the lowest unoccupied molecular orbital (LUMO) and the highest occupied molecular orbital (HOMO) energy levels, respectively, these energy levels can be calculated from the reduction and oxidation potentials of the molecule, respectively. A molecule is oxidized if an electron is removed, and if instead an electron is accepted, the molecule is reduced. The oxidation potential ( $E_{\text{ox}}$ ) and reduction potential ( $E_{\text{red}}$ ) of polymers can be measured by electrochemical techniques, like cyclic voltammetry (CV) and square-wave voltammetry (SWV). CV measurements ideally yield reversible or *quasi-reversible* redox profiles.  $E_{\text{ox}}$  can then be determined from the average of the oxidation peak value, while oxidizing the neutral molecule to the radical cation, and the consecutive reduction peak value back to the neutral state.  $E_{\text{red}}$  is calculated in a similar manner from the reduction peak and the consecutive oxidation peak. However, owing to the frequent irreversible reduction to radical cations or oxidation to neutral states,  $E_{\text{ox}}$  and  $E_{\text{red}}$ , for conjugated polymers, are usually taken from the first oxidation peak onset and the first reduction peak onset, respectively, (Figure 2.3, bottom profile).<sup>[18]</sup> In this, SWV was utilized to determine the  $E_{\text{ox}}$  and  $E_{\text{red}}$  of conjugated polymers as it is more sensitive and results in much clearer peaks in the voltammograms (Figure 2.3, top profile).<sup>[19]</sup> Furthermore, the HOMO and LUMO levels need to be expressed in the absolute potential scale, *i.e.*, with respect to the vacuum level. In our case, potentials were referenced to the ferrocenium/ferrocene ( $\text{Fc}^+/\text{Fc}$ ) couple using Fc as an internal standard. The HOMO and LUMO levels were estimated from the peak potentials by setting the oxidative peak potential of  $\text{Fc}/\text{Fc}^+$  *vs.* the normal hydrogen electrode (NHE) to 0.63 V, and the NHE *vs.* the vacuum level to 4.5 V.<sup>[20]</sup> The energy levels, therefore, were calculated according to the formula  $\text{HOMO} = -(E_{\text{ox}} + 5.13)$  eV and  $\text{LUMO} = -(E_{\text{red}} + 5.13)$  eV.

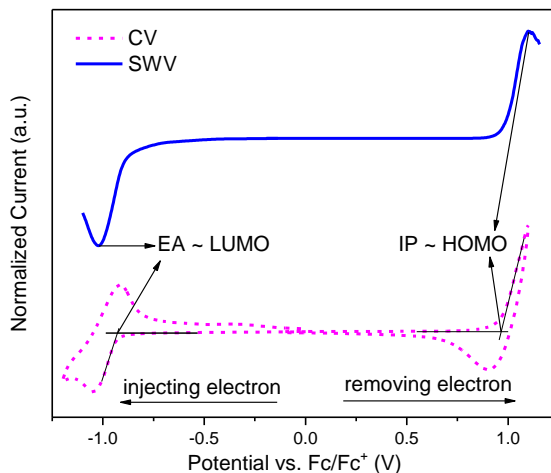


Figure 2.3 Energy levels determined from CV and SWV measurements.

## 2.2 Molecular Design towards Energy Bandgap Control

There are two possible resonance structures for the ground state of the backbone of a polyaromatic conjugated material, with nondegenerate energy: the aromatic form with confined  $\pi$ -electrons and the quinoid form with delocalized  $\pi$ -electrons along the polymer chain. (Figure 2.4). The quinoid form is energetically less stable compared to the aromatic form and has a smaller  $E_g$  owing to the destruction of the aromaticity and consequent loss in the stabilization energy.<sup>[21]</sup> Overall, the  $E_g$  decreases linearly as a function of the increasing quinoid state population. As demonstrated in Figure 2.4, a reduction of

aromaticity in the conjugated polymer main chain offers a greater tendency to form the quinoid state through  $\pi$ -electrons delocalization.

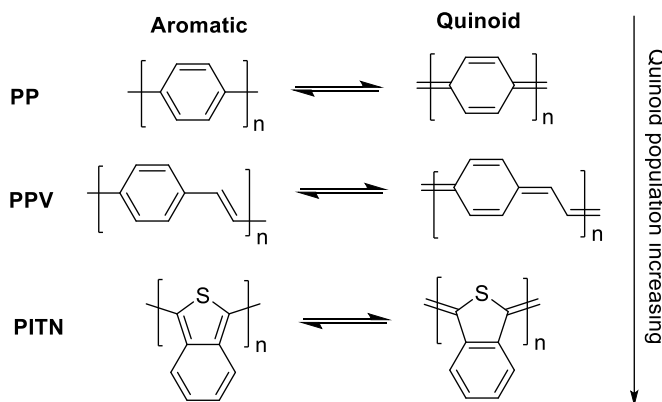


Figure 2.4 Aromatic and quinoid resonance forms for the ground state within nondegenerate energy.

Examples of effective methods towards controlling the  $E_g$  are described below:<sup>[22]</sup>

#### *Fused Heterocycles:*

The most effective way to increase the quinoid character of polythiophene is represented by polyisothianaphthene (PITN) (Figure 2.4).<sup>[23]</sup> Because of the larger aromatic resonance energy of benzene compared to thiophene (T), the main chain of PITN tends to favor the quinoid state to maintain the benzene aromaticity, which makes PITN the first well-known conjugated polymer with a narrow  $E_g$  as low as 1 eV.<sup>[24]</sup>

#### *Electron-donating or Electron-withdrawing Substituents:*

The direct incorporation of electron-donating or electron-withdrawing groups in the polymer main chain represents the most straight forward method to tune the  $E_g$  through either inductive or mesomeric effects. In 1994, Bredas and Heeger reported that the electron-donating groups can up-shift the energy levels with the HOMO level rising more than the LUMO level, while the electron-withdrawing groups can down-shift the energy levels with the LUMO level declining more than the HOMO level.<sup>[25]</sup>

#### *D-A Alternating Approach:*

The most popular strategy to tune the  $E_g$  of conjugated polymers is to regularly alternate the donor and acceptor units along the polymer backbone.<sup>[26]</sup> The push-pull driving force between the donor (D) and acceptor (A) components facilitates the delocalization of electrons and the formation of quinoid mesomeric structures ( $D-A \leftrightarrow D^+-A^-$ ) over the polymer main chain. Additionally, as illustrated in Figure 2.5, new HOMO and LUMO levels of D-A copolymers are formed due to the hybridization of the molecular orbitals between donor and acceptor units.<sup>[27]</sup> The redistribution of electrons results in a higher-lying HOMO level and a lower-lying LUMO level, which leads to narrowed  $E_g$  and broadened optical spectra. It is also worth noting that the magnitude of  $E_g$  reduction is strongly dependent on the strength of donor and acceptor units embedded in the polymer backbone and a judicious choice of the combination of donor and acceptor units is required to tune the  $E_g$  to the desired magnitude.<sup>[28]</sup>

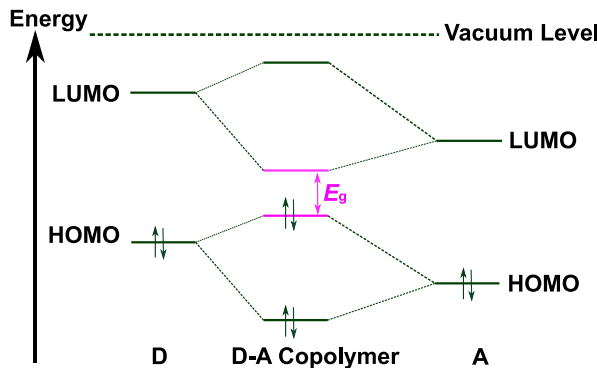


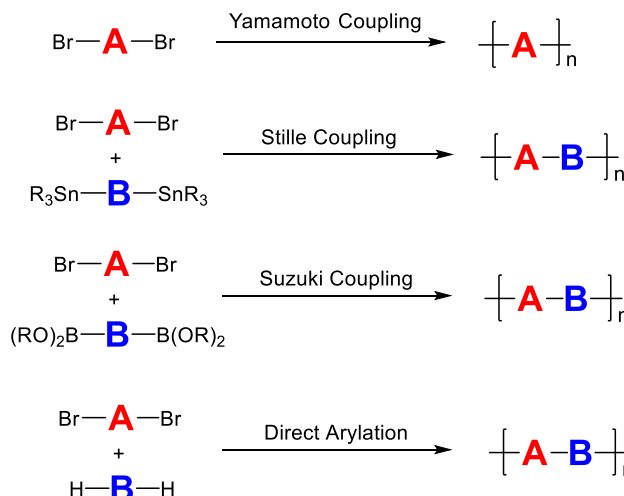
Figure 2.5 Illustration of energy level hybridization in D-A copolymers. D refers to donor unit and A refers to acceptor unit.

#### *Two-dimensional (2D) Effect:*

$E_g$  can also be tuned through enhancing the intermolecular charge transfer, which occurs as a result of the overlapping of  $\pi$  electrons between the adjacent polymer backbones, known as  $\pi$ - $\pi$  interaction.<sup>[29]</sup> 2D conjugated polymers are designed to increase  $\pi$ - $\pi$  interactions. In 2006, Hou *et al.* reported that 2D polythiophenes with conjugated side chains could lead to enhanced  $\pi$ - $\pi$  interaction, resulting in a broadened absorption spectrum.<sup>[30]</sup> Moreover, efficient intermolecular charge transfer can also result in higher charge carrier mobility, which is of critical importance for PSCs and PPDs.

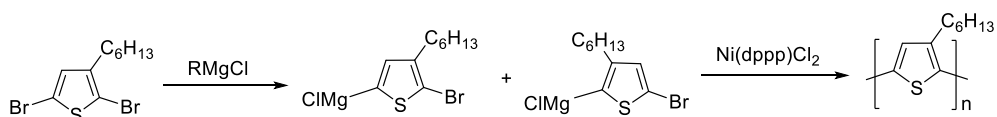
## 2.3 Synthesis of Conjugated Polymers

$\pi$ -Conjugated polymers are synthesized mainly by metal catalyzed step-growth polycondensation and chain growth polymerization reactions.<sup>[22a,31]</sup> The most popular synthetic routes to prepare conjugated polymers are illustrated in Scheme 2.1. The nickel-mediated Yamamoto dehalogenation coupling reactions are widely used for self-polymerization of single monomers.<sup>[32]</sup> Stille and Suzuki cross-coupling polycondensation reactions are the most widely used methods in laboratory scale synthesis of alternating copolymers.<sup>[31c]</sup> The mechanisms are presented in detail in the following section, since either Stille or Suzuki reactions have been employed to synthesize the conjugated acceptor polymers studied in this thesis. An alternative to the Stille and Suzuki coupling reactions is a polycondensation reaction via dehydrohalogenative cross-coupling, known as direct arylation. It has become as a promising method for the synthesis of highly pure conjugated polymers.<sup>[33]</sup> In this reaction, organometallic monomers are not required and the nonfunctionalized (hetero)arenes are coupled directly through C-H bond cleavage.



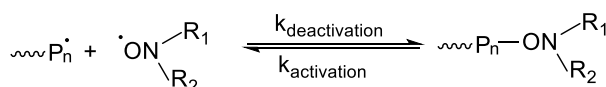
Scheme 2.1 Popular polymerization reactions

Except for the popular routes mentioned above, the nickel-catalyzed Kumada catalyst transfer polycondensation (KCTP), also known as Grignard metathesis (GRIM) polymerization has been one of the most convenient way in the preparation of head-to-tail (HT) coupled polythiophenes.<sup>[36]</sup> The synthetic route is shown in Scheme 2.2. Two metalated regioisomers are obtained via a magnesium exchange reaction, and the subsequent polymerization occurs instead of alkylation of the thiophene ring in the presence of Ni-initiator.



Scheme 2.2 Synthesis of poly(3-hexylthiophene) via KCTP

Recently, nitroxide-mediated radical polymerization (NMRP) has also gained attraction as a metal catalyst-free oxidative coupling reaction.<sup>[37]</sup> In this polymerization, the reactions are controlled by an equilibrium between the propagating radicals by nitroxides and dormant species by the formation of alkoxyamines (Scheme 2.3).



Scheme 2.3 General mechanism of NMRP

### 2.3.1 Stille and Suzuki Reactions

The Stille and Suzuki cross-coupling reactions are quite similar and both use a palladium catalyst. The catalytic cycle of the Stille and Suzuki reactions is shown in Figure 2.6. The cycle starts with an oxidative addition of the aryl-halide to the Pd catalyst. A transmetallation reaction introduces the other coupling partner to the palladium center. The coupling is completed through a reductive elimination, reforming the Pd(0) catalyst. The main difference is in the type of metallized coupling species used. A

stannyl-compound is employed as one coupling partner in Stille coupling reaction, while the Suzuki reaction uses a boronic acid derivative (Scheme 2.1). The other coupling partner is generally an alkenyl or aryl halide.<sup>[34]</sup> Additionally, the Suzuki reaction takes place in the presence of a base.<sup>[35]</sup> It was reported that the base has three roles in the reaction mechanism for Suzuki coupling reaction: formation of the palladium complex, formation of the trialkyl borate and acceleration of the reductive elimination step.<sup>[35]</sup> It is noteworthy that Stille coupling is more suitable for thienyl stannanes as monomers, while aryl stannanes generally give poor reactivity. The Suzuki coupling is more widely utilized to prepare alternating polymers starting from monomers containing boronic groups on the benzene ring.

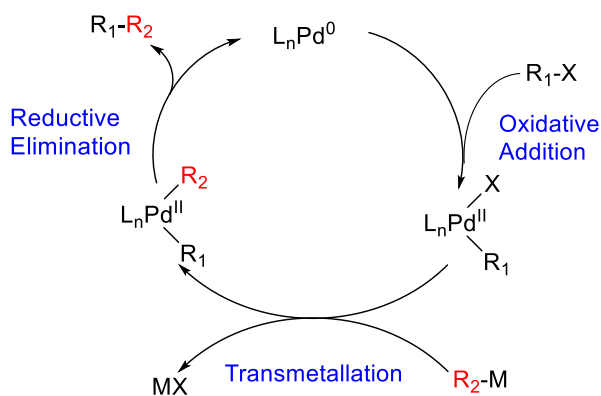


Figure 2.6 Catalytic cycle of the palladium catalyzed Stille and Suzuki reactions

### 3 All-Polymer Solar Cells and Photodetectors

---

#### 3.1 Working Principle and Device Structures

The process of converting light into photocurrent ( $I_{ph}$ ) within PSCs and PPDs without bias voltage is shown in Figure 3.1. There are four main steps in this process: (a) optical absorption and exciton formation. Upon absorption of a photon by the active layer, an electron is photoexcited, leading to the formation of a tightly bound electron-hole pair (exciton). (b) The exciton can diffuse towards the D:A interface, then (c) the exciton dissociates first into a weakly bound charge-transfer (CT) state at the interface, and into free charge carriers. The exciton separation (charge generation) is driven by the difference between the respective donor and acceptor LUMO levels, which normally is required to be around 0.3 eV.<sup>[36]</sup> However, recent results have highlighted systems that achieve high-performance with negligible driving force.<sup>[37]</sup> (d) The free charge carriers then drift towards the electrodes and are extracted at the respective electrodes generating electrical current.<sup>[38]</sup>

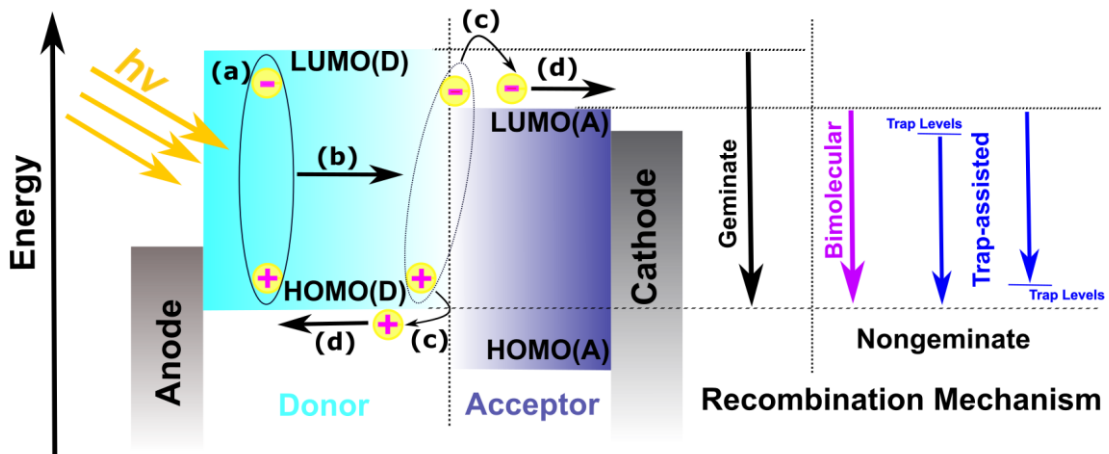


Figure 3.1 Left: simplified illustration of the working principle of PSCs and PPDs without bias voltage. Right: simplified illustration of the geminate and nongeminate recombination mechanisms. The two most encountered nongeminate recombination mechanisms: bimolecular and trap-assisted recombination.

Compared to PSCs, the target of PPDs is to deliver a  $I_{ph}$  signal, rather than an electric power to a load. Thus, PPDs can operate under reverse external voltage in order to enhance charge carrier photogeneration, collection and shorten device response time.<sup>[39]</sup>

Figure 3.2 shows the working principle of PPDs at forward injection mode in the dark and charge collection mode under illumination. Ohmic contacts need to be formed between the photoactive layer and the electrodes to constitute Schottky diodes. Under reverse bias (Figure 3.2 b), electron injection takes place from the anode to the LUMO of the acceptor polymer, resulting in large Schottky barriers ( $\phi_B$ ) at the two electrode sides, which leads to asymmetry in the current density–voltage ( $J$ – $V$ ) characteristics with low dark current ( $I_d$ ).

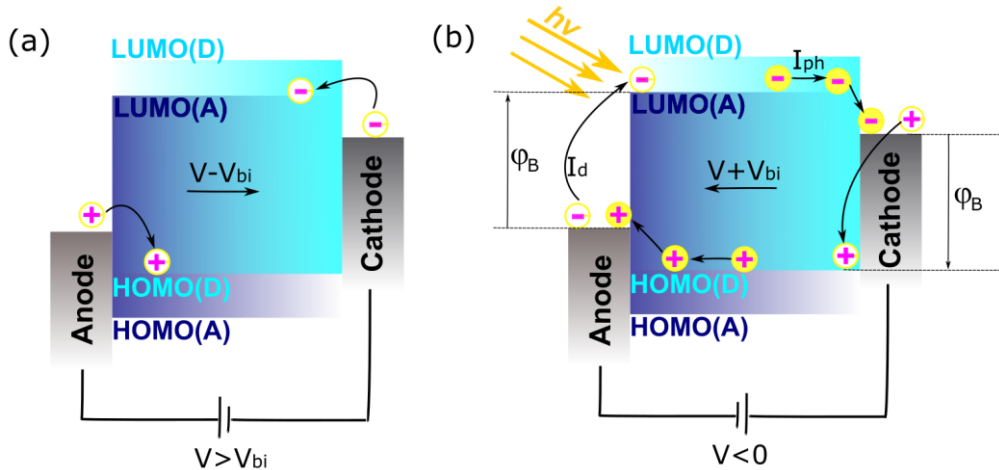


Figure 3.2 Illustration of the working principle in PPDs: (a) at forward injection mode (in the dark) and (b) charge collection mode (under illumination).  $V$  is applied voltage,  $V_{bi}$  is the built-in voltage,  $I_{ph}$  is the photo-generated current, and  $I_d$  is the dark current.

In 1986, Tang introduced the bilayer junction concept into organic solar cells (OSCs), bringing an electron donor material (phthalocyanine dye) and an electron acceptor material (perylene tetracarboxylic derivative) together as active layer and achieved ~1% PCE. This pioneering experiment marks the starting point of modern OSCs.<sup>[40]</sup> In 1993, the first bilayer PSC was reported by N. S. Sariciftci *et al.* using poly[2-methoxy-5-(2-ethylhexyloxy)-1,4-phenylenevinylene] (MEH-PPV) and C<sub>60</sub> as active layer.<sup>[41]</sup> As the exciton diffusion length ( $L_D$ ) in polymer semiconductors is typically 1-10 nm,<sup>[42]</sup> only material within a few nanometers of the bilayer interface can generate photo-induced charges efficiently. As seen in Figure 3.3 a, the D:A interface is too far away from the molecule where the photo-excitation occurs. To circumvent this problem, the BHJ concept was developed by simply blending the electron donor and acceptor materials (Figure 3.3 b), with the possibility of forming a bicontinuous interpenetrating network of the individual donor and acceptor materials for effective charge generation and charge transport.<sup>[43]</sup> Thus, controlling the morphology of the active layer has become crucially important, which will be discussed in Section 3.7 in detail. It is also important to note that Figure 3.3 b is a simplified illustration, and generally there are no pure phases except within the crystals. Today, BHJ is the dominant active layer geometry in PSCs and PPDs, and devices studied in this thesis are also based on the BHJ concept.

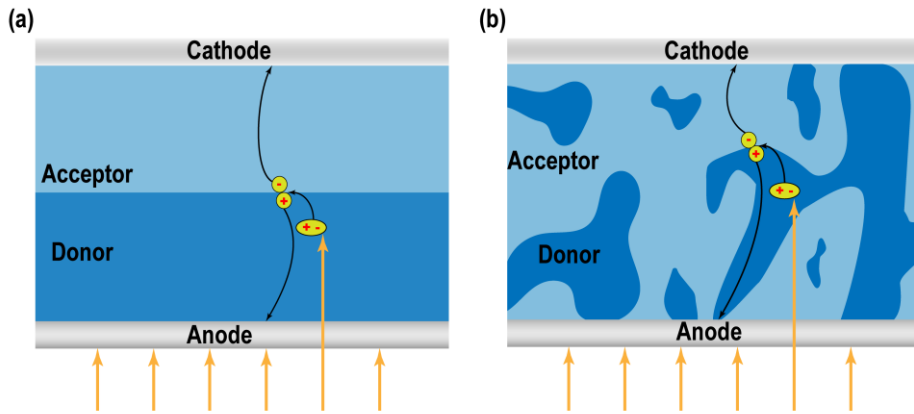


Figure 3.3 Simplified schematic of (a) bilayer junction and (b) BHJ active layer morphology. (Neither phase is necessarily pure, it may contain a certain amount of the second (donor or acceptor) material)

All-PSC and all-PPD devices fabricated in the laboratory typically comprise a glass substrate with a layer of semitransparent conducting indium tin oxide (ITO) as the bottom electrode, a carrier selecting layer, an active layer, a second carrier selecting layer and an evaporated metal as the top electrode. Depending on the polarity of the bottom electrode, the device structures can be divided into two different categories: conventional and inverted. The two different device structures adopted in this thesis are shown in Figure 3.4.

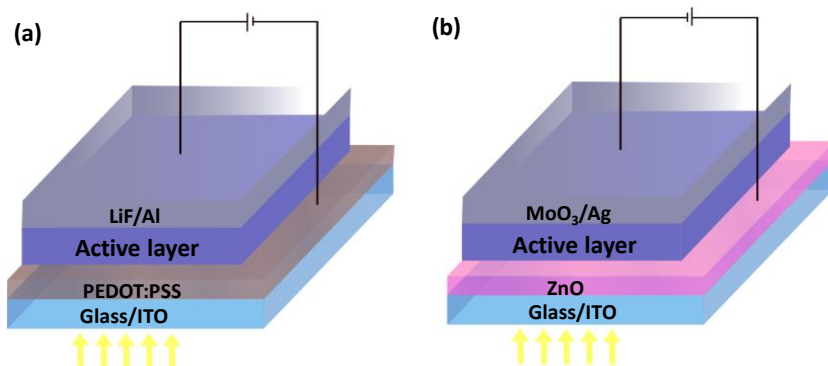


Figure 3.4 Schematic of (a) conventional and (b) inverted device structures adopted in this thesis.

## 3.2 Figures of Merit

### 3.2.1 Figures of merit for PSCs

To evaluate PSCs in the laboratory, the device is normally illuminated on the bottom electrode under a solar simulator lamp with a standard AM 1.5G solar irradiance spectrum (Figure 3.5). AM 1.5G refers to the spectral irradiance on the earth surface at 48.2° relative to the Earth's normal for direct sunlight together with the scattered contribution from atmosphere integrated over a hemisphere, which is defined by the American Society for Testing and Materials (ASTM International Standard). Under this condition, one sun is defined to be equal to 100 mW/cm<sup>2</sup>. The Shockley-Queisser efficiency limit under AM 1.5G radiation spectrum is shown in Figure 3.5.<sup>[44]</sup> The Shockley-Queisser limit describes the maximum theoretical efficiency of an ideal *p-n* junction SC, which was originally presented by

Shockley and Queisser in 1961 using the black body spectrum.<sup>[45]</sup> For PSCs, the electronic structure of photovoltaic polymers defines the lower limit of photon energy that can be absorbed.

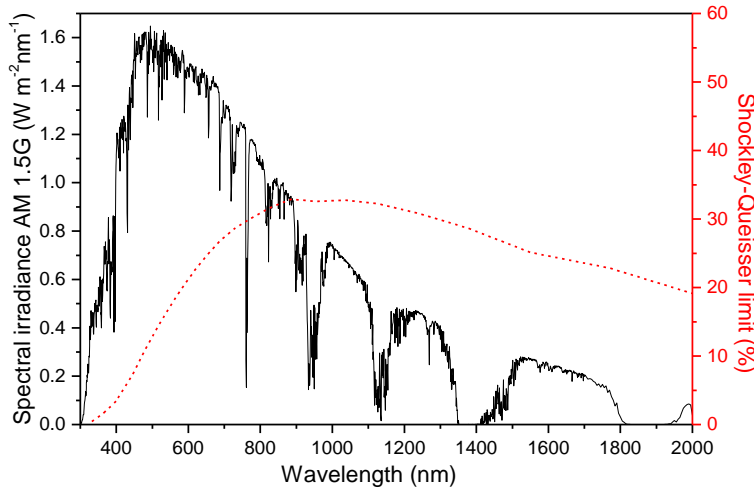


Figure 3.5 Schematic representation of AM 1.5G spectral irradiance and the Shockley-Queisser limit for AM 1.5G.

Upon illumination, the  $I_{ph}$  is recorded and normalized with respect to the device area to give a  $J$ . Furthermore, the applied voltage is varied to yield a J–V dependence, and upon plotting the J–V curve (Figure 3.6 a), different performance characteristics can be extracted:

*Short circuit current density ( $J_{sc}$ )* is the maximum current density attainable when the voltage across the device is zero whilst the solar cell is illuminated. There are different factors that affect the  $J_{sc}$  such as the level of illumination, efficiency of charge generation, efficiency of charge collection and photon absorption.<sup>[46]</sup>

*Open-circuit voltage ( $V_{oc}$ )* is the voltage obtained when the current across the device is zero. The  $V_{oc}$  depends on many factors, such as the energy difference between the HOMO of the donor and the LUMO of the acceptor and the binding energy of the CT state:

$$V_{oc} = \frac{E_{LUMO}^A - E_{HOMO}^D - E_B}{q} - C \quad (3.1)$$

where  $E_{LUMO}^A$  is the LUMO energy level of the acceptor,  $E_{HOMO}^D$  is the HOMO energy level of the donor,  $E_B$  is the exciton binding energy,  $q$  is the elementary charge of the electron ( $1.6 \times 10^{-19}$  C), and  $C$  is a constant related to illumination and temperature.<sup>[47]</sup>

*Fill factor (FF)* is the measure of squareness of the J–V curve (Figure 3.6 a) and is governed by the competition between charge recombination and extraction.<sup>[48]</sup> It is defined as the ratio between the obtained maximum power output ( $P_{max}$ ) and the theoretical power output:

$$FF = \frac{P_{max}}{J_{sc} V_{oc}} = \frac{J_{max} V_{max}}{J_{sc} V_{oc}} \quad (3.2)$$

where  $J_{max}$  and  $V_{max}$  are the  $J$  and  $V$  at the maximum power point.

PCE is defined as the ratio of  $P_{max}$  and input power of the incident light ( $P_{in}$ ), which is the most common figure of merit used to compare SCs and is given by

$$PCE = \frac{P_{max}}{P_{in}} = \frac{FFJ_{sc}V_{oc}}{P_{in}} \quad (3.3)$$

As shown in Equation 3.3, three characteristics  $V_{oc}$ ,  $J_{sc}$ , and FF should be modulated to increase the PCE. The corresponding approaches are elucidated in Chapter 4. Besides the figures of merit introduced above, which can be attained from the  $J$ - $V$  curve, there are two more photovoltaic performance characteristics frequently used:

*External quantum efficiency (EQE)* (also known as the incidence photon-to-electron conversion efficiency (IPCE)) is a spectral quantity and is defined as the number of charges collected at the electrodes ( $N_{el}^{out}$ ) divided by the number of incident photons ( $N_{ph}^{in}$ ) at a particular wavelength  $\lambda$ :

$$EQE(\lambda) = \frac{N_{el}^{out}(\lambda)}{N_{ph}^{in}(\lambda)} \quad (3.4)$$

EQE is impacted by photon absorption and exciton generation ( $\eta_A$ ), exciton diffusion ( $\eta_D$ ), exciton dissociation by charge transfer ( $\eta_{CT}$ ), and charge carrier collection ( $\eta_{CC}$ ). Moreover, it can be related to the  $J_{sc}$  under the AM 1.5G illumination via

$$J_{sc}^{EQE} = \int \varphi_p(\lambda) EQE(\lambda) d(\lambda) \quad (3.5)$$

where  $\varphi_p(\lambda)$  is the photon flux of AM1.5 solar radiation.

*Internal quantum efficiency (IQE)* is also a spectral quantity and is defined as the ratio between ( $N_{el}^{out}$ ) and the number of absorbed photons in the active layer ( $N_{ph}^{abs}$ ):

$$IQE(\lambda) = \frac{N_{el}^{out}(\lambda)}{N_{ph}^{abs}(\lambda)} \quad (3.6)$$

The detailed simulation of the absorptance of the photons in the active layer can be found in Chapter 9. If all photons absorbed by the active layer can be converted to photocurrent (IQE is 100%), the theoretical maximum photocurrent density ( $J_{tmax}$ ) of the all-PSCs can be calculated via integrating the simulated absorptance of the photons in the active layer with the AM 1.5G spectrum.

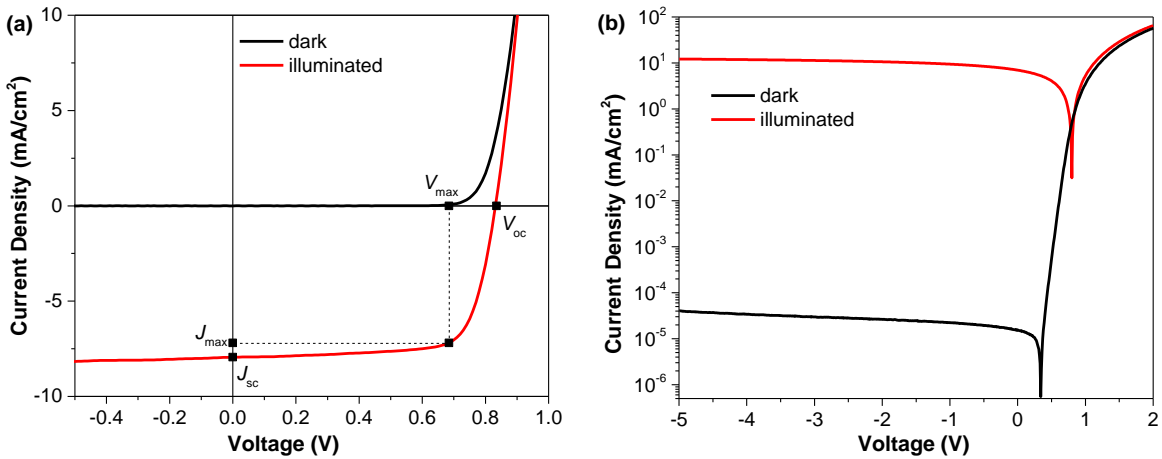


Figure 3.6 Schematic of (a) linear and (b) semi-logarithmic  $J$ - $V$  curves under illumination and in the dark.

### 3.2.2 Figures of merit for PPDs

Although PSCs and PPDs are structurally similar, their figures of merit are quite different. Figure 3.6 a shows  $J$ - $V$  characteristic plotted in the linear scale which reveals the interesting features of PSCs, while Figure 3.6 b illustrates the  $J$ - $V$  curve plotted in the logarithmic scale which is relevant for PPDs. The latter highlights the accurate value of *dark current density* ( $J_d$ ) and the nature of a Schottky diode.

The prerequisites for high-performance PPDs are the attainment of low  $J_d$  and high EQE at a high negative bias voltage.<sup>[49]</sup> The dark current should be minimized in order to improve fundamental aspects like the effectiveness of signal detection and power consumption. Other figures of merit are listed as follows:

*Responsivity* ( $R$ ), which is essentially the ratio between the output current and the input light power, is expressed as

$$R(\lambda) = \frac{J_{ph}(\lambda)}{I(\lambda)} = \frac{EQE(\lambda)q}{hv} \quad (3.7)$$

where  $J_{ph}(\lambda)$  is the photocurrent density,  $I(\lambda)$  is the incident light intensity, and  $v$  is the frequency of light.

*Noise equivalent power* (NEP) is the lowest light power needed to distinguish  $J_{ph}$  from the noise current, *i.e.*, the input optical power at signal/noise ratio (S/N) equals 1. The NEP of a PPD can be given by the expression:

$$NEP = \frac{i_n}{R} \quad (3.8)$$

where  $i_n$  is the root mean square noise current.

There are three main contributions to the total noise, including shot noise from fluctuation of charge carries, thermal noise (Johnson noise) and flicker noise. The shot noise and thermal noise are white noise, *i.e.*, frequency-independent, while the flicker noise is inversely proportional to the frequency.<sup>[50]</sup> In the case of PPDs in which reverse bias is applied, the shot noise from the dark current is commonly

postulated to be the dominant contribution.<sup>[9c,51]</sup> The  $i_n$  generated from dark current can then be described as

$$i_n = \sqrt{2qJ_d\Delta f} \quad (3.9)$$

where  $\Delta f$  is the signal bandwidth.

The reciprocal of the NEP is referred to as the *detectivity* ( $D$ ) of the device. *The specific detectivity* ( $D^*$ ) is introduced to be able to compare the performance of different PPDs with different active areas and working bandwidth, which is a normalization of  $D$  with respect of  $\Delta f$  and  $A$ . It is expressed as

$$D^* = \frac{\sqrt{A\Delta f}}{NEP} = \frac{R}{\sqrt{2qI_d}} \quad (3.10)$$

The unit of  $D^*$  is  $\text{cm Hz}^{1/2} \text{W}^{-1}$  or Jones,  $A$  is the effective area under illumination,  $J_d$  is the dark current density in  $\text{A cm}^{-2}$ , and the unit of  $R$  is  $\text{A W}^{-1}$ . Clearly,  $D^*$  is proportional to  $R$  and inversely proportional to the square root of  $J_d$ . Therefore, reducing dark current while simultaneously maintaining high EQE is essential for achieving a high signal to noise ratio in PPDs.

### 3.3 Development of All-PSCs

The pioneering work on all-PSCs reported in 1995 employed poly[2-methoxy-5-(2'-ethyl)-hexyloxy-*p*-phenylenevinylene] (MEH-PPV) and cyano-substituted phenylenevinylene (CN-PPV) as active layer, and resulted in 0.9% PCE.<sup>[43a]</sup> In the earliest development stage, CN-PPV, fluorene and benzothiadiazole (BT)-based conjugated polymers were the most widely used acceptor polymers.<sup>[52]</sup> High value of  $V_{oc}$  were often observed due to their relatively shallow LUMO energy levels. However, the  $J_{sc}$  and FF were low, because of the relatively low electron mobility ( $\mu_e$ ) and limited absorption of visible wavelengths. Consequently, the PCEs of all-PSCs remained at around 2% for a long period of time.<sup>[53]</sup> Later on, NDI and perylene diimide (PDI) were adopted as building blocks in acceptor polymers, because of their suitable energy levels and high electron mobilities.<sup>[15,54]</sup> In 2014, naphtho[2,3-b:6,7-b']dithiophene-4,5,9,10-diimide (NDTI) was utilized in all-PSCs as a promising acceptor building block as it exhibited bathochromic absorption and high charge carrier mobilities.<sup>[55]</sup> Other promising backbone candidates for acceptor polymers like B←N-bridged bipyridine (BNBP) unit,<sup>[56]</sup> DPP unit,<sup>[57]</sup> 3,4-difluorothiophene ([2F]T) unit,<sup>[58]</sup> indacenodithiophene (IDT),<sup>[59]</sup> and bithiophene imide (BTI) unit<sup>[60]</sup> have also been developed. The photovoltaic parameters of reported high-performance all-PSCs based on representative acceptor polymers are listed in Table 3.1 and the corresponding donor and acceptor chemical structures are listed in Figure 3.7.

Table 3.1 Photovoltaic parameters of reported representative all-PSCs

D:A (w:w)	$V_{oc}$ (V)	$J_{sc}$ (mA/cm <sup>2</sup> )	FF	PCE (%)	Device Type	d <sup>a</sup> (nm)	Ref.
POPT:CNPPV (NA)	1.06	5.44	0.35	2	Normal	NA	[52a]
P3HT:PF12TBT (1:1)	1.26	3.88	0.55	2.7	Normal	60	[52b]
PTB7-Th:PDI-V (1:1)	0.75	16.10	0.64	7.6	Inverted	120	[54b]
BDDT:PNNTI-DTT (1.5:1)	0.69	13.68	0.59	5.6	Normal	NA	[55b]
PTB7-Th:P-BNBP-fBT (1:1)	1.07	12.69	0.47	6.3	Normal	110	[56a]
P3HT:PDPP2TzT (2:1)	0.64	7.8	0.61	3	Inverted	115	[57a]
PTBFTAZ:PIID[2F]T2BO/2HD (1:1)	0.97	13.2	0.55	7.3	Inverted	85	[58b]
PBDB-T:PZ1 (1.5:1)	0.83	16.05	0.69	9.2	Normal	105	[59]
PTB7-Th:f-BTI2-FT (1:2)	1.04	11.55	0.57	6.9	Normal	NA	[60]
PTzBI-Si:N2200 (2:1)	0.87	15.76	0.74	10.1	Normal	140	[61]

<sup>a</sup> active layer film thickness

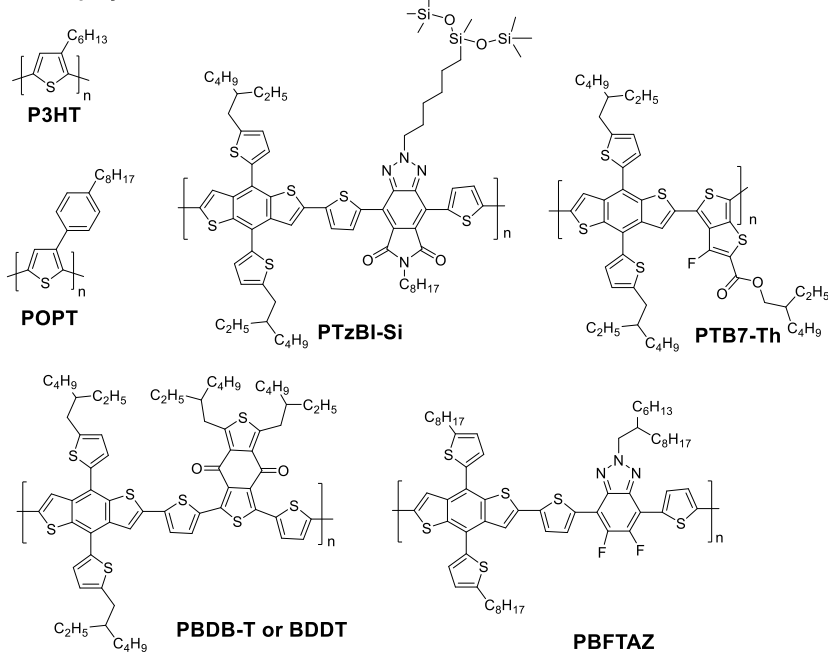
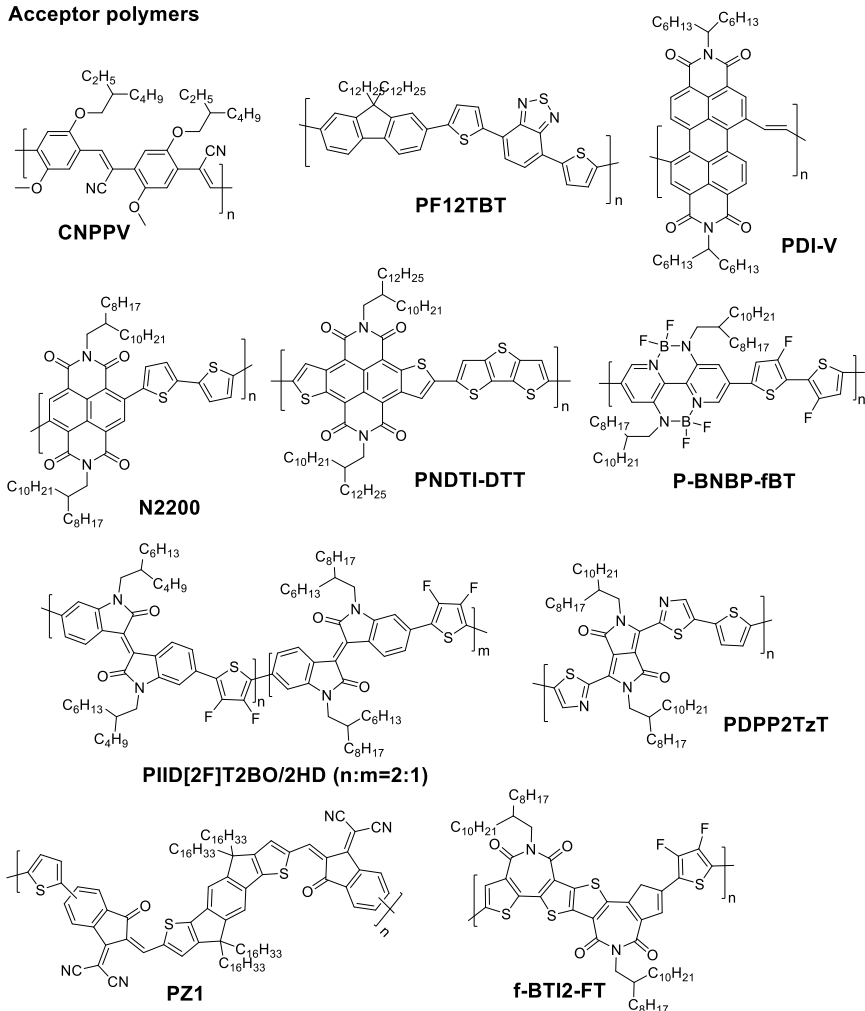
**Donor polymers****Acceptor polymers**

Figure 3.7 Chemical structures of representative donor and acceptor polymers for all-PSCs in reported literatures

### 3.4 Development of All-PPDs

Compared to the extensive effort made on the development of high-performance all-PSCs, the research on all-PPDs has been limited until recently. The first all-PPD was reported in 2009, employing poly(3-hexylthiophene-2,5-diyl) (P3HT) as electron donor and poly([9,9-dioctylfluorene]-2,7-diyl-*alt*-[4,7-bis(3-hexylthien-5-yl)-2,1,3-benzothiadiazole]-2,2,-diyl]) (F8TBT) as acceptor.<sup>[62]</sup> The inferior performance of this system in comparison with fullerene-based PPDs was mainly ascribed to the poor active layer morphology and unfavorable energy levels. Later, NDI- and PDI-based acceptor polymers were adopted in all-PPDs and  $D^*$  of greater than  $10^{12}$  Jones was achieved, which is close to that of fullerene-based PPDs.<sup>[50a,63]</sup> For comparison, the characteristics of reported all-PPDs are listed in Table 3.2 and the structures of the acceptor polymers are given in Figure 3.8.

Table 3.2 Characteristic parameters of reported all-PPDs

D:A (w:w)	R (A/W)	EQE <sup>a</sup> (%)	$J_d$ (mA/cm <sup>2</sup> )	$D^*$ <sup>b</sup> (Jones)	d (nm)	Ref.
P3HT:F8TBT (1:1)	0.1 (@-0.5V, 500nm)	20	$4.0 \times 10^{-6}$ (@-0.5V)	NA	80	[62]
P3HT:P2 (1:1)	NA (@-5V, 600nm)	1.6	$1.8 \times 10^{-5}$ (@-0.1V)	NA	120	[64]
PDPP:N2200 (1:1)	0.1 (@-2V, 850nm)	NA	$1.5 \times 10^{-6}$ (@-0.1V)	$3.4 \times 10^{12}$	180	[63a]
PDPP:PNDI-T50 (1:1)	0.09 (@-0.1V, 900nm)	12.4	$1.2 \times 10^{-6}$ (@-0.1V)	$4.7 \times 10^{12}$	NA	[63b]
PTB7-Th:PIID-NDI (1:1)	0.12 (@-1V, 730nm)	22	$7.5 \times 10^{-5}$ (@-0.2V)	$0.6 \times 10^{12}$	100	[65]
PDTP-DPP:PNDI-DPP10 (1:1)	0.05 (@-0.1V, 900nm)	NA	$1.3 \times 10^{-6}$ (@-0.1V)	$2.4 \times 10^{12}$	NA	[66]
PTB7-Th:PNDI-5DD (1:1)	NA (@-0.1V, 700nm)	30.6	$1.2 \times 10^{-7}$ (@-0.1V)	$3.0 \times 10^{13}$ (@-0.1V)	101	[67]

<sup>a</sup> Measured at the same reverse voltage and wavelength as the R

<sup>b</sup> Measured at the same reverse voltage as the  $J_d$

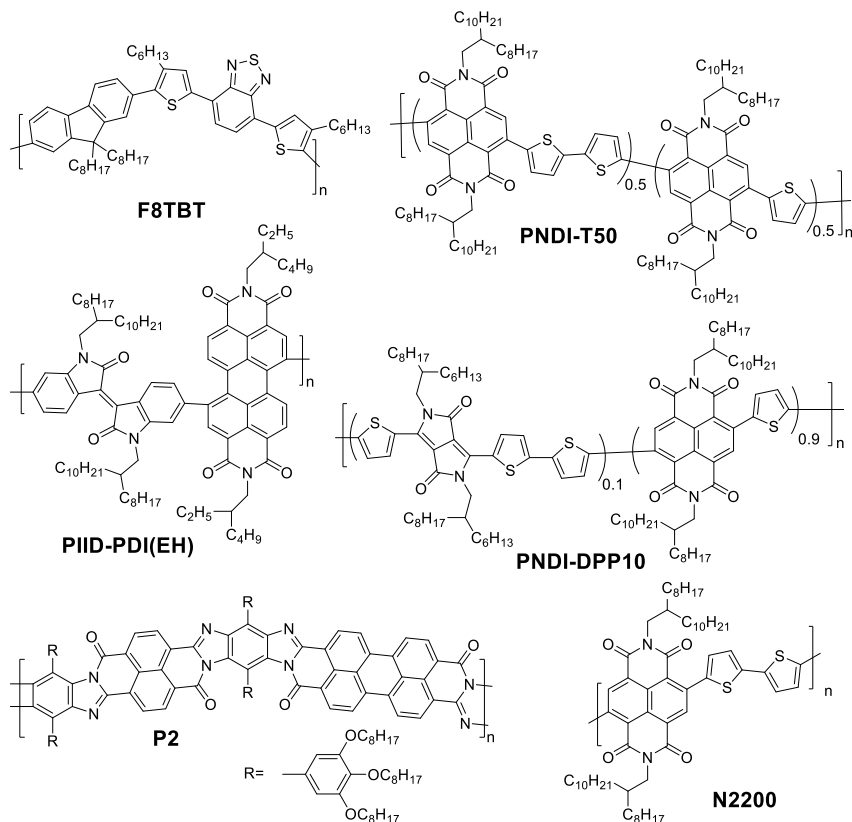


Figure 3.8 Chemical structures of acceptor polymers for all-PPDs in reported literatures

### 3.5 Charge Recombination

Charge carrier recombination is one of the key energy loss mechanisms in PSCs and PPDs. Due to the relatively low dielectric constant,  $\epsilon_r$ , of polymeric materials, the excited electron-hole pairs often recombine back to the ground state in a process known as *geminate recombination* before they fully dissociate into free charge carriers. It is driven by the Coulomb attraction between the geminate electron-hole pair. After charge generation, free electrons and holes can encounter each other and subsequently recombine back to the ground state in a process known as *nongeminate recombination* (Figure 3.1).<sup>[68]</sup>

#### 3.5.1 Geminate Recombination

The geminate recombination loss scales linearly with incident light intensity,  $I$ , and can be field-dependent.<sup>[69]</sup> It has been reported that the strength of the field dependence of geminate recombination also varies between different active layers and processing conditions in fullerene-based PSCs.<sup>[70]</sup> Whereas the high-performance fullerene-based PSCs with FF exceeding 0.65 usually exhibit little field dependent geminate recombination loss.<sup>[71]</sup>

The geminate and total recombination losses can be estimated from the  $J_{sc}$ , saturated photocurrent density ( $J_{sat}$ ) and the theoretical maximum photocurrent density,  $J_{tmax}$ , of all-PSCs. The total recombination efficiency ( $\eta_T$ ) is then calculated by the equation:

$$\eta_T = 1 - \frac{J_{sc}}{J_{tmax}} \quad (3.11)$$

The geminate recombination efficiency ( $\eta_{GR}$ ) can be calculated by

$$\eta_{GR} = 1 - \frac{J_{sat}}{J_{tmax}} \quad (3.12)$$

### 3.5.2 Non-geminate Recombination

Non-geminate recombination includes the recombination of a free electron and a free hole known as *bimolecular recombination* and the recombination of a free electron (hole) and a trapped hole (electron) known as *trap-assisted recombination* (Figure 3.1).

*Bimolecular Recombination* losses are the most commonly observed nongeminate recombination losses in fullerene-based PSCs and PPDs and are widely accepted to be the main recombination channel in BHJ PSCs.<sup>[72]</sup> The recombination rate ( $R_{BR}$ ) per volume is proportional to the product of the electron and hole charge densities ( $n$  and  $p$ , respectively):<sup>[48]</sup>

$$R_{BR} = \gamma_{pre} k_{BR} np \quad (3.13)$$

where  $\gamma_{pre}$  is a dimensionless reduction prefactor,  $k_{BR}$  is the classic Langevin recombination coefficient, defined as  $k_{BR}=q(\mu_e + \mu_h)/\epsilon_0\epsilon_r$ ,  $\epsilon_0$  is absolute dielectric constant of vacuum and  $\epsilon_r$  is relative dielectric constant of the blend.  $\mu_e$  and  $\mu_h$  are the electron and hole mobility, respectively. Since the reduction of classical Langevin recombination has been observed experimentally in some all-polymer blends, the Langevin expression is considered to be an upper limit for the bimolecular recombination losses.<sup>[73]</sup> As both  $n$  and  $p$  depend on  $I$ , the recombination losses are nonlinear with respect to  $I$ .

The bimolecular recombination efficiency ( $\eta_{BR}$ ) is often estimated by measuring the  $J_{sc}$  dependence of  $I$  on a logarithmic scale. The slope ( $\beta$ ) of the linear fitting for the logarithmic dependence of  $J_{sc}$  on  $I$  gives an indication of the bimolecular recombination losses. Bimolecular recombination is thought to be negligible at the short-circuit condition, if  $\beta$  is close to 1. However, Janssen *et al.* have demonstrated that the  $I$  dependence method is not accurate enough, since the bimolecular recombination losses can vary up to tens of percent under illumination while the  $J_{sc}$  versus  $I$  seemingly remains linear. Additionally, the authors developed a more precise method to quantify bimolecular recombination losses by comparing the EQE profiles with or without the illumination of bias light.<sup>[74]</sup> The illumination of a bias light would increase the charge carrier density of the active layer and represent more actual EQE response in the short-circuit condition. The average ratio of the EQEs measured with and without bias light at different wavelengths can quantitatively reflect the bimolecular recombination losses. The  $\eta_{BR}$  in the short-circuit condition is denoted by

$$\eta_{BR} = \frac{EQE_{nobias}}{EQE_{bias}} - 1 \quad (3.14)$$

Note that  $\eta_{BR}$  only reflects the bimolecular recombination loss in the short-circuit condition, and it gradually accumulates in the maximum power point of PSCs.<sup>[71]</sup>

*Trap-assisted recombination* is a first order process and the recombination rate ( $R_T$ ) is proportional to the charge carrier density ( $R_T \propto p$ , in the case of an electron trap). If trap-assisted recombination loss is dominant, an ideality factor ( $n$ ) greater than unity is expected.<sup>[75]</sup> The ideality factor can be estimated either in the dark ( $n_d$ ) or under illumination ( $n_i$ ).  $n_d$  can be derived from dark  $J$ - $V$  curves and is easier to obtain. However, it was reported that  $n_i$  can be used as a more reliable tool to evaluate the presence of trap-assisted recombination as  $n_d$  is more impacted by the external series resistances and mainly determined by the transport dominating carrier in the blend.<sup>[75-76]</sup> It is also worth noting that  $n_i$  can be smaller than unity originating from the presence of surface recombination at the active layer/contact interface.<sup>[77]</sup>

$n_d$  can be determined from the slope of the exponential regime of dark  $J$ - $V$  curves on a semi-logarithmic plot (Figure 3.6 b). Similarly,  $n_i$  can be determined by measuring the slope of the dependence of  $V_{oc}$  on the logarithm of the  $I$ .<sup>[78]</sup>  $n_d$  and  $n_i$  are described by the following equations:

$$n_d = \frac{q}{kT} \frac{dV}{d \ln(J_d)} \quad (3.15)$$

$$n_i = \frac{q}{kT} \frac{dV_{oc}}{d \ln(I)} \quad (3.16)$$

where  $kT$  is the thermal energy.

For all-PSCs, geminate recombination has been identified as the limiting process.<sup>[79]</sup> However, there is still lack of complete understanding of the dominant recombination losses in all-PSC systems.

## 3.6 Morphology Engineering

### 3.6.1 Desired Active Layer Morphology

Optimal morphology of the active layer blend is crucial to its photophysical properties. In the ideal case, the donor and acceptor domains must have a characteristic spacing less than the diffusion length,  $L_D$ , to maximize charge generation via exciton dissociation. Concomitantly, these domains should be interconnected allowing charge transport to the electrodes without dead-ends or isolated islands that result in the build-up of space charges.<sup>[80]</sup>

Relevant for all-PSCs, the change in the Gibbs free energy ( $\Delta G_{mix}$ ) while two polymers are mixed can be calculated, according to the Flory-Huggins theory, the following equation:<sup>[81]</sup>

$$\frac{\Delta G_{mix}}{Nk_B T} = \frac{\varphi_A}{N_A} \ln(\varphi_A) + \frac{\varphi_B}{N_A} \ln(\varphi_B) + \chi \varphi_A \varphi_B \quad (3.17)$$

where  $\varphi_A$  and  $\varphi_B$  are the volume fraction of polymer A and B, respectively; N is the total number of monomeric units;  $N_A$  and  $N_B$  are the degree of polymerization of polymer A and B, respectively;  $\chi$  is the Flory-Huggins interaction parameter. The first two terms on the right side of equation (3.17) represent the translational entropy ( $\Delta S_T$ ) and the last term represents the enthalpic component.

Thus, compared to small molecule mixtures, the  $\Delta S_T$  of polymers is reduced by a factor of N, reflecting that monomers in the same polymer chain are connected and cannot be positioned independently.

Because of the reduced entropic contribution to the Gibbs free energy by donor and acceptor polymers, it is, in general, energetically favorable for each polymer to interact with its own kind while there is no specific interaction between two different polymer species, resulting in large-scale phase separation and limited exciton diffusion.<sup>[12]</sup>

### 3.6.2 Optimization of Active Layer Morphology

There are many factors that can influence the active layer morphology and they often operate simultaneously in one active layer system. In general, the optimization determinants can be classified in two aspects: a synthetic approach, specially of acceptor polymers, which is the focusing point of this thesis, and a device engineering approach.

#### Synthetic Approach of Acceptor Polymers

*Acceptor polymer main backbone modification:* By modifying the acceptor polymer backbone, the blend morphology can be optimized through tuning the crystallinity of the acceptor polymers. It is speculated that with respect to a given donor polymer, there is an optimal crystallinity of acceptor polymer that endows blend compatibility and boosts the performance of all-PSCs. Larger crystallite and more ordered local structures may lead to enhanced carrier transport in polymer films but in turn result in debilitating exciton dissociation efficiency. The tradeoff between carrier transfer and transport is critical to the device performance. In 2015, Jenekhe *et al.* elucidated the effect of acceptor polymer crystallinity on the performance of all-PSCs.<sup>[82]</sup> A series of NDI-selenophene (Se)/PDI-Se random copolymers, whose crystallinity varied with composition, were investigated as acceptor polymers in all-PSCs. With respect to the donor polymer PBDTTT-CT, the acceptor polymer with 30% PDI-Se leads to the optimal blend morphology, balancing charge carrier mobilities, resulting in the highest PCE. Later, Ma *et al.* further proposed that the crystallinity of the donor and acceptor should be similar to form suitable phase separation.<sup>[83]</sup> They investigated all-PSCs based on the moderately crystalline donor polymer PTP8, blended with acceptor polymers PNDI-2T, PNDI-Se and PNDI-2Se, respectively. Compared to the more crystalline acceptor polymers PNDI-2T and PNDI-2Se, the acceptor polymer PNDI-Se with similar crystallinity to the donor polymer resulted in an optimal blend morphology, with the best performance of 6%. Recently, Chen *et al.* further attested to the validity of this crystallinity control strategy through acceptor polymer backbone modification, specifically through random copolymer design.<sup>[84]</sup>

*Acceptor polymer side chain engineering:* The side chains of conjugated polymers possess multiple functions of modulating the properties of resultant conjugated polymers, including the ability to affect molecular weight, self-assembly (intramolecular interactions), optoelectronic properties (light absorptivity, charge transport behavior) and film morphology, which in turn, will significantly affect the performance.<sup>[85]</sup> But compared to the extensive efforts spent on improving conjugated backbones, the side chain engineering of *n*-type polymers has not been given due attention. In 2015, Kim *et al.* emphasized the importance of engineering alkyl side chains of NDI-based acceptor polymers for producing efficient all-PSCs. They demonstrated that the acceptor polymer PNDIT-HD with relatively short 2-hexyldecyl (HD) side chains could form highly ordered, strong face-on interchain stacking, showing better intermixed BHJ morphology in the PTB7-Th:PNDI-HD blend. This desirable film

morphology led to PCE around 6% in the PTB7-Th:PNDI-HD all-PSC device, which was the record value reported for all-PSCs at that time.<sup>[86]</sup> However, Jen *et al.* later observed the opposite trend to what was described above for the short side chain-containing polymer. Thus, they reported that the acceptor polymer P(NDI2OD-FT2) with longer alkyl side chain possessed highly crystalline nanostructures with a preferential face-on orientation, forming desirable film morphology and 6.71% PCE in all-PSC devices.<sup>[87]</sup> Recently, Kim *et al.* reported the effect of side chain engineering of acceptor polymers based on phenylnaphthalenediimide (PNDI) building blocks. Interestingly, all-PSCs based on the acceptor polymer with 2-butyloctyl (BO) side chains (medium-length alkyl chains) exhibited the highest PCE of 4.25%, benefiting from the well-mixed blend morphology.<sup>[88]</sup> Overall, these results showed that there are still many unknown factors in determining chain packing of conjugated polymers.

*Molecular weight effect:* In fullerene-based PSCs, it is well-known that molecular weight exerts a profound influence on macromolecular ordering, microstructure, optoelectronic and charge transport characteristics, making it one of the key parameters governing device performance. Donor polymers with higher molecular weights typically show higher degrees of ordering, resulting in enhanced light absorption and  $\mu_h$ , as well as higher  $J_{sc}$  and FF. In all-PSCs, there is a clear relationship between the number-average molecular weight ( $M_n$ ) and the crystalline behaviors of the polymers. There have been studies which revealed that the performances of all-PSC devices could be improved by increasing the molecular weight of the acceptor polymer.<sup>[89]</sup> Marks *et al.* reported that increasing the  $M_n$  values of both semicrystalline donor and semicrystalline acceptor polymers simultaneously transformed the polymer domains from relatively ordered, highly crystalline, and largely phase-separated to a relatively disordered and amorphous morphology. The highest PCE was actually achieved for the donor and acceptor blend with an intermediate  $M_n$ .<sup>[90]</sup> On the one hand, increasing the  $M_n$  of both polymers shrank blend film domain sizes and enhanced donor-acceptor polymer-polymer interfacial areas, which resulted in enhanced exciton dissociation, affording increased  $J_{sc}$ . On the other hand, random, disordered blend morphology contributed to a high degree of recombination and lower FF. However, they claimed that the performance of the all-PSC containing an amorphous donor polymer with medium molecular weight was nearly constant, regardless of the molecular weight of the semicrystalline acceptor, which is in stark contrast to their earlier findings for two semicrystalline polymers.<sup>[91]</sup>

### Device Engineering Approach

During the fabrication of devices, the film morphology can be controlled by changing the film processing parameters. However, it is also important to note that this promising strategy is more empirical and can vary from case to case.

*Processing solvents and additives:* The kinetics of blend film formation can be controlled through choice of proper processing solvents and additives to optimize the morphology. An intermediate state of mixing can be frozen into the solid state if there is insufficient time for complete phase separation of the polymer blend. Ito *et al.* reported that the use of the low boiling point solvent chloroform (CF) to process the all-PSC device based on a semi-crystalline donor P3HT and an amorphous acceptor PF12TBT could suppress the spontaneous growth of phase separation during the spin coating process, leading to increased  $J_{sc}$  and overall performance.<sup>[92]</sup> Friend *et al.* demonstrated that the use of 4-

bromoanisole (BrAni) as an additive could facilitate the crystallization of P3HT, and improve the morphology of the P3HT-containing blend, which resulted in enhanced performances of the all-PSCs.<sup>[93]</sup> Furthermore, additives such as 1,8-diiodooctane (DIO),<sup>[94]</sup> diphenyl ether (DPE),<sup>[95]</sup> 1-chloronaphthalene (CN),<sup>[96]</sup> and 6,6'-dithiopheneisoindigo (DTI)<sup>[97]</sup> were also shown to improve the device performance with optimized blend morphology through modulating the aggregation of donor or acceptor polymers in different active layer systems. In addition, Zhan *et al.* reported that the performances of all-PSCs could be enhanced by the utilization of binary additives. In this scenario, the non-volatile additive PDI-2DTT suppressed aggregation of the acceptor polymer, while DIO facilitated crystallization of the donor polymer. Consequently, suitable phase separation, improved and balanced charge carrier mobilities, and, therefore, boosted PCE could be achieved.<sup>[98]</sup> Recently, a new pentafluorobenzene-based additive (FPE) was demonstrated to improve the performances of all-PSCs by controlling the D:A interfacial morphology.<sup>[99]</sup> Overall, the role of the additive or a good processing solvent is to provide better  $\pi$ - $\pi$  packing of polymer chains as well as to achieve the required sizes of polymer domains.<sup>[100]</sup>

*Post-treatment of the active layer film:* Post-treatments like thermal annealing and film aging provide convenient means of tuning the donor or acceptor domain size. Previously, Ito *et al.* showed through photoluminescence (PL) quenching measurements, that thermal annealing caused two-step structural changes in P3HT:PF12TBT blend all-PSCs.<sup>[92]</sup> Thermal treatment below 120 °C induced homogeneity between donor and acceptor in the mixed blend film, keeping the domain size close to  $L_D$ . In this regime,  $J_{sc}$  increased at elevated temperature, leading to improved PCE. While thermal treatment above 120 °C caused further growth of domain size beyond  $L_D$  and a decrease in domain interface area, resulting in a reduction in device performance. Later, thermal annealing and film aging were proven to be effective in optimizing blend morphology and enhancing all-PSCs performance with improved charge carrier mobilities.<sup>[101]</sup>

### 3.7 Active Layer Polymers Design Criteria

Overall, there are several key parameters for active layer polymers that need to be simultaneously controlled to achieve high-performance all-PSCs:

- Reasonable solubility in organic solvents to ensure their solution-processability.
- Strong light absorption in the visible range and complementary absorption spectra between donor and acceptor polymers to achieve optimal light harvesting and increased  $I_{ph}$ .
- Suitable frontier energy levels to facilitate effective charge generation and increase  $V_{oc}$ .
- High  $\epsilon_r$  to lower exciton binding energies, hence mitigating geminate recombination.
- High  $\mu_e$  to enhance the electron transporting property and facilitate extraction prior to recombination and thus allow for thicker photovoltaic layers.
- Proper miscibility to form nanoscale phase-separated morphologies with bicontinuous pathways of donor and acceptor polymer domains for efficient charge transport and collection.

## 4 Synthesis and Characterization of Naphthalene Diimide-based Acceptor Polymers for All-PSCs

---

### 4.1 Background and Motivation

The most popular non-fullerene acceptor used in all-PSCs has been the naphthalene diimide (NDI)-based polymer poly[[N,N'-bis(2-octyldodecyl)-naphthalene-1,4,5,8-bis(dicarboximide)-2,6-diyl]-*alt*-5,5'-(2,2'-bithiophene)] with the commercial name N2200. It is popular because it displays high  $\mu_e$ , good solubility and strong absorption in the visible and NIR region.<sup>[61,89b,102]</sup> The PCE of PTB7-Th:N2200 all-PSCs has been steadily improving, recently reaching 5.7%.<sup>[103]</sup> Moreover, the development of wide bandgap donor polymers, which exhibit complementary absorption with N2200 has boosted the PCE of all-PSCs to 10%.<sup>[61,102b]</sup> Nonetheless, there is still room for further improvement of the all-PSC performances through rational design of the structures of acceptor polymers and device engineering. As mentioned in Section 3.2.1, the three characteristics  $V_{oc}$ ,  $J_{sc}$ , and FF should be modulated to increase PCE:

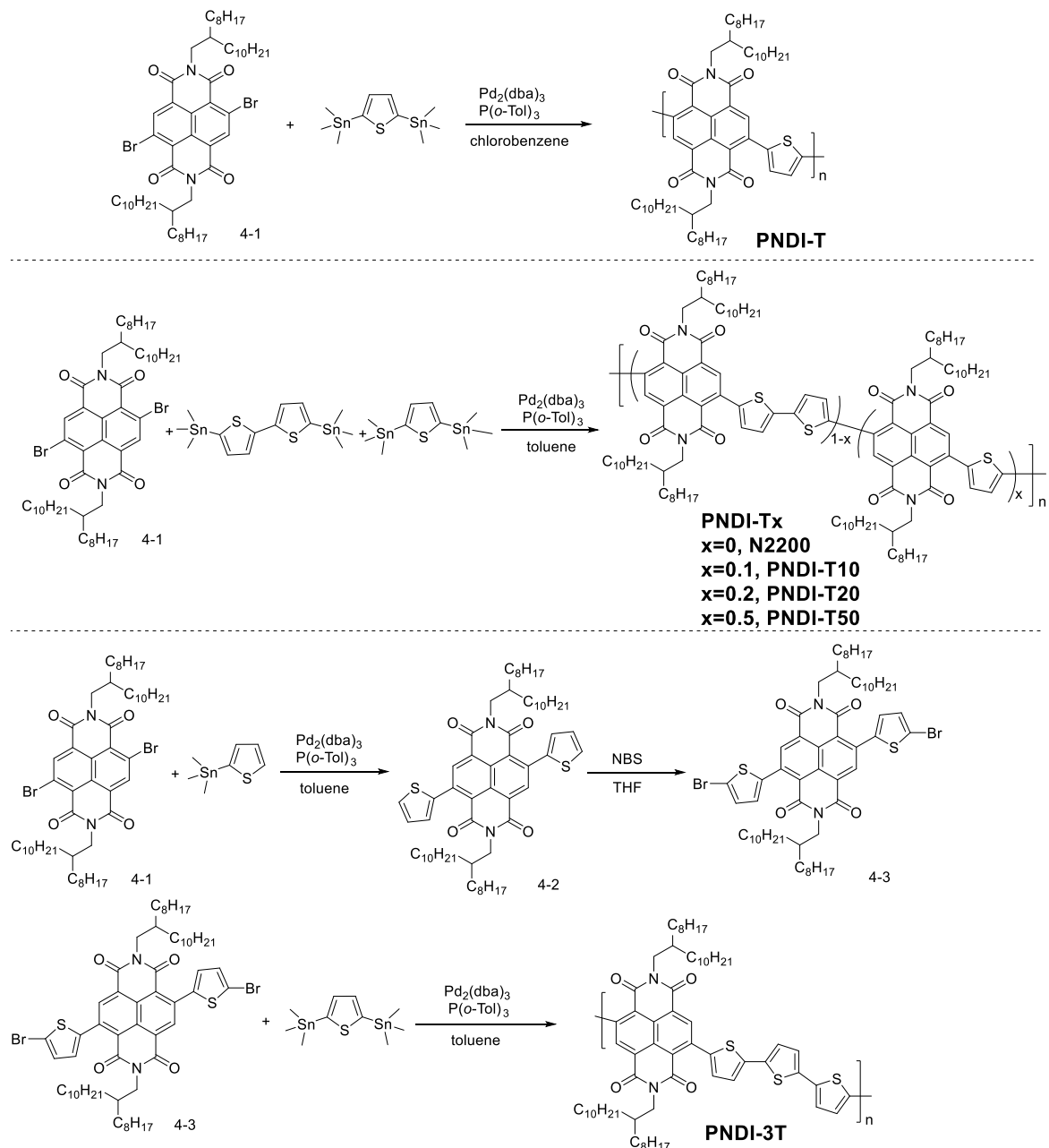
- N2200 blends easily form big domains and large phase separation due to the high crystallinity of N2200, which leads to increased charge recombination and limits the all-PSC performance. Therefore, modifying the crystallinity of N2200 by incorporating flexible moieties in the backbone may lead to suitable miscibility with donor polymers, increase the FF, and improve the all-PSC performance.
- By utilizing properly matched donor and acceptor polymers, the absorption spectra can be broadened, which can further increase the  $J_{sc}$ , and improve the performance of all-PSCs in the optimal morphology condition.
- Since the LUMO level of N2200 is similar to that of PC<sub>71</sub>BM, further optimization is possible by uplifting the LUMO level of N2200 and utilizing donor polymers with low-lying HOMO levels to maximize the  $V_{oc}$ .
- Ternary blends incorporating two donors and one acceptor (or one donor and two acceptors) have been utilized as an effective strategy to improve the performance of fullerene-based PSCs. However, there are few successful examples of ternary all-PSCs, since polymer blends tend to result in large phase separation due to the reduced translational entropy as discussed in Section 3.6. Whereas, good miscibility with nano-scale phase separation can be achieved in ternary systems by choosing suitable donor and acceptor polymers, and proper device engineering. Complementary absorption in ternary blends can overcome the absorption limit and boost the PCE of all-PSCs

To address the above approaches, a series of NDI based acceptor polymers were synthesized. The acceptor polymers were scrutinized with respect to crystallinity, absorption, and energy levels. These properties were correlated to photovoltaic performance by studying film morphology, exciton dissociation, charge transport processes and charge recombination.

## 4.2 Acceptor Polymers Synthesis and Characterization

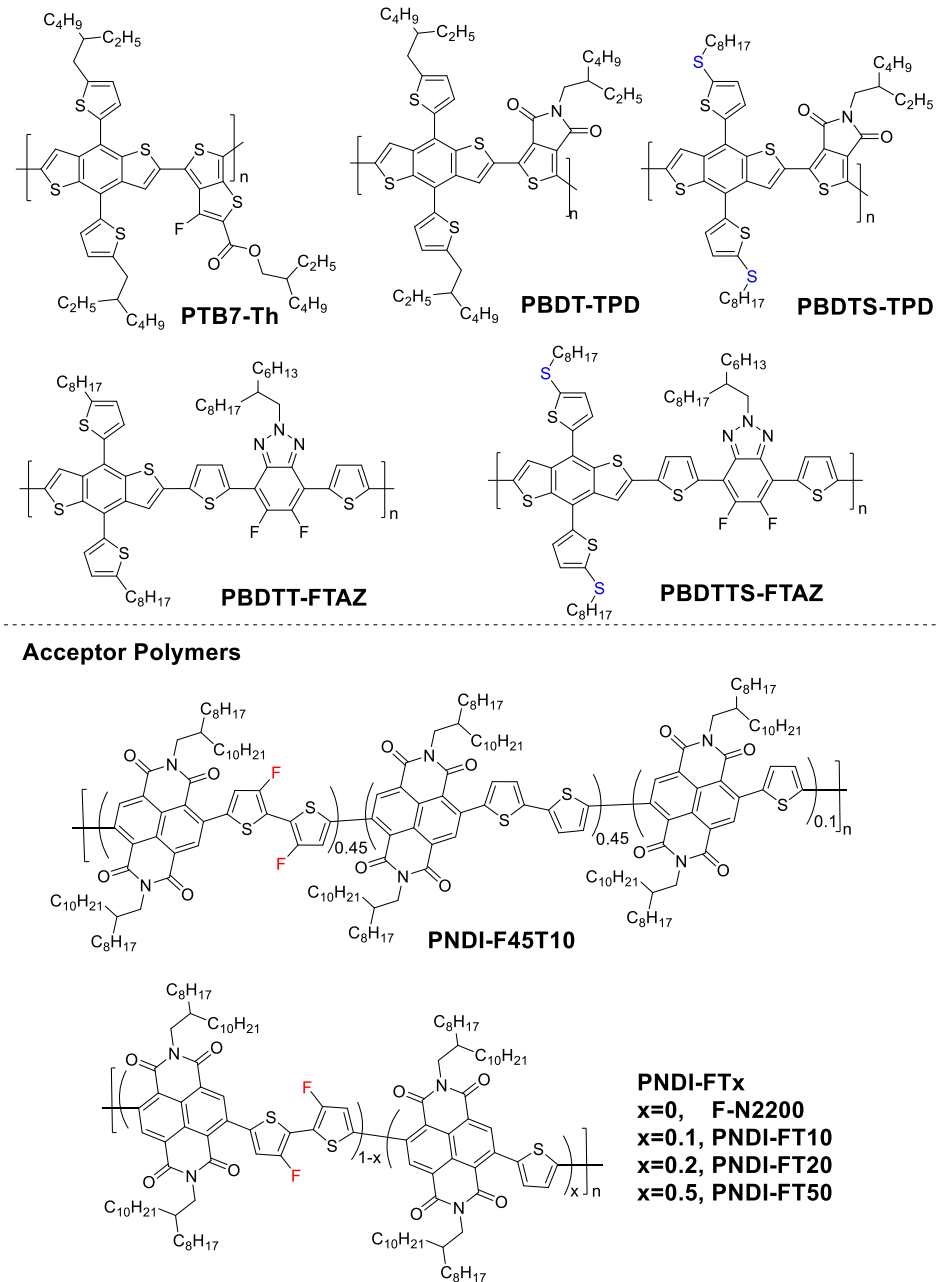
The NDI-based acceptor polymers were all synthesized by Stille coupling polymerizations, and the synthetic routes are shown in Scheme 4.1. The acceptor polymer PNDI-T was synthesized through microwave-assisted Stille coupling reaction to increase the molecular weight, since the strong steric hindrance between NDI and T units led to a smaller molecular weight when ordinary polymerization procedures were employed. The random copolymer PNDI-T<sub>x</sub> was synthesized by introducing different amounts of single thiophene, T, units to replace the bithiophene (2T) units as electron-donating units in the N2200 polymer backbone, where x stands for the molar percentage of T units relative to total donor units. The random copolymers were expected to exhibit more flexible backbones and lower crystallinity due to their reduced regularity in the main chains. The chemical structures of other donor and acceptor polymers described in this chapter are illustrated in Scheme 4.2. Polymer PTB7-Th was purchased from Solarmer Energy, Inc. Polymers PBDTT-FTAZ and PBDTTS-FTAZ were synthesized by Zewdneh Genene, Addis Ababa University. The remaining polymers in Scheme 4.2 were synthesized by Xiaofeng Xu, Chalmers.

The molecular weights and polydispersity indices (PDs) of the polymers, summarized in Table 4.1, were measured via gel permeation chromatography (GPC) in 1,2,4-trichlorobenzene at 150 °C. Donor polymers PBDTT-FTAZ, PBDT-TPD and PBDTTS-TPD, and acceptor polymer PNDI-T displayed good solubility in common organic solvents, like CF, chlorobenzene (CB), and *o*-dichlorobenzene (*o*DCB) at room temperature, due to their relatively low molecular weights. Other polymers showed poor solubility in CF, but were well-soluble in CB and *o*DCB at 70 °C.



Scheme 4.1 Synthetic routes of NDI-based acceptor polymers

## **Donor Polymers**



Scheme 4.2 Chemical structures of donor polymers and other acceptor polymers described in this chapter. (Some atoms are marked in different colors to highlight the difference.)

The optical absorption properties of the donor and acceptor polymers were characterized via UV-vis-NIR absorption spectroscopy. The absorption maxima ( $\lambda_{\max}$ ) and  $E_g^{\text{opt}}$  of all polymer thin films are summarized in Table 4.1. Owing to the enhanced  $\pi-\pi$  stacking and intermolecular interactions in the solid state, red-shifted absorption spectra were found for all the polymers in films as compared to the spectra in solution. The NDI-based acceptor polymers showed two distinct absorption bands at 300–400 nm and 500–700 nm, which arise from the  $\pi-\pi^*$  manifold excitations and correspond to transitions within local NDI and intramolecular charge transfer (ICT) characteristics.<sup>[104]</sup> The fluorinated polymer F-N2200 displayed slightly blue-shifted absorption spectra compared to the non-fluorinated N2200 and the  $\lambda_{\max}$  of the ICT  $\pi-\pi^*$  bands for F-N2200 and N2200 were around 684 nm and 698 nm, respectively.

Among the non-fluorinated acceptor polymers, increasing the fraction of T units in the polymer backbone of NDI-based acceptor polymers resulted in a gradual blue shift of the  $\lambda_{\text{max}}$  from 698 nm in N2200 to 644 nm in PNDI-T50. The absorptions of the fluorinated acceptor polymers showed the same trend. In addition, a red shift of the absorption maximum was observed, when the donor length of the acceptor polymer was increased from one to two and to three T units.

The absorption spectra for the similar donor polymers PBDTT-FTAZ and PBDTTS-FTAZ presented the same  $\lambda_{\text{max}}$  at 598 nm. However, the donor polymer PBDTS-TPD exhibited a red-shifted and broadened absorption spectrum as compared to the related PBDT-TPD. The difference is presumably due to the promoted packing of polymer chains induced by the linear alkylthio side chains on PBDTS-TPD.

Table 4.1 Molecular weights and optical properties of the polymers

Polymer	$M_n$ (kDa)	PD	$\lambda_{\text{max}}^{\text{d}}$ (nm)	$E_g^{\text{opt}}$ (eV)	$T_m$ (°C)	$T_c$ (°C)
PBDTT-FTAZ	13.7	2.1	598	1.91	-	-
PBDTTS-FTAZ	22.6	3.2	598	1.94	-	-
PTB7-Th <sup>a</sup>	35.0	3.0	700	1.60	-	-
PTB7-Th <sup>c</sup>	45.7	2.2	700	1.60	-	-
PBDT-TPD	28.9	2.9	614	1.87	-	-
PBDTS-TPD	24	3.6	619	1.85	-	-
PNDI-T	43.6	1.8	600	1.83	240	222
PNDI-T50	41.9	3.1	644	1.60	227	206
PNDI-T20	67.7	5.0	680	1.56	266	236
PNDI-T10 <sup>a</sup>	66.6	5.0	694	1.55	290	267
PNDI-T10 <sup>b</sup>	41.9	2.8	694	1.55	-	-
PNDI-T10 <sup>c</sup>	83.5	2.5	694	1.55	-	-
N2200	30.5	3.8	698	1.47	305	280
PNDI-3T	37.1	3.0	707	1.45	300	277
PNDI-F45T10	79.1	2.3	677	1.53	-	-
PNDI-FT50	84.7	2.1	626	1.60	-	-
PNDI-FT20	78.8	2.2	648	1.58	-	-
PNDI-FT10	58.6	2.2	679	1.57	-	-
PNDI-FT10 <sup>c</sup>	60.2	2.3	679	1.57	-	-
F-N2200	51.6	1.9	684	1.55	-	-

<sup>a</sup> refers to the first batch used in paper I, II, III and IV. <sup>b</sup> refers to the batch used in paper VI. <sup>c</sup> refers to the batch used in paper VII. <sup>d</sup> absorption maximum of the thin film.

The LUMO and HOMO energy levels of the donor and acceptor polymers are depicted in Figure 4.1. The non-fluorinated NDI-based acceptor polymers showed similar LUMO levels around -4.05 eV, which stems from the dominant contribution of the electron-withdrawing NDI units. Upon increasing the donor length of the polymers from one to two, and to three T units, the LUMO level slightly downshifted from -4.04 eV to -4.08 eV, while the HOMO level upshifted from -6.52 eV to -6.22 eV. Consequently, the  $E_g$  decreased, in accordance with the narrowing of  $E_g^{\text{opt}}$ . The fluorinated polymers exhibited low-lying LUMO levels compared to the corresponding non-fluorinated polymers, which can be attributed to the strong electron-withdrawing property of fluorine.

With regards to donor polymers, the HOMO level of PBDTTS-FTAZ was lowered by 0.2 eV compared to that of PBDTT-FTAZ, presumably due to the less electron-donating effect of the alkylthio side chains on the benzodithiophene (BDT) moiety. Although the inclusion of a sulfur atoms on the side chains of the BDT unit can down-shift the HOMO level of the polymer, it was evidenced that the linear octylthio-substituted BDT polymer had a slightly up-shifted HOMO level as compared to the branched 2-ethylhexylthio-substituted analogue.<sup>[105]</sup> Thus, only a slight decrease in the HOMO level of PBDTS-TPD was found compared to PBTD-TPD, which can be explained by the combined effects of the sulfur atoms and linear octyl side chains.

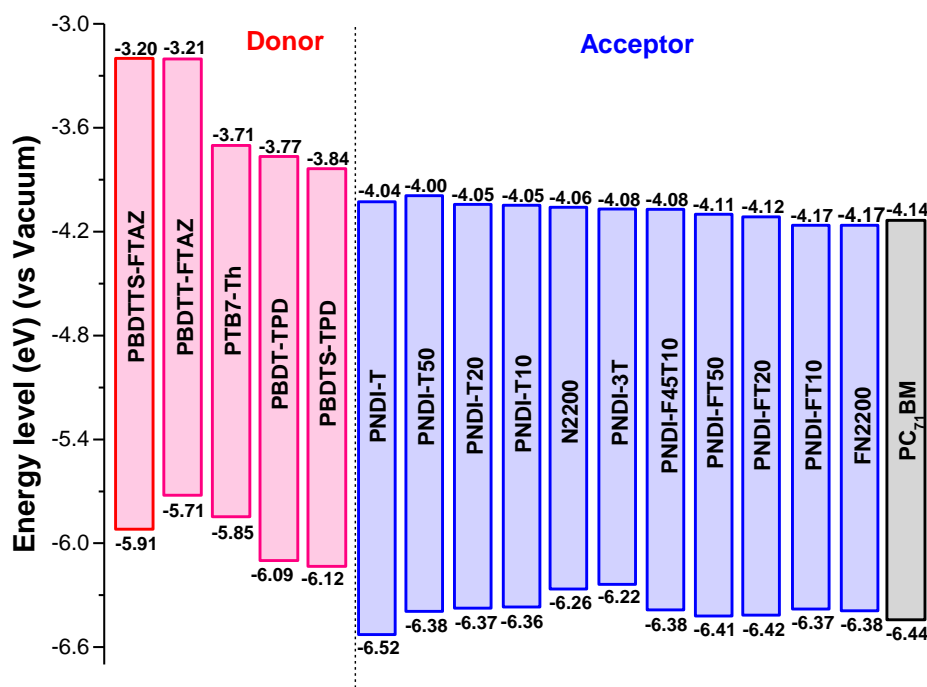


Figure 4.1 Energy level diagram of the polymers described in this chapter.

Differential scanning calorimetry (DSC) was used to determine the solid-state thermal transitions of donor and acceptor polymers. The donor polymers exhibited no clear thermal transitions along the heating and cooling cycle, suggesting that they are mostly amorphous in the solid state. All non-fluorinated acceptor polymers presented a clear melting transition upon heating and a crystallization transition upon cooling. The melting temperature ( $T_m$ ) of N2200 was as high as 305.3 °C, indicating a highly crystalline behavior. The DSC curves of non-fluorinated acceptor polymers are depicted in Figure 4.2, and the thermal transition parameters are summarized in Table 4.1. Inclusion of single T units in the backbone gradually reduced the  $T_m$  and crystallization temperature ( $T_c$ ) of the polymers, which indicates that the rigidity or chain stacking of the polymers is weakened due to increased backbone disorder. In contrast, none of the fluorinated polymers presented detectable thermal transitions in the temperature range of 0–320 °C.

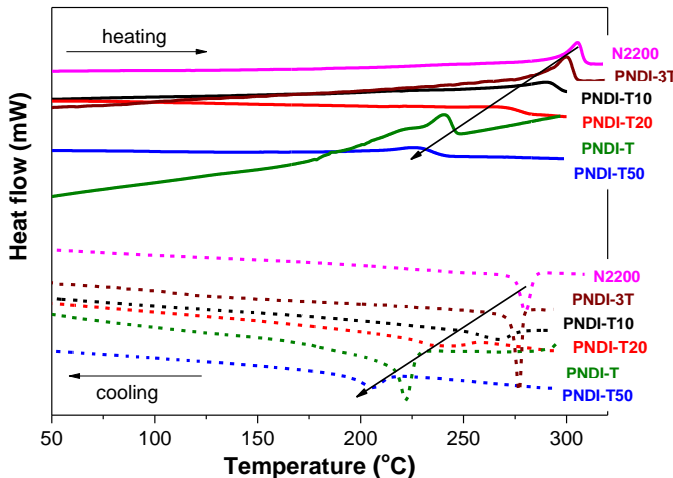


Figure 4.2 DSC thermograms of neat PNDI-T, N2200, PNDI-3T, and PNDI-T<sub>x</sub>, measured with a scan rate of 10 °C per min.

### 4.3 Results and Discussion on All-PSCs

In principle, donor and acceptor polymers with complementary absorption spectra (for high  $J_{ph}$ ), well-matched energy levels (to enabling high  $V_{oc}$ ), desired polymer miscibility (for reduced charge recombination and improved FF), and balanced charge transport can be realized through rational design, which should lead to high PCEs for all-PSCs. In this section, four approaches, *viz*, crystallinity modification of acceptor polymers, utilization of donor and acceptor polymers with complementary absorption, energy levels modulation and ternary approach are discussed in detail.

#### 4.3.1 Crystallinity Modification Approach to Improve the FF

The FFs of all-PSCs based on polymer:N2200 blends are often limited due to the suboptimal morphology with large phase separation, which is caused by the high crystallinity of N2200. In consequence, different solvents and post-treatment procedures are applied on different polymer:N2200 blends to optimize the nanostructure of the active layer and improve the all-PSC performance.<sup>[106]</sup> While there are evidences that the incorporation of flexible moieties or different side chain modulation techniques on NDI-based acceptor polymers can modify crystallinity and lead to suitable miscibility, developing rational methods to better control the crystallinity of N2200 backbone may have a major impact on the performance of the resulting all-PSC.<sup>[82,107]</sup> Therefore, the PNDI-T<sub>x</sub> and PNDI-FT<sub>x</sub> series were utilized as described in this Section to investigate the effect of acceptor polymer crystallinity on the performances of all-PSCs. The results presented herein have been extractd from Paper I and Paper VI.

The polymer PTB7-Th was selected as the electron donor material, since PTB7-Th:N2200 blend showed very promising properties with high photovoltaic performance. Both conventional and inverted all-PSCs were fabricated to evaluate the photovoltaic performances. Interestingly, conventional all-PSCs fabricated from non-fluorinated acceptors exhibited superior performance compared to inverted devices, while all-PSCs fabricated from fluorinated acceptor polymers showed opposite trends. All the active layers were processed from CB solution and the optimized D:A ratio was 1:1 (w:w). The

photovoltaic parameters of the optimized all-PSCs are summarized in Table 4.2, and the detailed photovoltaic parameters, under different processing conditions, can be found in Paper I and Paper VI. The variations of the  $V_{oc}$ s of all-PSCs based on different acceptor polymers can be well-explained by the changes of the LUMO levels of the acceptor polymers as discussed in the previous section (Figure 4.1). Both the F-N2200- and PNDI-FT10-based all-PSCs exhibited 0.09 V lower  $V_{oc}$ , compared to the corresponding non-fluorinated N2200- and PNDI-T10-based all-PSCs, respectively. Among the series of non-fluorinated acceptor polymer-based all-PSCs, the PTB7-Th:PNDI-T10 blend attained the highest PCE of 5.6% with a  $J_{sc}$  of 12.7 mA/cm<sup>2</sup>, and FF of 0.54. This enhanced PCE suggests that inclusion of small amounts of T units in the polymer backbone affords a better counterpart for the PTB7-Th donor. The same trend was also observed among fluorinated acceptor polymer-based all-PSCs, where the PTB7-Th:PNDI-T10 blend accomplished the highest PCE of 6.3% with an increased  $J_{sc}$  of 14.4 mA/cm<sup>2</sup>, and FF of 0.60. After trying several film processing approaches, like thermal annealing and use of additives, solvent annealing (SA) turned out to be the most effective method to improve the performance of PNDI-T10- and PNDI-FT10-based all-PSCs, and led to superior PCEs above 7%. During the SA process, the slow solvent evaporation rate provides both donor and acceptor polymers with longer molecular rearrangement time, which renders a well-organized nanostructure and improved FF of all-PSCs. On the other hand, despite the high PCEs achieved through the random acceptor polymers PNDI-T10 and PNDI-FT10, it is necessary to be aware of the effects of molecular weights and batch-to-batch variations on the performance of all-PSCs (Table 4.2).

Table 4.2 Photovoltaic parameters of the optimized all-PSCs.

A	d (nm)	$V_{oc}$ (V)	$J_{sc}$ (mA/cm <sup>2</sup> )	FF	PCE (%)	SCLC $\mu_h$ (cm <sup>2</sup> V <sup>-1</sup> s <sup>-1</sup> )	SCLC $\mu_e$ (cm <sup>2</sup> V <sup>-1</sup> s <sup>-1</sup> )	$\mu_h/\mu_e$
N2200 <sup>a</sup>	90	0.81	9.4 (8.7) <sup>d</sup>	0.49	3.7	$2.0 \times 10^{-3}$	$2.0 \times 10^{-4}$	10
PNDI-T10b <sup>a</sup> SA <sup>c</sup>	90	0.82	12.9 (12.1)	0.65	6.9	-	-	-
PNDI-T10a <sup>a</sup>	95	0.82	12.7 (12.4)	0.54	5.6	$8.5 \times 10^{-4}$	$4.3 \times 10^{-4}$	2
PNDI-T10a <sup>a</sup> SA	95	0.83	12.9 (12.5)	0.71	7.6 (7.4) <sup>e</sup>	$1.0 \times 10^{-3}$	$6.0 \times 10^{-4}$	1.7
PNDI-T20 <sup>a</sup>	95	0.83	9.7 (9.2)	0.52	4.2	$8.4 \times 10^{-4}$	$1.4 \times 10^{-4}$	6
PNDI-T50 <sup>a</sup>	95	0.83	5.8 (5.2)	0.48	2.3	$8.2 \times 10^{-4}$	$9.5 \times 10^{-5}$	9
F-N2200 <sup>b</sup>	90	0.72	12.9 (12.3)	0.58	5.4	$5.0 \times 10^{-4}$	$1.7 \times 10^{-4}$	2.9
PNDI-FT10 <sup>b</sup>	95	0.73	14.4 (14.2)	0.60	6.3	$6.5 \times 10^{-4}$	$2.2 \times 10^{-4}$	3.0
PNDI-FT10 <sup>b</sup> SA	95	0.73	14.6 (14.4)	0.68	7.2 (6.9)	-	-	-
PNDI-FT20 <sup>b</sup>	90	0.74	11.8 (11.8)	0.53	4.6	$2.8 \times 10^{-4}$	$1.8 \times 10^{-4}$	1.6
PNDI-FT50 <sup>b</sup>	85	0.77	5.6 (5.6)	0.49	2.1	$1.1 \times 10^{-4}$	$1.0 \times 10^{-4}$	1.1

<sup>a</sup> Conventional device structure. <sup>b</sup> Inverted device structure. <sup>c</sup> Solvent annealing. <sup>d</sup>  $J_{ph}$  obtained by integrating the EQE with the AM1.5G spectrum are given in the parentheses <sup>e</sup> The average PCE from ten devices

The charge carrier mobilities of active layer blends were characterized through space charge limited current (SCLC) method to investigate the charge transport in the all-PSCs. As summarized in Table 4.2, the PTB7-Th:PNDI-T10 blend showed more balanced  $\mu_h/\mu_e$  among the active layers consisting of non-fluorinated acceptors. The slightly higher  $\mu_e$  of PTB7-Th:PNDI-T10 compared to that of PTB7-Th:N2200 is likely related to the much higher molecular weight of PNDI-T10, which often contributes to the enhancement of the mobilities of conjugated polymers.<sup>[108]</sup> The balanced charge carrier mobilities could reduce bimolecular recombination in the all-PSCs, and lead to higher  $I_{ph}$ , which agrees well with the higher  $J_{sc}$  of PNDI-T10-based all-PSC. In contrast, all active layers comprising fluorinated acceptors showed relatively high and well-balanced charge carrier mobilities in the order of  $10^{-4} \text{ cm}^2 \text{ V}^{-1} \text{ s}^{-1}$ . This indicates that mobility is not a limiting factor for photovoltaic performance in this system.

To gain a clear understanding of the exciton dissociation process, photoluminescence (PL) quenching of the blend films was measured. The steady-state PL quenching efficiency ( $\Delta PL$ ) can be inferred using the following equation:

$$\Delta PL = 1 - \frac{PL_{blend}}{PL_{polymer}} \quad (4.1)$$

where  $PL_{blend}$  and  $PL_{polymer}$  are the integral PL counts of the blends and neat polymer films, respectively.

$\Delta PL$  reflects the efficiency of exciton dissociation at the D:A interface. Higher  $\Delta PLD$  ( $\Delta PL$  relative to the donor PTB7-Th) and  $\Delta PLA$  ( $\Delta PL$  relative to the acceptor polymers) values indicate that more efficient charge transfer occurred, due to optimal polymer miscibility in this blend. As depicted in Figure 4.3, the PL emission from PTB7-Th was almost quenched completely in all four blends, inferring that there was no large phase separation in each blend film. Compared to the rigid D-A copolymers N2200 and F-N2200, however, the random copolymers PNDI-T10 and PNDI-FT10 (with 10% T units in the polymer backbone) showed more efficient charge transfer. It is also worth noting that high  $\Delta PLAs$  of 87% and 95% were observed in the fluorinated blends PTB7-Th:F-N2200 and PTB7-Th:PNDI-FT10, respectively, while the two non-fluorinated blends PTB7-Th:N2200 and PTB7-Th:PNDI-T10 presented moderate  $\Delta PLAs$  of 65% and 80%, respectively. Since similar morphology was revealed by fluorinated and non-fluorinated acceptor-based active layers, the enhanced  $\Delta PL$  can probably be attributed to the reduced binding energy caused by the improved  $\varepsilon_r$  of fluorinated acceptor polymers (refer to Paper I and Paper VI).

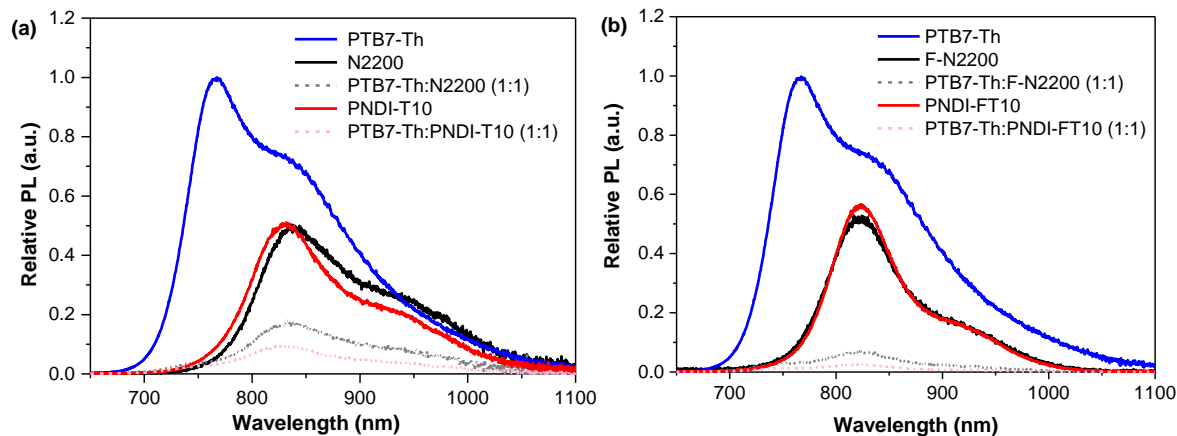


Figure 4.3 The proportional PL counts of the neat polymer and blend films.

The bimolecular recombination loss was quantified by measuring the EQE profiles with and without the illumination of bias light. The  $\eta_{BR}$  was calculated according to equation (3.14), and is shown in Figure 4.4. The PNDI-T10-based all-PSC showed a much lower  $\eta_{BR}$  of 0.04 compared to other non-fluorinated acceptor-based devices, implying negligible bimolecular recombination in this system. A similar trend was also found among fluorinated acceptor-based all-PSCs.

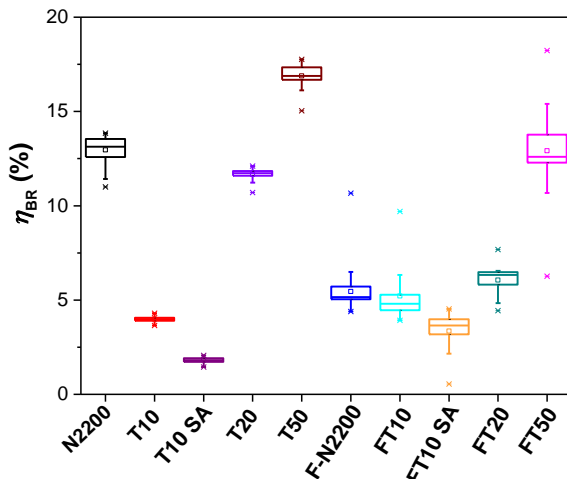


Figure 4.4 Average  $\eta_{BR}$  of the all-PSCs with different acceptor polymers.

In summary, compared to the rigid D-A copolymers N2200 and F-N2200, the random copolymers PNDI-T10 and PNDI-FT10 turned out to be better counterparts for the PTB7-Th donor, and formed the desired nanoscale blend morphology with reduced bimolecular recombination, which led to high PCEs over 7%. Since the random copolymers PNDI-T10 and PNDI-FT10 showed similar optical and electrochemical properties as the rigid D-A copolymers N2200 and F-N2200, the improved performance of all-PSCs can be attributed to the modification of acceptor polymer crystallinity. As hypothesized, the introduction of disorder on the acceptor polymer backbones turns out to be a facile method to potentially benefit the photovoltaic performance.

#### 4.3.2 The Complementary Absorption Approach to Increase the $J_{sc}$

Although the PTB7-Th:PNDI-T10 all-PSC achieved a high PCE of over 7% as discussed in Section 4.3.1, the absorption spectrum of the acceptor PNDI-T10 almost completely overlapped with that of the donor PTB7-Th. Additionally, both PTB7-Th and PNDI-T10 presented weak absorption in the visible region, indicating that the photons would not be fully utilized in this spectral range. Therefore, it is desirable to utilize a high band gap donor polymer with strong absorption in the visible region, that is complementary with the absorption of PNDI-T10, to further improve the  $J_{sc}$ . Also, since the PTB7-Th:PNDI-T10 all-PSCs afforded significantly improved performance compared to PTB7-Th:N2200 all-PSCs, it would be interesting to also compare PNDI-T10 with N2200, where the donor polymers present complementary absorption spectra. Therefore, two high band gap polymers PBDTT-FTAZ and PBDTTS-FTAZ, developed in our group, with good performance when blended with PC<sub>71</sub>BM, were utilized as donors.<sup>[109]</sup> Three NDI-based polymers, PNDI-T, PNDI-T10 and N2200, exhibiting diverse optical properties and energy levels, were used as acceptors. The results presented in this Section are based on Paper III.

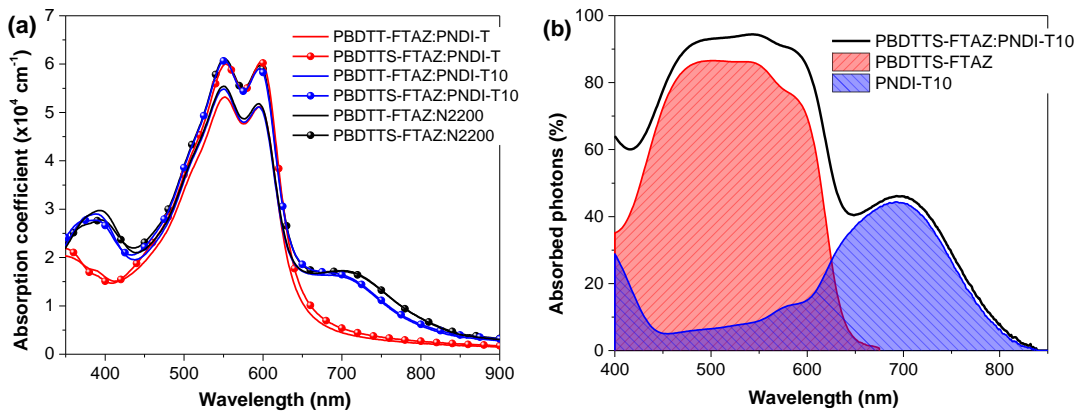


Figure 4.5 (a) Absorption coefficient of the D:A (2:1, w:w) blends in films; (b) Simulated absorptance of the PBDTTS-FTAZ:PNDI-T10 (2:1, w:w) blend in an inverted all-PSC (black line) and the divided absorptance of PBDTTS-FTAZ (red line) and PNDI-T10 (blue line) in the active layer. (adapted from Paper III)

The absorption coefficients of the D:A (2:1, w:w) blend films are depicted in Figure 4.5 a. The three blends containing PBDTTS-FTAZ displayed slightly higher  $\alpha$  than those based on PBDTT-FTAZ, presumably because of the higher  $\alpha$  of PBDTTS-FTAZ. Each of the PNDI-T10- and N2200-based blend film presented one main absorption peak stemming from the donor polymers, where the small shoulder at ca. 710 nm comes from the absorptions of the acceptor polymers. In contrast, only one absorption peak was observed in each of the PNDI-T-based blends. Since the  $\alpha$  of the acceptor polymers were much lower than that of the donor polymers, one might assume that the contributions to light harvesting by acceptor polymers were much lower. Therefore, a simple method to calculate the actual light harvesting contribution of the two components in a blend film was developed. Taking PBDTTS-FTAZ:PNDI-T10 blend as an example, as shown in Figure 4.5 b, the simulated absorptance of the active layer was divided to that of the individual donor and acceptor polymers, as described by Equation (4.3) and (4.4):

$$A_D(\lambda) = \frac{f_D k_D(\lambda)}{f_D k_D(\lambda) + f_A k_A(\lambda)} A(\lambda) \quad (4.2)$$

$$A_A(\lambda) = \frac{f_A k_A(\lambda)}{f_D k_D(\lambda) + f_A k_A(\lambda)} A(\lambda) \quad (4.3)$$

where  $f_D$  and  $f_A$  are the volume fractions of the donor and acceptor, which were calculated to be 62% and 38%, respectively (refer to Paper III).  $A(\lambda)$ ,  $A_D(\lambda)$  and  $A_A(\lambda)$  are the simulated absorptance of the active layer, neat donor and neat acceptor films, respectively.

The absorbed photon fluxes of the donor ( $N_D$ ) and acceptor ( $N_A$ ) in the active layer were then estimated by integrating the individual absorptance over the AM 1.5G spectrum. It was revealed that there were nearly equal light harvesting contributions by PBDTTS-FTAZ and PNDI-T10 relative to the D:A composition, which can be easily understood by considering that the photon flux of the solar irradiance at the absorption region of PNDI-T10 is higher than that of PBDTTS-FTAZ. This disclosed that, in a D:A system with complementary absorption, the absorption contribution of the donor and acceptor was not only correlated to their  $\alpha$ , but also the absorption regions. Additionally, utilizing donor and acceptor polymers with complementary absorption does have a potential to achieve higher performance all-PSCs.

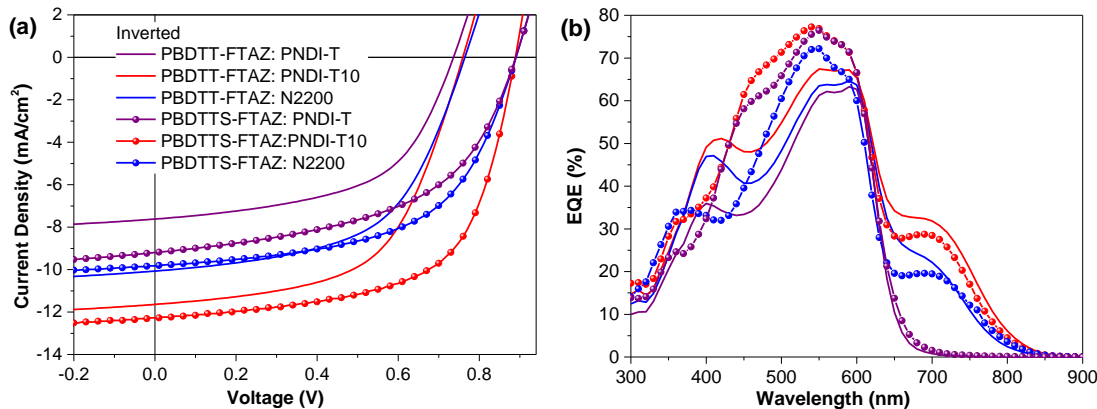
Figure 4.6 (a)  $J$ - $V$  characteristics of the inverted all-PSCs. (b) The corresponding EQE profiles.

Table 4.3 Photovoltaic parameters of the all-PSCs in inverted structure.

D:A	d (nm)	$V_{oc}$ (V)	$J_{sc}$ (mA/cm <sup>2</sup> )	FF	PCE (%)	SCLC $\mu_h$ (cm <sup>2</sup> V <sup>-1</sup> s <sup>-1</sup> )	SCLC $\mu_e$ (cm <sup>2</sup> V <sup>-1</sup> s <sup>-1</sup> )	$\mu_h/\mu_e$
PBDTT-FTAZ: PNDI-T	80	0.75	7.6 (7.5) <sup>a</sup>	0.55	3.1	$2.4 \times 10^{-5}$	$9.4 \times 10^{-6}$	2.6
PBDTT-FTAZ: PNDI-T10	96	0.77	11.6 (11.7)	0.57	5.0	$5.8 \times 10^{-5}$	$3.2 \times 10^{-5}$	1.8
PBDTT-FTAZ: N2200	90	0.77	10.1 (10.0)	0.56	4.3	$7.9 \times 10^{-5}$	$1.6 \times 10^{-5}$	4.9
PBDTTS-FTAZ: PNDI-T	86	0.89	9.0 (9.7)	0.55	4.4	$4.2 \times 10^{-5}$	$6.8 \times 10^{-6}$	6.2
PBDTTS-FTAZ: PNDI-T10	90	0.89	12.3 (12.2)	0.63	6.9	$7.8 \times 10^{-5}$	$2.7 \times 10^{-5}$	2.9
PBDTTS-FTAZ: N2200	92	0.89	9.8 (9.7)	0.57	5.0	$8.9 \times 10^{-5}$	$1.1 \times 10^{-5}$	8.1

<sup>a</sup>  $J_{ph}$  obtained by integrating the EQE with the AM1.5G spectrum

Both conventional and inverted device structures were employed to evaluate the all-PSCs. The optimized ratio of D:A polymers was 2:1 (w:w), and the active layers were processed from CB solutions. The parameters of the inverted all-PSCs are summarized in Table 4.3, and the corresponding  $J$ - $V$  curves and EQE spectra are depicted in Figure 4.6. The PBDTTS-FTAZ-based all-PSCs gave high  $V_{oc}$  values of ~0.90 V, *i.e.*, ~0.18 V higher than those of the PBDTT-FTAZ-based all-PSCs, which was attributed to the low-lying HOMO level of PBDTTS-FTAZ. This agrees well with the trend of  $V_{oc}$  variations in the PC<sub>71</sub>BM-based PSCs reported in a previous work.<sup>[109]</sup> Due to the comparable LUMO levels of three NDI-based acceptors, similar  $V_{oc}$  values were observed when the three acceptors were blended with the same donor. The PNDI-T10-based and N2200-based all-PSCs present higher  $J_{sc}$  compared to those based on PNDI-T, which indicates that more absorbed photons can be converted to photocurrent using D:A systems with complementary absorptions. The EQE spectra of the absorption-complementary D:A systems corroborate the photocurrent contributions both from the donors and acceptors (Figure 4.6 b).

Further, slightly higher  $J_{sc}$  and FF were obtained by PNDI-T10-based all-PSCs in comparison with N2200-based all-PSCs, which is in line with the phenomena discussed in 4.3.1.

Encouragingly, the PCEs of PBDTTS-FTAZ-based all-PSCs in the inverted structure showed long lifetimes retaining 90% of the initial PCEs after 60 days in the glove box. In addition, the inverted PBDTTS-FTAZ:PNDI-T10 all-PSCs could retain a high PCE of 6.0% after thermal annealing at 80 °C for 2 h. The results of stability studies highlight the promising future of all-PSCs, and the detailed discussion can be found in Paper III.

Charge carrier mobilities were measured via the SCLC method to understand the charge transport properties in the active layer. The  $\mu_h$  and  $\mu_e$  are summarized in Table 4.3. In general, all the blends studied in this work exhibited well-balanced hole and electron mobilities with  $\mu_h/\mu_e$  less than 10. As discussed in Section 4.3.1, balanced hole and electron mobilities can suppress bimolecular recombination, and bimolecular recombination loss may, therefore, not be a limiting factor for photovoltaic performance in this system. This is further supported by the quantified  $\eta_{BR}$  (~5%) (Paper III). To gain better insight into the recombination mechanism, geminate and total recombination losses were estimated from the  $J_{sc}$ ,  $J_{sat}$  and  $J_{tmax}$  of the PBDTTS-FTAZ:PNDI-T10 all-PSCs. The  $J_{tmax}$  was calculated to be 15.6 mA/cm<sup>2</sup>. The  $\eta_T$  and  $\eta_{GR}$  were calculated according to the equations (3.11) and (3.12), respectively. As shown in Table 4.4, the geminate recombination loss was not negligible and amounted to about 13%. The sum of bimolecular and geminate recombination losses (~18%) was in reasonable agreement with the total recombination loss of ~21%, so geminate recombination was dominant at short-circuit condition in this all-PSC.

Table 4.4 Summary of  $J_{sc}$ ,  $J_{sat}$  and  $J_{tmax}$  and the related recombination losses

all-PSC	$J_{sc}$ (mA/cm <sup>2</sup> )	$J_{sat}$ (mA/cm <sup>2</sup> )	$J_{tmax}$ (mA/cm <sup>2</sup> )	$\eta_{GR}$	$\eta_{BR}$	$\eta_T$
PTB7-Th:PNDI-T10	12.3	13.5	15.6	13%	5%	21%

In summary, the importance of light harvesting contributions by donors and acceptors with complementary absorption spectra was highlighted through a detailed comparison of all-PSCs using a selection of donor and acceptor polymers. As hypothesized, the PBDTTS-FTAZ:PNDI-T10-based all-PSC achieved highest PCE of 6.9%. The results revealed that the fine-tuned crystallinity of the acceptor, matched D:A system with complementary absorption and desired energy levels, and device architecture engineering can synergistically boost the performance of all-PSCs.

### 4.3.3 Energy Level Manipulation to Improve the $V_{oc}$

One of the key advantages of all-PSCs is that the LUMO levels of the acceptor polymers can be readily tuned to maximize  $V_{oc}$  values compared to PC<sub>71</sub>BM-based PSCs.

#### All-PSCs based on the donor polymer PTB7-Th

All-PSCs were fabricated from PTB7-Th as the donor, and N2200, F-N2200, PNDI-3T and PNDI-F45T10 as the acceptor polymers and their photovoltaic properties were investigated. The results presented herein are those extracted from Paper I, Paper VI and unpublished data. First, the  $V_{oc}$  variations of the all-PSCs containing NDI-based acceptor polymers were studied. As shown in Table 4.5, the  $V_{oc}$  could be slightly tuned via tuning the LUMO levels of the acceptor polymers by choosing different donor units within the acceptor polymers. However, the  $V_{oc}$  was limited to around 0.8 V due to the high-lying HOMO level of PTB7-Th. The relatively low  $J_{sc}$  and FF in PNDI-3T- and PNDI-F45T10-based all-PSCs were presumably due to the undesired blend morphology as discussed in Section 4.3.1. It is, therefore, essential to find rational combinations of donor and acceptor polymers, so that both the  $V_{oc}$  and other device parameters can be simultaneously improved.

Table 4.5 Photovoltaic parameters of the all-PSCs

A	d (nm)	$V_{oc}$ (V)	$J_{sc}$ (mA/cm <sup>2</sup> )	FF	PCE (%)
N2200 <sup>a</sup>	90	0.81	9.4(8.7) <sup>c</sup>	0.49	3.7
PNDI-3T <sup>a</sup>	90	0.83	9.9(9.7)	0.46	3.8
PNDI-F45T10 <sup>b</sup>	92	0.78	12.4(11.6)	0.54	5.2
F-N2200 <sup>b</sup>	90	0.72	12.9 (12.3)	0.58	5.4

<sup>a</sup>Conventional device structure. <sup>b</sup>Inverted device structure. <sup>c</sup>Photocurrents obtained by integrating the EQE with the AM1.5G spectrum are given in the parentheses

### All-PSCs based on the donor polymer PBDTS-TPD

Recently, Kim *et al.* reported a PNDI-T-based all-PSC with a high  $V_{oc}$  of 1.06 V and a PCE of 6.6%.<sup>[15]</sup> Inspired by their work, a combination of the donor polymer PBDTS-TPD with a low-lying HOMO level, and the acceptor polymer PNDI-T with a high-lying LUMO level were utilized as the active layer. The donor polymer PBDT-TPD was also utilized for comparison. The results discussed herein are from Paper V.

The all-PSCs were fabricated with conventional and inverted device structures. As both structures afforded similar performance, the device parameters with conventional structures are listed in Table 4.6 for discussion. The optimized D:A ratio of the all-PSCs was found to be 1.3:1 (w:w), and the donor and acceptor were dissolved in CF with 1% of DIO as additive. The detailed optimization of the performances of the all-PSCs can be found in Paper V. As shown in Table 4.6, both all-PSCs based on PBDT-TPD and PBDTS-TPD achieve high  $V_{oc}$  of 1.10 V. The PBDTS-TPD-based all-PSC attained a slightly higher PCE of 8.0%. Compared to the PBDT-TPD-based all-PSC, the slightly improved  $J_{sc}$  in the PBDTS-TPD-based all-PSC might have partially stemmed from the broader absorption spectrum and higher  $\alpha$  of PBDTS-TPD (Paper V). Additionally, the mobilities of both active layers were quite low (Table 4.6). The moderate FF around 0.6 might have partially been caused by the low mobilities of the active layer blends.<sup>[110]</sup>

Table 4.6 Photovoltaic parameters of the optimized all-PSCs in the conventional structure.

D	d (nm)	$V_{oc}$ (V)	$J_{sc}$ (mA/cm <sup>2</sup> )	FF	PCE (%)	SCLC $\mu_h$ (cm <sup>2</sup> V <sup>-1</sup> s <sup>-1</sup> )	SCLC $\mu_e$ (cm <sup>2</sup> V <sup>-1</sup> s <sup>-1</sup> )	$\mu_h/\mu_e$
PBDT-TPD	100	1.10	11.2 (10.8) <sup>a</sup>	0.59	7.3	$2.6 \times 10^{-5}$	$1.4 \times 10^{-5}$	1.9
PBDTS-TPD	100	1.10	11.6 (11.3)	0.63	8.0	$3.0 \times 10^{-5}$	$2.0 \times 10^{-5}$	1.5

<sup>a</sup>The photocurrent calculated by integrating the EQE spectra with AM 1.5G solar spectrum

In summary, a high-performance all-PSC with 8.0% PCE was achieved, which was mainly ascribed to the high  $V_{oc}$  of 1.10 V. The high  $V_{oc}$  benefited from the low-lying HOMO level of the donor and up-lying LUMO level of the acceptor, which is in congruence with our design motif. The second hypothesis described in Section 1.3, *i.e.*, “*By utilizing proper matched donor and acceptor polymers, the absorption spectra can be broadened or the open-circuit voltage can be modified, which can further improve the performance of the resulting all-PSCs in the optimal morphology condition.*” is proven to be valid. On the other hand, it is important to note that while modulating the energy level of donor and acceptor polymers, other important factors like absorption and blend morphology should also be considered to synergistically improve the performance of all-PSCs.

#### 4.3.4 Ternary Approach

Since the absorption of PTB7-Th:PNDI-T10 blend was very weak in the 400-600 nm, it was appropriate to use a ternary approach by introducing PBDTTS-FTAZ as a second donor into the PTB7-Th:PNDI-T10 blend to complement the absorption in the visible region. Thus, this ternary system was formed using PTB7-Th as the primary donor (D1), PBDTTS-FTAZ as the second donor (D2), and PNDI-T10 as the acceptor (A). The ratio of PTB7-Th:PNDI-T10 was fixed to be 1:1, where the contents of PBDTTS-FTAZ with respect to PTB7-Th were varied to optimize the D1:D2:A ratio. The results discussed in this section are based on Paper IV.

The absorption coefficients,  $\alpha$ , of the three neat polymer thin films are depicted in Figure 4.7 a. The polymer D2 presented strong absorption in the visible region with a high  $\alpha$  of  $11 \times 10^4$  cm<sup>-1</sup> at 600 nm, which was well complementary with the absorptions of polymers D1 and A. As shown in Figure 4.7 b, the LUMO levels of the three polymers provided a cascade alignment for electron transfer. The slightly up-shifted HOMO level of D1 indicated that the majority of holes generated in the active layer might finally be transported to the HOMO of D1 before extraction.

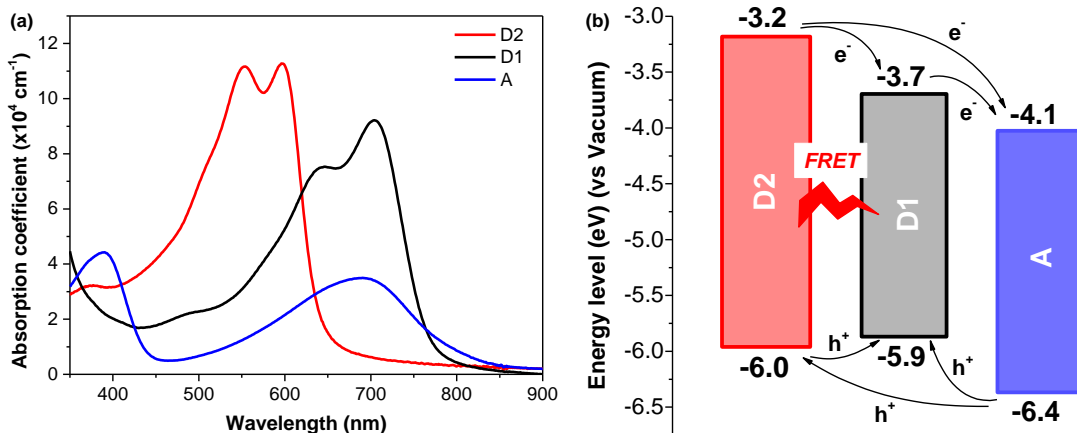


Figure 4.7 (a) Absorption coefficients of the polymer thin films. (b) Energy level diagram of the polymers. (Adapted from Paper IV)

The ternary all-PSCs were investigated with both conventional and inverted device structures. The variations of the device parameters as a function of the contents of D2 (relative to the amount of D1) are illustrated in Figure 4.8. Both the conventional and inverted devices presented the same trend, where the  $J_{sc}$ , FF and PCE gradually increased as the content of D2 increased from 0 to 15%, and declined while the content of D2 further increased from 15% to 30%. Thus, the 1:0.15:1 ternary all-PSC attained the maximal PCE of 9.0%, with  $V_{oc}$  of 0.84 V, with a clearly enhanced  $J_{sc}$  of  $14.5 \text{ mA cm}^{-2}$ , and FF of 0.74. Notably, the PCE was improved by 18% as compared to the D1:A binary all-PSC (9.0% vs 7.6%), which was mainly due to the 10% increase in  $J_{sc}$ . The nearly constant  $V_{oc}$  was pinned to that of the D1:A all-PSC, which was attributed to the mechanism that the majority of holes were transferred to the HOMO level of D1 before extraction. A preliminary stability study was conducted, and undesired fast decay in PCEs was observed for the devices stored at 20 °C in the glovebox.

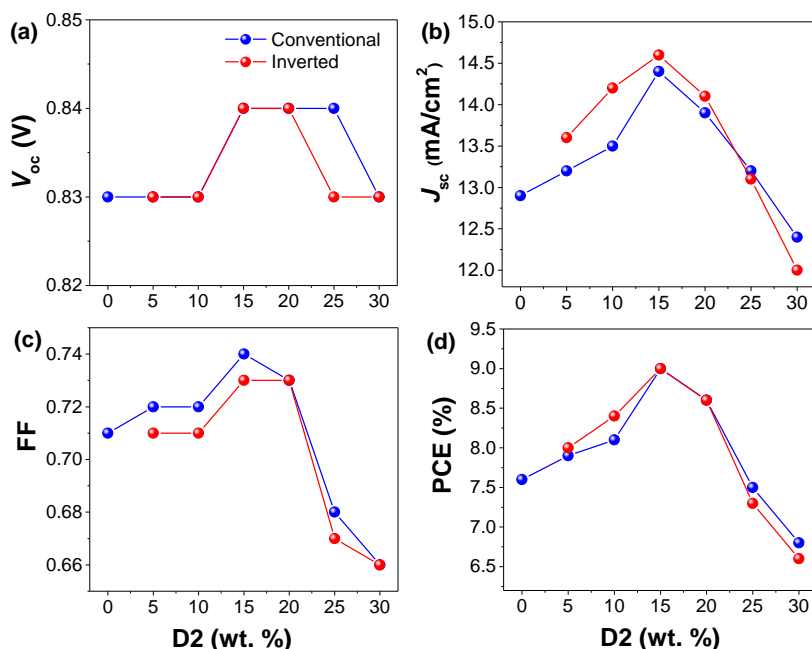


Figure 4.8 Variations in (a)  $V_{oc}$ , (b)  $J_{sc}$ , (c) FF, and (d) PCEs of the binary and ternary all-PSCs as a function of the contents of D2. (Adapted from Paper IV)

The exciton dissociation process in 1:0.15:1 ternary system was investigated by steady-state PL measurement. As shown in Figure 4.9 a, the D2:A and D1:A binary blends retained tiny PL peaks at 725 nm and 830 nm, respectively, whereas the PL of each polymer was completely quenched in the 1:0.15:1 ternary blend. This suggested that the inclusion of D2 promoted exciton dissociation in the ternary blend as compared to the binary blends. Moreover, Figure 4.9 b clearly revealed the Förster resonant energy transfer (FRET) from donor polymer D2 to donor polymer D1. While excited at 500 nm, the D2:D1 blend showed clearly higher PL intensity compared to the neat D1 film and the PL from D2 component disappeared in the blend. However, it is worth noting that energy and charge transfer processes are often intertwined and compete in the ternary blend, as reported in other ternary systems.<sup>[111]</sup> Additionally, the ternary blends retain similar charge mobilities to those of the D1:A binary blends (Paper IV). The relatively high (on the order of  $10^{-4} \text{ cm}^2 \text{V}^{-1} \text{s}^{-1}$ ) and well-balanced charge mobilities in the ternary system indicated that mobility was not a limiting factor in the ternary system.

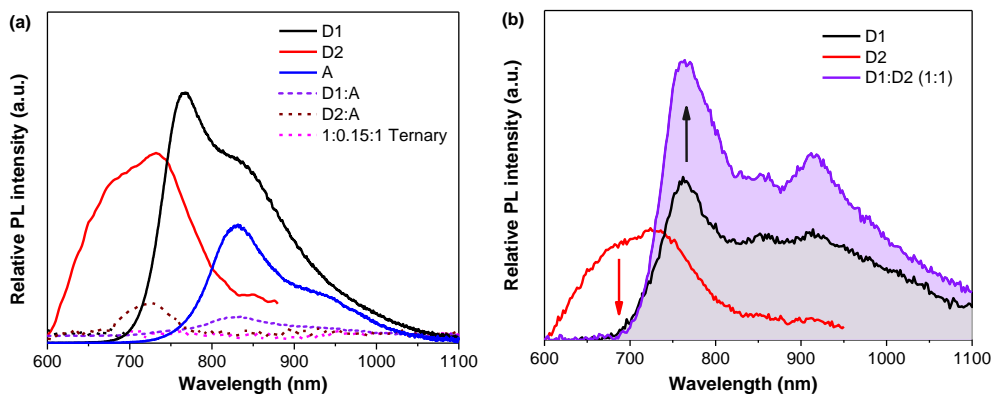


Figure 4.9 (a) Steady-state PL spectra of the neat polymers and ternary films excited at 500 nm. (b) PL spectra of neat donor polymer D2, neat donor polymer D1 film and D2:D1 blend film. (Adapted from Paper IV)

To estimate the recombination losses, we calculated the  $J_{\text{tmax}}$  of the conventional binary and ternary all-PSCs. With the optimized active layer thickness around 95 nm, the conventional D1:A all-PSC showed a  $J_{\text{tmax}}$  of  $16.5 \text{ mA/cm}^2$ , while a higher  $J_{\text{tmax}}$  of  $17.0 \text{ mA/cm}^2$  was recorded from the conventional D1:D2:A (1:0.15:1) ternary all-PSC, clearly suggesting the contribution of D2 to the enhanced  $J_{\text{ph}}$  of the ternary system. Furthermore, the  $J$ - $V$  curves of the 1:0.15:1 ternary all-PSCs showed slow saturation with a higher  $J_{\text{sat}}$  of  $15.1 \text{ mA/cm}^2$ , as compared to  $13.5 \text{ mA/cm}^2$  for D1:A binary all-PSC, when the bias voltage approached to  $-1.5 \text{ V}$ , (Paper I and Paper IV). In principle, the inverted bias voltage could sweep out all the free charges in the active layers to the electrodes. Thus, the  $\eta_{\text{GR}}$  in the conventional 1:0.15:1 all-PSC was calculated to be  $\approx 12\%$ . In contrast, the D1:A binary all-PSC featured a higher  $\eta_{\text{GR}}$  of  $\approx 19\%$ . This revealed that the optimized ternary all-PSC could suppress the geminate recombination. Moreover, as shown in Figure 4.10 a, the 1:0.15:1 ternary all-PSCs showed the lowest  $\eta_{\text{BR}}$  of only 1%–2%, implying that the bimolecular recombination in these all-PSCs was negligible. The recombination study revealed that the optimized ternary all-PSC could reduce the geminate and bimolecular recombination loss as compared to the D1:A binary all-PSC, which spontaneously suppressed the overall recombination losses.

As shown in Figure 4.10 b, both the absorptance and IQE profiles of the 1:0.15:1 ternary all-PSC were clearly higher than those of the D1:A binary all-PSC throughout the whole absorption wavelength of 450–750 nm. Clearly, the inclusion of small amounts of D2 indeed led to the enhanced  $J_{sc}$  in this ternary system. As discussed above, around 88% of the absorbed photons could be converted into free charges in the 1:0.15:1 ternary all-PSCs, which agreed well with the average IQE of  $\approx 85\%$  in the 1:0.15:1 ternary all-PSC.

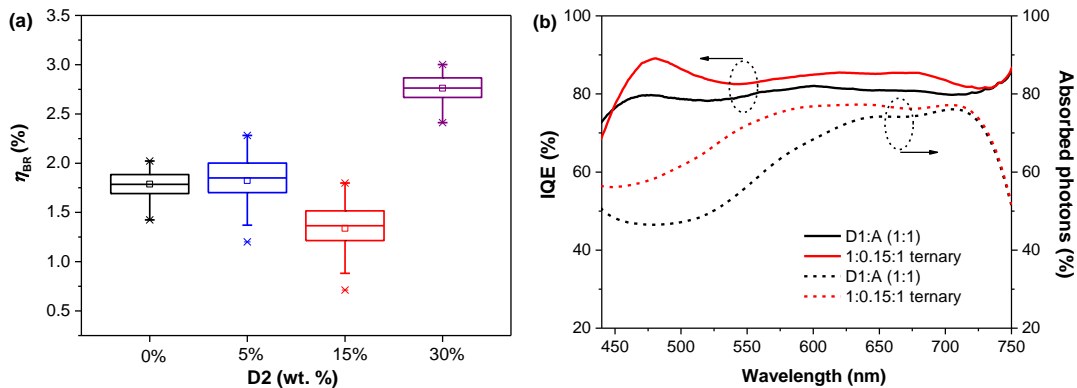


Figure 4.10 (a) Average  $\eta_{BR}$  values of conventional all-PSCs. (b) IQE curves of the D1:A binary and ternary all-PSCs. (Adapted from Paper IV)

In summary, through optimizing the weight loadings of polymer D2, the ternary all-PSCs attain outstanding PCEs of 9.0% in both the conventional and inverted devices, achieving one of the highest PCEs for ternary all-PSCs. The results provide constructive insights for developing high-performance ternary all-PSCs by choosing proper donor and acceptor polymers to overcome limitations in absorption, and by reducing recombination losses benefiting from good miscibility and efficient charge and energy transfer mechanisms. Thus, this study properly validated the third hypothesis described in Section 1.3, *i.e.*, “*Good miscibility with nano-scale phase separation can be achieved in ternary systems by choosing suitable donor and acceptor polymers, combined with proper device engineering. As such, ternary blends incorporating two donor polymers and one acceptor polymer with complementary absorption can overcome the absorption limit and boost the PCE of all-PSCs.*”

## 5 Synthesis and Characterization of Diketopyrrolopyrrole- and Isoindigo-based Acceptor Polymers for All-PSCs

---

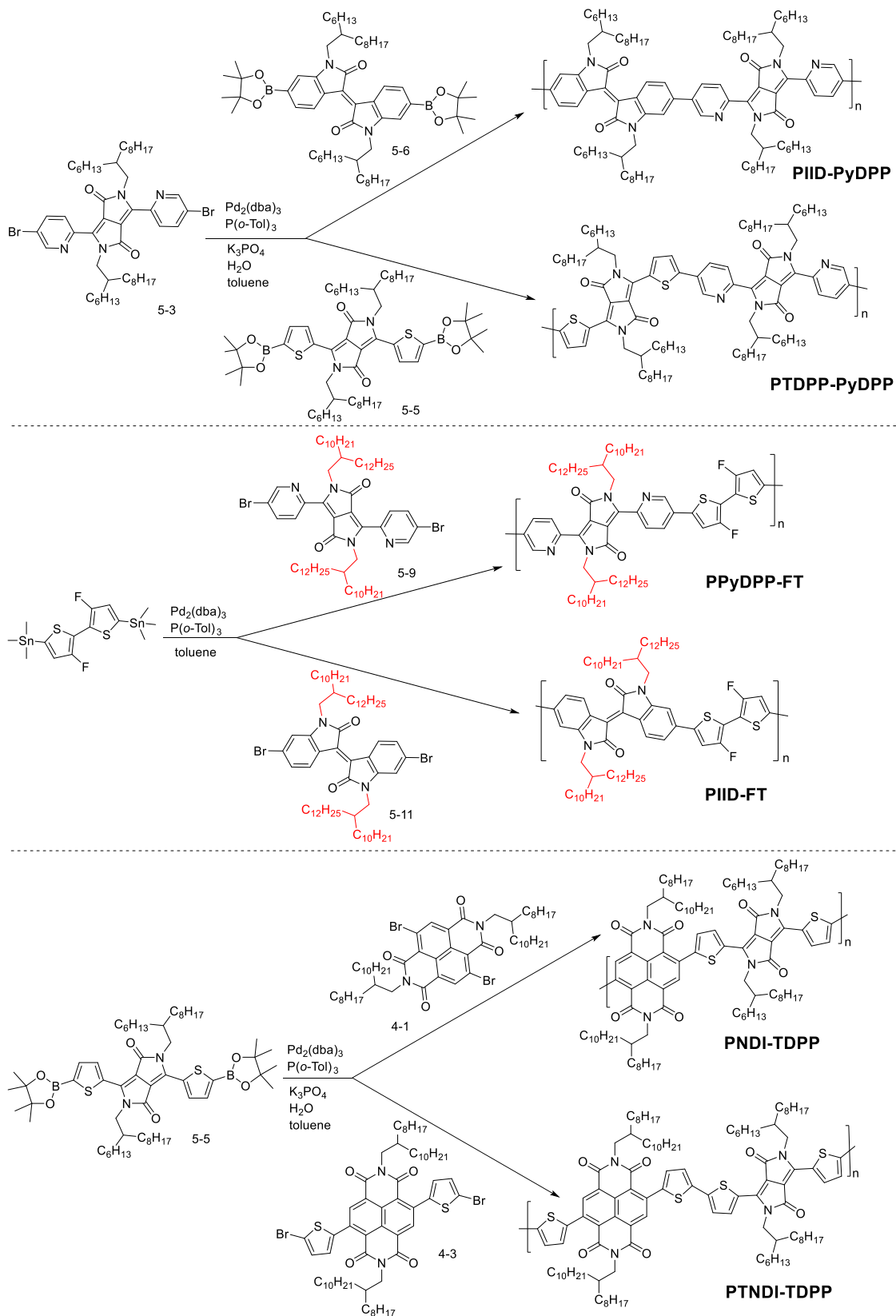
### 5.1 Background and Motivation

As discussed in Chapter 4, the NDI-based polymers showed relatively low  $\alpha$  and limited the  $J_{ph}$  of the all-PSCs. In addition, the normally quite low (*ca* -4.0 eV) LUMO levels of these acceptor polymers were similar to that of PC<sub>71</sub>BM and limited the  $V_{oc}$  of the all-PSCs. It was, therefore, essential to develop new acceptor polymers with high-lying LUMO levels and high  $\alpha$  to further boost the device performances of the all-PSCs. Among various promising electron-deficient units, the strong electron-withdrawing diketopyrrolopyrrole (DPP) and isoindigo (IID) units stand out because of their outstanding absorption properties and high mobility.<sup>[112]</sup> Although polymers containing DPP and IID have already been successfully utilized as donor materials in PSCs, there are, to date, very few successful examples of all-PSCs using DPP- or IID-based polymers as acceptors.<sup>[113]</sup>

In this chapter, a series of acceptor polymers based on DPP or IID are described. The acceptor polymer structures were correlated to the performances of all-PSCs by the studying their absorption properties, energy levels, charge transport, and their morphologies in particular.

### 5.2 Acceptor Polymers Synthesis and Characterization

The DPP- and IID-based acceptor polymers were synthesized by Stille and Suzuki coupling reactions as depicted in Scheme 5.1. Detailed synthetic routes can be found in Appendix I. Since a few early reports indicated that the pyridine-flanked diketopyrrolopyrrole (PyDPP) unit could lower HOMO levels and provide wider band gaps for the resulting polymers compared to the commonly used thiophene-flanked diketopyrrolopyrrole (TDPP) unit,<sup>[114]</sup> two new PyDPP-based polymers, PTDPP-PyDPP and PIID-PyDPP, were synthesized by incorporating the PyDPP unit with the TDPP and IID units, respectively. Moreover, two novel acceptor polymers, PPyDPP-FT and PIID-FT, were synthesized to differentiate the properties of PyDPP and IID unit. Elongation of the alkyl side chains was essential to increase the solubilities of the resulting polymers. The last two acceptor polymers, PNNDI-TDPP and PTNNDI-TDPP, were synthesized to enhance light harvesting in the NIR region.



Scheme 5.1 Synthetic routes towards DPP- and IID-based acceptor polymers. (Different side chains on DPP and IID units are marked in different colors to highlight the difference.)

The number-average molecular weights,  $M_n$ , and PDs of the acceptor polymers are listed in Table 5.1. The polymers PIID-PyDPP, PTDPP-PyDPP, PTDPP-NDI, and PTDPP-TNDI were readily soluble in common organic solvents, such as CF, CB and *o*DCB at room temperature. Whereas the polymers PPyDPP-FT and PIID-FT were only readily soluble in CB and *o*DCB at 70 °C due to their high molecular weights.

Table 5.1 Molecular weights and optical properties of acceptor polymers

Polymer	$M_n$ (kDa)	PD	$\lambda_{\max}^a$ (nm)	$E_g^{\text{opt}}$ (eV)
PIID-PyDPP	23.1	2.9	792	1.43
PTDPP-PyDPP	20.2	2.5	667	1.69
PPyDPP-FT	97.5	4.5	675	1.72
PIID-FT	53.8	2.7	704	1.66
PTDPP-NDI	45.4	3.73	755	1.38
PTDPP-TNDI	21.1	2.1	766	1.17

<sup>a</sup> The longest wavelength absorption maximum of the thin film.

The normalized absorption spectra of acceptor polymer thin films are illustrated in Figure 5.1. Polymers containing the TDPP unit displayed bathochromic shifts in comparison with the other polymers. Additionally, PTNDI-TDPP showed a broader absorption spectrum compared to PNDI-TDPP and the smallest  $E_g^{\text{opt}}$  of 1.17 eV among all the acceptor polymers. The absorption spectra of PPyDPP-FT and PIID-FT were quite similar, whereas the  $\lambda_{\max}$  was slightly redshifted from 675 nm for PPyDPP-FT to 704 nm for PIID-FT.

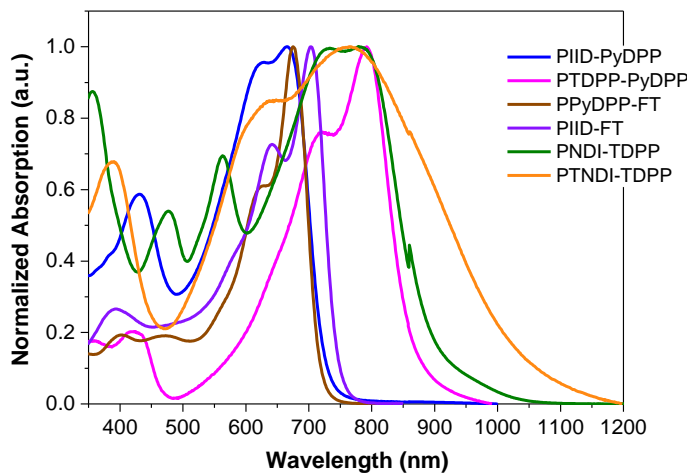


Figure 5.1 Normalized absorption spectra of the polymer thin films

### 5.3 Results and Discussion on All-PSCs

### 5.3.1 All-PSCs based on acceptor polymers PIID-PyDPP and PTDPP-PyDPP

As already discussed in Section 4.3.3, one of the key advantages of all-PSCs is that the LUMO levels of the acceptor polymers can be readily tuned to maximize the  $V_{oc}$  compared to PC<sub>71</sub>BM-based PSCs. In order to study the relationship between structure and all-PSC performance, two acceptor polymers, *viz.*, PTDPP-PyDPP and PIID-PyDPP were synthesized. This section will further emphasize the effect of energy levels on the performance of the resulting all-PSCs. To investigate the performances of the two acceptor polymers in all-PSCs, a medium band gap polymer PTB7-Th and a high band gap polymer PBDTTS-FTAZ were selected as donor polymers. The results discussed in this Section are based on Paper II.

The absorption coefficients,  $\alpha$ , and energy levels of the donors and acceptors are illustrated in Figure 5.2 a and b, respectively. The  $\alpha$  of N2200 and the energy levels of N2200 and PC<sub>71</sub>BM are also shown for comparison. Compared to N2200 and other NDI-based acceptor polymers reported in the literature, PIID-PyDPP showed a clearly higher  $\alpha$ .<sup>[95,103,115]</sup> Moreover, the LUMO levels of the two acceptor polymers were up-shifted compared to N2200 and PC<sub>71</sub>BM, thus a higher  $V_{oc}$  could be expected from the all-PSCs based on PIID-PyDPP and PTDPP-PyDPP. However, the HOMO level of PTDPP-PyDPP was very close to those of the two donor polymers, suggesting that there might have been insufficient driving force for charge separation in the PTB7-Th:PTDPP-PyDPP and PBDTTS-FTAZ:PTDPP-PyDPP blends, explaining the poor photovoltaic performance encountered (Paper II). Thus, only all-PSC performances based on the acceptor polymer PIID-PyDPP are discussed below.

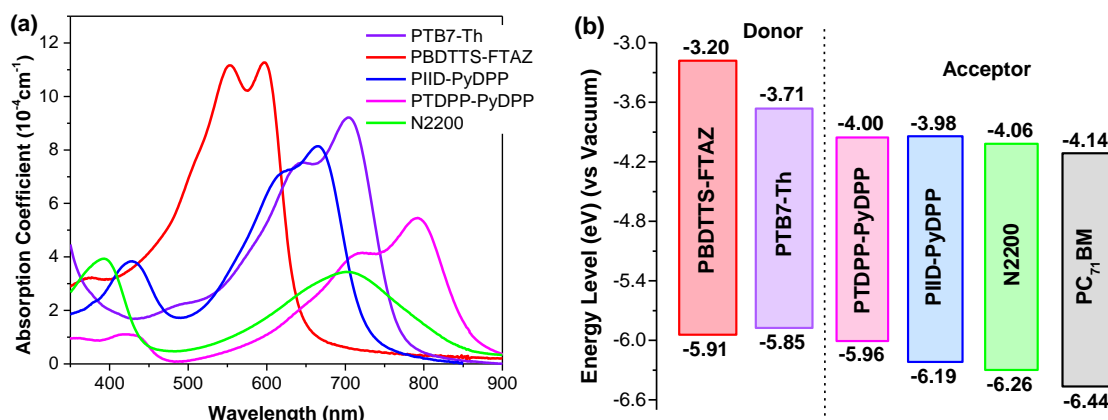


Figure 5.2 (a) Absorption coefficients of the polymers in thin films. (b) Energy level diagram of the polymers and PC<sub>71</sub>BM. (Adapted from Paper II)

The all-PSCs were investigated in the inverted structure as it was known to afford better performance compared to the conventional structure. The highest PCE for either donor was recorded with a donor-rich D:A ratio of 2.5:1 (w:w) and an optimized film thickness of 85 nm. The parameters of the optimized all-PSCs are summarized in Table 5.2. The PTB7-Th:PIID-PyDPP all-PSC showed a  $V_{oc}$  of 1.02 V, which was higher than the reported values for the PTB7-Th:PC<sub>71</sub>BM (~0.83 V) and PTB7-Th:N2200 (~0.82 V) PSCs.<sup>[103,116]</sup> This was consistent with the higher-lying LUMO level of PIID-PyDPP in comparison with PC<sub>71</sub>BM and N2200. The PBDTTS-FTAZ:PIID-PyDPP all-PSC attained a higher  $V_{oc}$  of 1.07 V, which presumably originated from the high-lying LUMO level of PIID-PyDPP and the low-

lying HOMO level of PBDTTS-FTAZ. Combined with a  $J_{sc}$  of 9.1 mA/cm<sup>2</sup> and a moderate FF of 0.43, an encouraging PCE of 4.2% was achieved, which is among the highest PCEs in all-PSCs fabricated with DPP-based polymers as acceptors. As shown in Figure 5.3 b, the photoresponse of the EQE curves were consistent with the absorption spectra of the blend films for both the PTB7-Th:PIID-PyDPP and PBDTTS-FTAZ:PIID-PyDPP all-PSCs, which corroborated the photocurrent contribution from both the donor and acceptor polymers. More encouragingly, more than 90% of initial PCE of the inverted PBDTTS-FTAZ:PIID-PyDPP all-PSCs could be retained after two weeks in the glove box.

Table 5.2 Photovoltaic parameters of the optimized PTB7-Th:PIID-PyDPP and PBDTTS-FTAZ:PIID-PyDPP all-PSCs

D:A	$V_{oc}$ (V)	$J_{sc}$ (mA/cm <sup>2</sup> )	FF	PCE (%)	SCLC $\mu_h$ (cm <sup>2</sup> V <sup>-1</sup> s <sup>-1</sup> )	SCLC $\mu_e$ (cm <sup>2</sup> V <sup>-1</sup> s <sup>-1</sup> )	$\mu_h/\mu_e$
PTB7-Th:PIID-PyDPP	1.02	5.9	0.39	2.3	$2.4 \times 10^{-4}$	$4.4 \times 10^{-5}$	5.5
PBDTTS-FTAZ: PIID-PyDPP	1.07	9.1	0.43	4.2	$7.1 \times 10^{-5}$	$3.7 \times 10^{-5}$	1.9

Since the  $\mu_h$  and  $\mu_e$  were fairly balanced in both blends (Table 5.2), the relatively low FF was surmised to be caused by non-ideal D:A morphology with the presence of large intermixed regions. In such case, the  $J_{ph}$  only slowly saturated under reverse bias as the enhanced electric field reduced the amount of charge being lost by nongeminate recombination (Figure 5.3 a). In addition, the  $\eta_{BR}$  was quantified according to equation (3.14) and the existence of bimolecular recombination was verified. On the other hand, the PTB7-Th-based all-PSC presented a much higher  $\eta_{BR}$  around 18% in comparison with that of the PBDTTS-FTAZ-based all-PSC (8%). This indicated that the bimolecular recombination was one of the main loss mechanisms in the PTB7-Th:PIID-PyDPP all-PSC, which resulted in the reduction of  $J_{sc}$ .

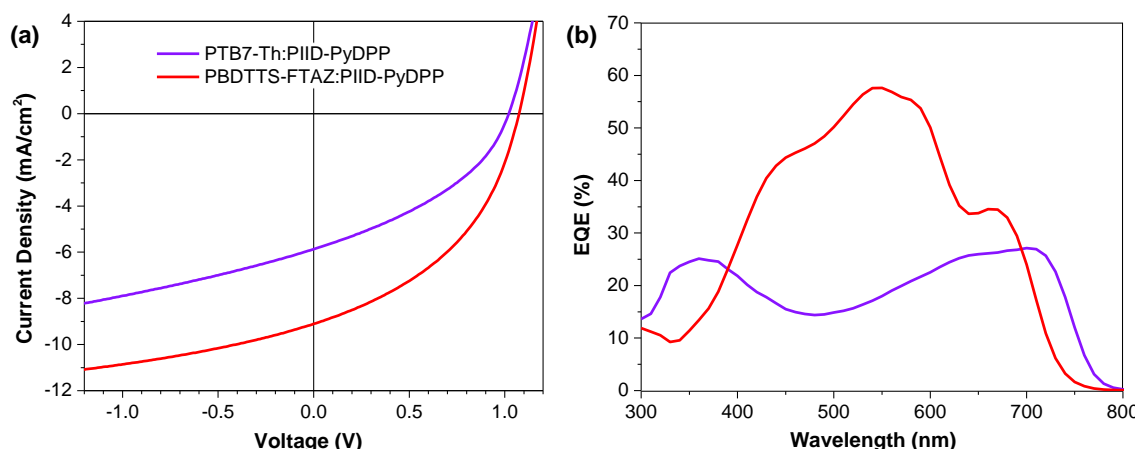


Figure 5.3 (a) J–V curves of the optimized PTB7-Th:PIID-PyDPP (2.5:1, w:w) and PBDTTS-FTAZ:PIID-PyDPP (2.5:1, w:w) all-PSCs. (b) The corresponding EQE profiles of the all-PSCs.

In summary, two novel acceptor polymers based on the PyDPP moiety, with up-shifted LUMO levels compared to PC<sub>71</sub>BM, were utilized with the intention of achieving higher  $V_{oc}$ . The acceptor polymer

PIID-PyDPP, with lower lying HOMO and enhanced  $\alpha$  compared to NDI-based polymers, is proved to be a promising acceptor polymer in combination with PBDTTS-FTAZ as donor. An encouraging PCE of 4.2%, featuring a high  $V_{oc}$  of 1.07 eV was obtained, which was among the best all-PSC performances with DPP-based polymers as acceptors.

This study demonstrated that the PyDPP unit can be a promising alternative to the widely used NDI unit for the synthesis of new acceptor polymers for high-performance all-PSCs. However, as the resulting PSCs suffered from the bimolecular recombination loss due to the suboptimal morphology and relatively low charge mobilities, further structural optimization is necessary. Therefore, the fourth hypothesis (Section 1.3) “*Other electron-deficient units which have been successfully utilized in donor polymers can be promising as building blocks for acceptors, featuring suitable LUMO levels and higher absorption coefficients in comparison with NDI-based polymers.*” is supported and the related research question “*Is there another promising acceptor building block other than NDI, which can further boost the performance of all-PSCs?*” is partly answered.

### 5.3.2 All-PSCs based on the acceptor polymers PPyDPP-FT and PIID-FT

Two acceptor polymers PPyDPP-FT and PIID-FT were utilized to further compare the properties of PyDPP- and IID-based polymers. However, as discussed in the previous Section, the resulting all-PSCs suffered from suboptimal morphology, which impacted the  $J_{sc}$  and FF particularly. Some preliminary results are discussed below.

In all-PSCs fabricated from the acceptor polymers PIID-FT and PPyDPP-FT, the high bandgap polymer PBDTT-FTAZ was utilized as the donor polymer due to its suitable LUMO and HOMO levels. The energy levels of donor and acceptor polymers and PC<sub>71</sub>BM are shown in Figure 5.4. The LUMO levels of the two acceptor polymers were up-shifted compared PC<sub>71</sub>BM, thus a higher  $V_{oc}$  could be expected.

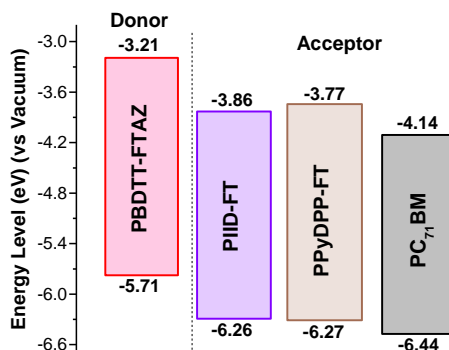


Figure 5.4 Energy level diagram of the polymers and PC<sub>71</sub>BM.

The PIID-FT- and PPyDPP-FT-based all-PSCs were preliminarily evaluated in the inverted structure following the same procedure as for the acceptor polymer PIID-PyDPP. The D:A ratio was 2.5:1 (w:w) and the photovoltaic parameters under the optimal film thickness of 85 nm are summarized in Table 5.3. The higher  $V_{oc}$  obtained in PPyDPP-FT-based all-PSC compared to that of PIID-FT-based device was consistent with its higher LUMO level. However, poor FFs were observed in both devices, which was similar to the PPyDPP-IID-based all-PSCs discussed in the previous Section. Consequently, the

inferior performance was assumed to be caused by the suboptimal blend morphology. To verify this, atomic force microscope (AFM) measurements were conducted. As shown in Figure 5.5, clear polymer aggregation was observed in both blend films, which supported the assumption. Since the donor polymer PBDTT-FTAZ did not show clear aggregation behavior in our previous study (Paper III), this phenomenon could be attributed to the high regioregularities of the acceptor polymers.

Table 5.3 Preliminary photovoltaic parameters of PPyDPP-FT- and PIID-FT-based all-PSCs

A	$V_{oc}$ (V)	$J_{sc}$ (mA/cm <sup>2</sup> )	FF	PCE (%)
PPyDPP-FT	1.08	8.35	0.4	3.6
PIID-FT	0.99	2.42	0.45	1.1

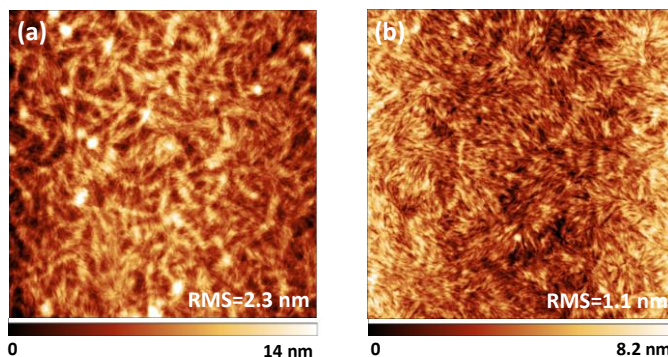
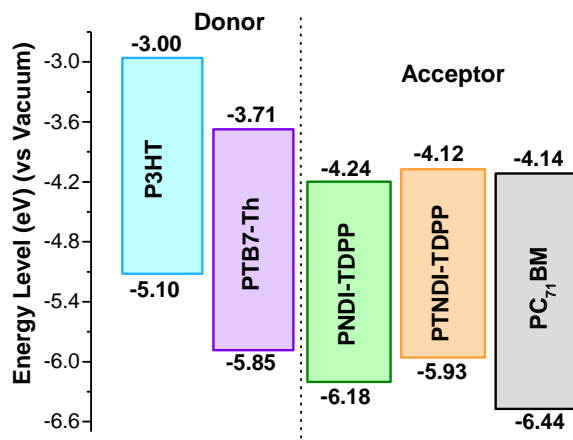


Figure 5.5 AFM topography ( $5 \times 5 \mu\text{m}^2$ ) images of the blend films.

In summary, the effect of morphology on the performance of all-PSCs using PPyDPP-FT and PIID-FT as acceptor polymers was studied. The inferior performance of all-PSCs investigated here was suggested to be mainly due to the aggregation of the acceptor polymer. Further optimization of device processing parameters is necessary to improve the morphology. In addition, modifying the backbone of the acceptor polymers to increase flexibility may result in reduced aggregation and improved morphology.

### 5.3.3 All-PSCs based on the acceptor polymers PNDI-DPP and PTNDI-TDPP

Two novel acceptor polymers PNDI-TDPP and PTNDI-TDPP were utilized to harvest light in the NIR region. As shown in Figure 5.6, the acceptor PNDI-TDPP featured quite low LUMO level and the acceptor PTNDI-TDPP featured similar LUMO level compared to PC<sub>71</sub>BM. To investigate the all-PSC performance of the two acceptor polymers in all-PSCs, a high bandgap polymer P3HT and a medium bandgap polymer PTB7-Th were utilized as donors.

Figure 5.6 Energy level diagram of the polymers and PC<sub>71</sub>BM.

Preliminary evaluation of the all-PSC performance was conducted following the same procedure discussed in Chapter 4 for acceptor polymer PNDI-T10. The D:A ratio was fixed at 1:1 (w:w) and the performance was optimized by varying the active layer film thickness. The photovoltaic parameters with the optimal blend film thickness of around 80 nm are summarized in Table 5.4. The  $V_{oc}$ s of PTNDI-TDPP-based all-PSCs were around 0.06 V higher compared to that of PNDI-TDPP, with respect to both donor polymers. This is consistent with the LUMO level difference between the two acceptor polymers. On the other hand, the relatively low  $V_{oc}$  suggests that there is a large energy loss in the system. All devices presented poor  $J_{sc}$  and FF, which could be attributed to suboptimal morphology (Figure 5.7). Notwithstanding, more detailed studies on the charge generation and transport are required to support these assumptions.

Table 5.4 Preliminary photovoltaic parameters of the all-PSCs in the conventional structure.

D:A	$V_{oc}$ (V)	$J_{sc}$ (mA/cm <sup>2</sup> )	FF	PCE (%)
PTB7-Th:PNDI-TDPP	0.65	1.5	0.37	0.37
PTB7-Th:PTNDI-TDPP	0.71	1.8	0.36	0.46
P3HT:PNDI-TDPP	0.31	0.18	0.48	0.03
P3HT:PTNDI-TDPP	0.38	0.2	0.46	0.04

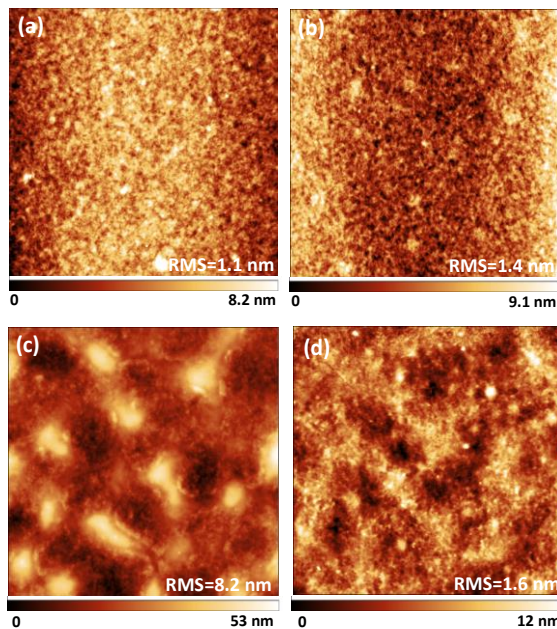


Figure 5.7 AFM topography ( $5 \times 5 \mu\text{m}^2$ ) images of the blend films.

In summary, the effect of morphology on the performances of all-PSCs using PNDI-TDPP- and PTNDI-TDPP-based acceptor polymers were studied. The inferior performances of the all-PSCs is presumably mainly due to the suboptimal morphology, and further studies to address the issues are necessary.



## 6 Synthesis and Characterization of Thiadiazoloquinoxaline-based Acceptor Polymers for All-PSCs and All-PPDs

---

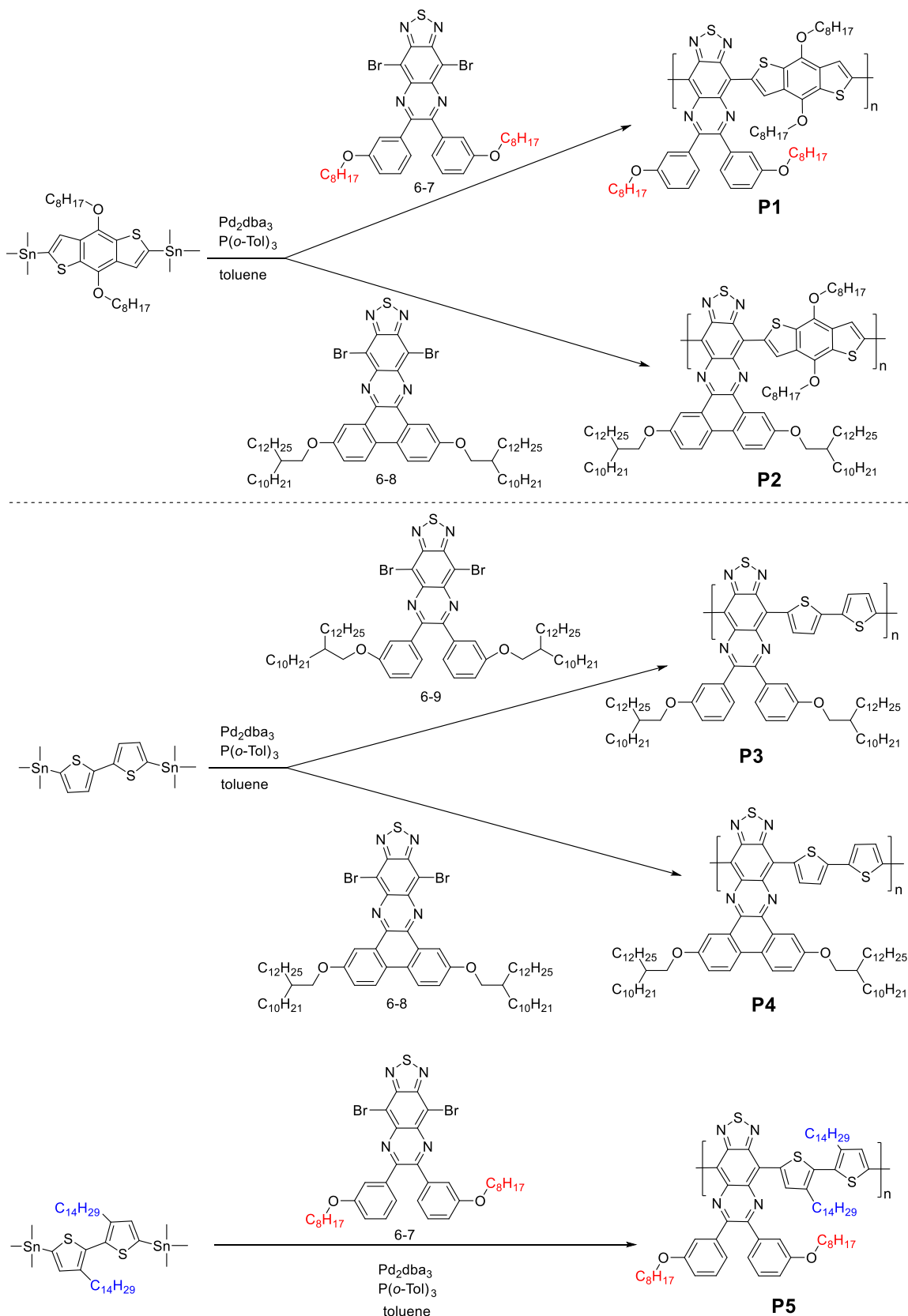
### 6.1 Background and Motivation

Besides NDI and DPP units, the thiadiazoloquinoxaline (TDQ) unit also possesses an outstanding electron-accepting ability due to the presence of electron-deficient thiadiazole and pyrazine rings.<sup>[27a,117]</sup> It has become one of the most important building blocks for the construction of donor polymers for NIR light harvesting and TDQ-based polymers with very low energy bandgap,  $E_g$ , have been developed since the pioneering work by Yamashita *et al.*<sup>[27a,118]</sup> The excellent absorption properties in the NIR region and the encouraging ambipolar mobilities also make it a promising building block for acceptor polymers in all-PSCs and all-PPDs application.<sup>[117,119]</sup>

Thus, a series of acceptor polymers based on TDQ units were synthesized and preliminary studies were made to investigate their performances in all-PSCs. The results discussed in this chapter are new and have not yet been published.

### 6.2 Acceptor Polymers Synthesis and Characterization

All TDQ-based polymers were synthesized via Stille coupling polymerization and the synthetic routes are shown in Scheme 6.1. Synthetic routes for the preparation of the monomers can be found in Appendix II. Two popular donor units BDT and bithiophene were incorporated with the TDQ unit separately. To compare the properties of the polymers with different side chain positions, bithiophene with long side chains were also utilized as a donor unit. The lengths of the side chains on either the TDQ unit or the bithiophene unit were modified to ensure better solubilities of the resulting polymers. Moreover, higher planarity and stronger conjugation was expected in polymers P2 and P4 (Scheme 6.1), due to the fusion of the phenanthrene moiety with the TDQ scaffold.



Scheme 6.1 Synthetic routes towards TDQ-based acceptor polymers. (Different side chains are marked in different colors to highlight the difference.)

The molecular weights and optical properties of the TDQ-based polymers are shown in Table 6.1. The particularly low  $M_n$  of polymer P4 was presumably due to the lack of solubility. All polymers, except polymer P4, were readily soluble in common solvents like CF, CB and *o*DCB. Polymer P4 was soluble in CB and *o*DCB at 70 °C.

Table 6.1 Molecular weights and optical properties of TDQ-based acceptor polymers

Polymer	$M_n$ (kDa)	PD	$\lambda_{\max}^{\text{a}}$ (nm)	$E_g^{\text{opt}}$ (eV)
P1	19.7	1.3	1147	0.95
P2	33.9	2.2	1069	1.01
P3	23.4	1.8	1369	0.69
P4	6.7	1.5	1411	0.69
P5	31.1	1.7	846	1.20

<sup>a</sup> The absorption maximum of the thin film.

The absorption profiles of all polymers featured two main absorption bands (Figure 6.1 a). The first band at shorter wavelength (400-600 nm) is attributed to the  $\pi-\pi^*$  transition of the main chain, while the second at longer wavelength (700-1800 nm) is due to the ICT interaction between the donor and acceptor moieties in the polymer backbone.<sup>[118b]</sup> Owing to the long side chains on the thiophene units, the strong steric repulsion between the donor and acceptor moieties in polymer P5, and to some extent in polymers P1 and P2, explains the decrease in the ICT interaction and, thus, the much smaller  $\lambda_{\max}$  values compared to polymers P3 and P4. The fusion of the phenanthrene moiety with the TDQ core should effectively extend  $\pi$ -conjugation and cause a red-shifted absorption.<sup>[120]</sup> This is in agreement with the absorption spectrum of polymer P4 compared to that of P3. However, the opposite was observed in polymers P1 and P2, where the fusion of the phenanthrene unit led to a larger torsional strain between the TDQ and BDT units, due to the long alkyl chains on the benzene rings.

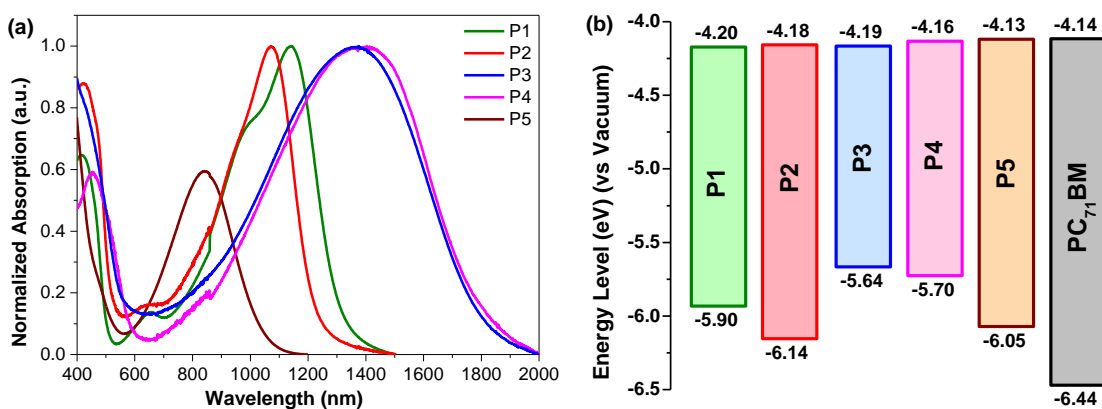


Figure 6.1 (a) Normalized absorption spectra of the TDQ-based polymer thin films. (b) Energy level diagram of the polymers and PC<sub>71</sub>BM.

The energy levels of all TDQ-based polymers are depicted in Figure 6.1 b, and the energy level of PC<sub>71</sub>BM is also shown for comparison. All polymers presented similar LUMO levels at around -4.16 eV, which stemmed from the dominant contribution of the electron-withdrawing TDQ units. Polymer P5 showed much larger  $E_g$  compared to polymers P3 and P4, due to the large steric hindrance as explained above. The energy levels correlated well with their absorption profiles. Moreover, as explained above for the absorption, the  $E_g$  dropped while changing the donor moiety from BDT to bithiophene.

### 6.3 Preliminary Evaluation in All-PSCs

Since all acceptor polymers present quite high-lying HOMO levels, there are few suitable donor polymers in terms of matching energy levels. Therefore, to investigate the performances of the acceptor polymers in all-PSCs, the well-known high bandgap polymer P3HT, with a high-lying HOMO level, was utilized as the donor polymer.<sup>[5]</sup>

Polymers P1 and P5 with relatively low-lying HOMO levels were chosen as representative acceptors to be preliminarily evaluated in the conventional all-PSC device structure. The photovoltaic parameters of P3HT:P1 and P3HT:P5 all-PSCs are summarized in Table 6.2. Both the  $V_{oc}$  and  $J_{sc}$  values for P1- and P5-based all-PSCs were very low, resulting in low PCEs. The low PCEs can be explained by the absorption behaviors of the acceptor polymers and the blend morphologies. Even though both acceptor polymers P1 and P5 presented strong absorption bands in the NIR region, the exciton generated by harvesting low energy photons could not be effectively dissociated into free charges.<sup>[121]</sup> This is explained by the energy gap law, which states that the non-radiative decay rate increases exponentially as the energy gap decreases.<sup>[122]</sup> In addition, as shown in Figure 6.2, the strong polymer aggregation and large phase separation further sabotaged the exciton dissociation process and resulted in inferior  $J_{sc}$  and PCE. Therefore, further optimization in both device processing parameters and acceptor polymer structures are required to optimize the blend morphologies.

Table 6.2 Preliminary photovoltaic parameters of the all-PSCs in the conventional structure.

D:A (w:w)	$V_{oc}$ (V)	$J_{sc}$ (mA/cm <sup>2</sup> )	FF	PCE (%)
P3HT:P1 (1:1)	0.41	0.3	46	0.06
P3HT:P5 (1:1)	0.63	0.4	58	0.15

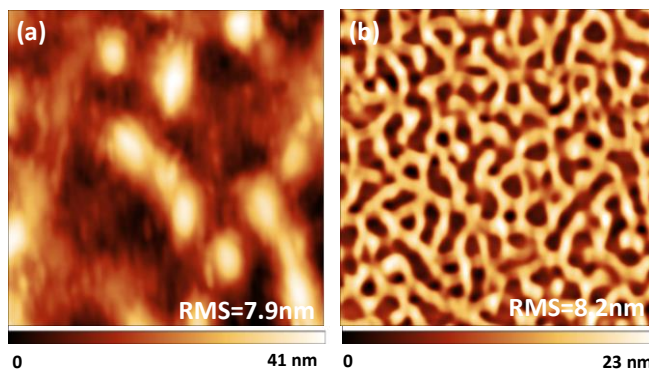


Figure 6.2 AFM topography ( $5 \times 5 \mu\text{m}^2$ ) images of the blend films.

In summary, a series of TDQ-based acceptor polymers were synthesized and investigated to elucidate the structure-property relationship. The acceptor polymers showed strong absorption in the NIR region and can be promising candidates in all-PSC and all-PPD applications. However, preliminary all-PSC studies using P3HT as the donor polymer showed poor PCE and suboptimal morphologies with large phase separation. Investigation into further structural modifications of these polymers, and additional device engineering is required for increased performance in the all-PSCs. Moreover, other donor polymers featuring high-lying LUMO levels and proper crystallinity should be considered to modify the morphology.



## 7 Characterization of Naphthalene Diimide-based Acceptor Polymers for All-PPDs

---

---

### 7.1 Background and Motivation

The performances of all-PPDs still lag largely behind fullerene-based PPDs and there are only a few reports on all-PPDs with decent responsivity ( $R$ ) and low dark current density ( $J_d$ ) simultaneously while operating at reverse bias.<sup>[50b]</sup> Moreover, Table 3.2 clearly shows that the main limitation in the performance of all-PPDs is the poor  $R$  (only about 0.12 A/W). Since the combination of PTB7-Th:PNDI-T10 and PTB7-Th:PNDI-FT10 afforded efficient all-PSCs in our previous study, as discussed in Section 4.3.1, it was interesting to further explore their potential application in all-PPDs. Thus, the PTB7-Th:PNDI-T10 and PTB7-Th:PNDI-FT10 all-PPDs were fabricated and their properties were studies in comparison with those of PTB7-Th:PC<sub>71</sub>BM all-PPD. The results discussed in this Section are based on Paper VII.

### 7.2 Reduction of Dark Current

Since electron injection takes place from the anode to the LUMO of the acceptor material operating at inverted bias voltage in the dark (Figure 3.2 b), less content of acceptors may facilitate reducing the dark current in the case that the formation of acceptor-rich domain in the active layer is adjacent to the anode of the device.<sup>[123]</sup> Therefore, the PTB7-Th:PNDI-FT10 all-PPD was taken as an example to evaluate the dependence of dark current on the D:A ratio.

All-PPDs were investigated in the inverted structure and 3% DIO was used as additive. The detailed device optimization can be found in Paper VII. To make sure PPD devices sustained reverse bias voltage, all measurements were conducted under reverse biases up to -5 V. The all-PPD performance parameters are illustrated in Figure 7.1. Clearly, the  $J_d$  under -5 V bias decreased dramatically from  $3.73 \times 10^{-4}$  to  $4.86 \times 10^{-5}$  mA/cm<sup>2</sup> while the content of PNDI-FT10 in the active layer decreased from 50% to 20% (D:A ratio from 1:1 to 4:1). Then the  $J_d$  continued to slightly decrease to  $4.07 \times 10^{-5}$  mA/cm<sup>2</sup> while the content of PNDI-FT10 dropped to 11% (D:A ratio 8.5:1). It was also demonstrated that lowering acceptor content in the active layers was a facile way to reduce  $J_d$ . The EQE<sub>max</sub> and  $R_{max}$  could be kept steady at above 67% and 0.37 A/W, respectively, while the content of PNDI-FT10 was varied from 50% to 13%. Thus the highest  $D^*_{max}$  of  $3.2 \times 10^{12}$  Jones was achieved at D:A ratio of 6.5:1 under the combined effect of  $J_d$  and  $R$ .

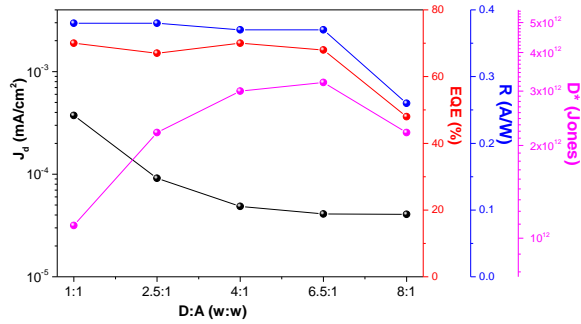


Figure 7.1 Variations in  $J_d$ ,  $EQE_{\max}$ ,  $R_{\max}$  and  $D^*_{\max}$  operating at -5 V bias of PTB7-Th:PNDI-FT10 all-PPDs as a function of D:A (w:w) ratio. (Reproduced from Paper VII)

### 7.3 Comparison Between All-Polymer- and Fullerene-based Photodetectors

To evaluate the effects of different acceptor materials on the performances of PPDs, PTB7-Th was utilized as the donor polymer for all devices, in combination with either PC<sub>71</sub>BM, PNDI-T10 or PNDI-FT10 as acceptor. The D:A (w:w) ratio for all devices was fixed at 4:1 and all the materials were dissolved in CB with 3% DIO as additive.

The optimal characteristic parameters are summarized in Table 7.1. The corresponding spectra and detailed device optimization can be found in Paper VII. Limited by the solubility of PC<sub>71</sub>BM, the film thickness of PTB7-Th:PC<sub>71</sub>BM blends could not be increased further than 360 nm while sustaining a homogenous film. The PC<sub>71</sub>BM-based PPD showed the lowest  $J_d$  of  $3.67 \times 10^{-5}$  mA/cm<sup>2</sup> under -5 V bias. In comparison, PNDI-FT10- and PNDI-T10-based all-PPDs exhibited slightly higher  $J_d$  values of  $4.86 \times 10^{-5}$  mA/cm<sup>2</sup> and  $4.09 \times 10^{-5}$  mA/cm<sup>2</sup>, respectively. While the  $J_d$ s of all studied PPDs were in the order of  $10^{-5}$  mA/cm<sup>2</sup>, all-PPDs based on PTB7-Th:PNDI-FT10 blend exhibited the highest  $R$  of 0.37 A/W among all devices. Thus, all devices showed similar  $D^*$  in the order of  $10^{12}$  Jones. The higher  $J_d$  values in the all-PPDs can be explained by the percolation of electrons via the larger PNDI-FT10 and PNDI-T10 crystallites present. This was supported by coarser surfaces, as observed in AFM measurements, due to the larger polymer aggregates (Paper VII).

Table 7.1 Characteristics of PPDs based on PTB7-Th:PNDI-FT10 (4:1, w:w), PTB7-Th:PNDI-T10 (4:1, w:w) and PTB7-Th:PC<sub>71</sub>BM (4:1, w:w) operating at bias -5 V

Acceptor	d (nm)	$J_d$ (mA/cm <sup>2</sup> )	$J_{ph}$ (mA/cm <sup>2</sup> )	${}^a J_{ph}^{EQE}$ (mA/cm <sup>2</sup> )	$R_{\max}$ (A/W)	$D^* @ 730 \text{ nm}$ (Jones)	${}^b J_{\text{simulated}}$ (mA/cm <sup>2</sup> )
PNDI-FT10	440	$4.86 \times 10^{-5}$	16.53	16.74	0.37	$3.0 \times 10^{12}$	22.83
PNDI-T10	240	$4.09 \times 10^{-5}$	12.17	12.24	0.30	$2.6 \times 10^{12}$	22.00
PC <sub>71</sub> BM	320	$3.67 \times 10^{-5}$	12.01	12.12	0.31	$3.4 \times 10^{12}$	22.24

<sup>a</sup> Photocurrent density calculated by integrating the EQE spectra

<sup>b</sup> Calculated  $J_{ph}$  from simulated absorptance of the active layer at the corresponding film thickness

The ideality factor under illumination,  $n_i$ , was calculated to illustrate the origin of the  $J_d$  and gain insight into the recombination mechanism in PPDs. As shown in Figure 7.2, the PTB7-Th:PC<sub>71</sub>BM PPD

showed the minimal  $n_i$  of 1.11, while the  $n_i$  of PTB7-Th:PNDI-T10 and PTB7-Th:PNDI-FT10 all-PPDs were around 1.19 and 1.25, respectively. The higher  $n_i$  manifested that there were more trap assisted recombinations in the all-PPD system. It also indicated that the traps could be intrinsically contained in the acceptor polymers, leading to lowered  $V_{oc}$  and  $J_d$  in the all-PPDs compared to PC<sub>71</sub>BM-based PPD.

Furthermore, no significant change of  $J_{ph}$  under reverse bias voltage was observed over 20 days in the glove box. Despite the fact that highly-stable PPDs were reported with different active layers,<sup>[19c,124]</sup> the  $J_d$  in this work was observed to be less stable than  $J_{ph}$  as a function of shelf time (Paper VII). Encouragingly, the  $J_d$  under high reverse bias voltage tended to be more stable in all-PPDs compared to PC<sub>71</sub>BM-based PPDs, which could be ascribed to the formation of large PC<sub>71</sub>BM aggregates in the active layer over time.<sup>[125]</sup>

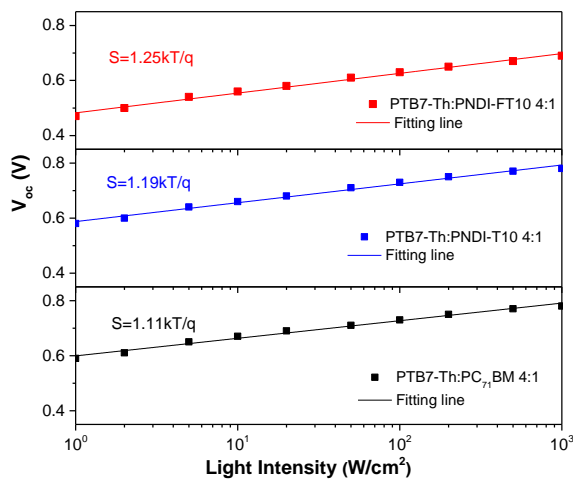


Figure 7.2 Measured  $V_{oc}$  of PPDs as a function of  $I$  (squares). The solid lines represent the best fits to the data for a logarithmic dependence of  $V_{oc}$  on  $I$  with a slope of  $S$ . (Reproduced from Paper VII)

Transient photocurrent (TPC) measurements were conducted to provide better analysis of the charge extraction properties in the PPDs.<sup>[126]</sup> As shown in Figure 7.3, the extracted photocurrents from PTB7-Th:PNDI-FT10 all-PPDs were much higher than those extracted from the other two devices, which were consistent with the higher  $J_{ph}$  observed in PTB7-Th:PNDI-FT10 all-PPDs. On the other hand, the all-PPDs exhibited longer decay times and higher persistent photocurrent tails after an initial fast decay, compared to the PC<sub>71</sub>BM-based PPDs, which were attributed to increased trap-assisted recombination or lowered conductivity.<sup>[127]</sup> Since the differences between the dielectric constants of the polymers ( $\epsilon_r$ ) in all blends were too small to exert measurable influences on the PPD performances (Paper VII), the longer decay times observed for all-PPDs were explained by the slower detrapping process after turn-off, which correlated well with the predictions from  $V_{oc}$ - $I$  measurements.

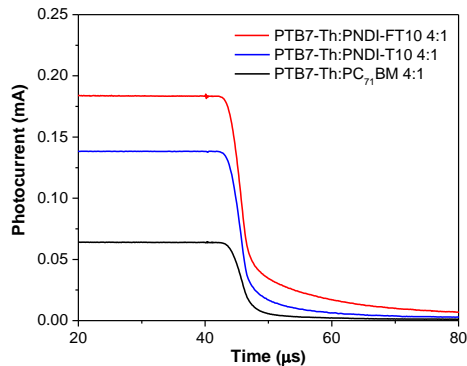


Figure 7.3 Transient photocurrent decay of PPDs. (Reproduced from Paper VII)

In summary, the representative acceptor polymers, PNDI-T10 and PNDI-FT10, which produced high-performance all-PSCs were utilized in all-PPDs and the effects of different acceptor structures on the device performances were systematically characterized. A high-performance all-PPD exhibiting  $J_d$  of  $4.09 \times 10^{-5}$  mA/cm<sup>2</sup>,  $R_{max}$  of 0.37 A/W, and  $D^*$  of  $3.2 \times 10^{12}$  Jones operating at a reverse bias of -5 V was demonstrated, which was among the best all-PPD performances reported to date and comparable with fullerene-based PPDs. As such, the fifth hypothesis (Section 1.3) that “*Decreasing the content of acceptor polymer can be an effective way to reduce the dark current under the desired morphology condition without sacrificing the photoresponsivity.*” is supported. The final research question “*Is it possible to reduce the dark current of all-PPDs using NDI-based acceptor polymers while maintaining the high EQE achieved in all-PSCs?*” is answered.

Furthermore, the trap-assisted recombination due to acceptor polymer aggregate was disclosed to be the main origin of higher  $J_d$  in all-PPDs compared to fullerene-based PPDs, which is also instructive to PSCs application since the same active layer materials are used.

## 8 Summary and Outlook

---

---

The past four years have witnessed rapid progress in all-PSCs and all-PPDs, boosted by novel methods of synthesizing donor and acceptor polymers, and device engineering. However, there are still three main primary challenges hindering their commercial application.

First, the overall performance of all-PSCs and all-PPDs are still lower than any of their commercially available inorganic competitors. The thesis first focused on approaches towards improving the performances of all-PSCs using NDI-based acceptor polymers, specifically by modifying the molecular structures of acceptor polymers, and rationally choosing a suitable donor and acceptor combination.

Compared to the rigid acceptor polymers N2200 and F-N2200, the random copolymers PNDI-T10 and PNDI-FT10 with 10% thiophene, T, units in the polymer backbone, afford better counterparts for the PTB7-Th donor and formed the desired nanoscale blend morphology with reduced bimolecular recombination, which led to high PCEs over 7%. The introduction of disorder on the acceptor polymer backbones turned out to be a facile method to potentially benefit the photovoltaic performance. As such, the first hypothesis (Section 1.3) regarding crystallinity control was verified.

The second hypothesis (Section 1.3) on utilizing properly matched donor and acceptor polymers to broaden the absorption spectra and to modify the open-circuit voltage to further improve the performance of the all-PSCs in the optimal morphology condition, is clearly supported as the complementary absorptions and desired blend morphologies in PBDTTS-FTAZ:PNDI-T10 all-PSCs led to the highest PCE of 6.9%. The importance of the contributions of the donor and acceptor polymers with complementary absorption spectra in light harvesting was highlighted. To further support the hypothesis, PBDTS-TPD:PNDI-T all-PSCs achieved high PCE of 8.0% due to the high  $V_{oc}$  of 1.10 V, resulting from the low-lying HOMO level of the donor and up-lying LUMO of the acceptor. This also demonstrated the advantages of all-PSCs in tuning the  $V_{oc}$  compared to PC<sub>71</sub>BM-based PSCs, as rational design of the structures of donor and acceptor polymers is possible.

In line with the third hypothesis (Section 1.3) regarding the ternary approach, broadened absorption spectra, efficient charge and energy transfer, and optimized blend morphology with reduced charge recombination could be achieved by including a second donor (PBDTTS-FTAZ) to the binary blend. The ternary all-PSCs based on PTB7-Th:PBDTTS-FTAZ:PNDI-T10 attained 9.0% PCE, which is one of the highest PCEs recorded for ternary all-PSCs.

As summarized here, the results described in Chapter 4 verified the approaches proposed to further improve the performances of all-PSCs using NDI-based acceptor polymers.

Broadening the scope of the investigated acceptor polymers, the performances of all-PSCs utilizing acceptor polymers based on other electron-deficient units as building blocks were studied. The advantages of these polymers were that their LUMO levels were higher-lying and their absorption coefficients,  $\alpha$ , were higher than the NDI-based polymers. The acceptor polymer PIID-PyDPP was proved to be a promising acceptor polymer in combination with PBDTTS-FTAZ as a donor. An encouraging PCE of 4.2%, and a high  $V_{oc}$  of 1.07 eV were obtained in PBDTTS-FTAZ:PIID-PyDPP all-PSCs, which is among the best all-PSCs fabricated with DPP-based polymers as acceptors. The PyDPP unit can also be a promising alternative building block to the widely used NDI unit for high-performance and stable all-PSCs. However, all-PSCs containing PyDPP suffered from bimolecular recombination loss due to suboptimal morphologies and relatively low charge mobilities. Thus, further structural optimization of PyDPP-based acceptor polymers is necessary to circumvent these drawbacks. As such, the fourth hypothesis, “*Other electron-deficient units which have been successfully utilized in donor polymers can be promising as building blocks for acceptors, featuring suitable LUMO levels and higher absorption coefficients in comparison with NDI-based polymers.*” is validated. The second research question, “*Is there any other promising acceptor building block except NDI, which can further boost the performance of all-PSCs?*” is partly answered.

Furthermore, PTB7-Th:PNDI-FT10 all-PPD exhibited low  $J_d$  of  $4.09 \times 10^{-5}$  mA/cm<sup>2</sup> and high  $R_{max}$  of 0.37 A/W while simultaneously operating at -5 V bias. These characteristics are among the best reported for all-PPDs to date and are comparable to those of fullerene-based PPDs. The photophysical properties of PPDs were investigated and trap-assisted recombination due to acceptor polymer aggregate was disclosed to be the main origin of higher  $J_d$  in the all-PPDs compared to fullerene-based PPDs, and parallels were drawn to PSC applications. Thus, the fifth hypothesis (Section 1.3) “*Decreasing the content of acceptor polymer can be an effective way to reduce the dark current under the desired morphology condition without sacrificing the photoresponsivity.*” is validated. The final research question “*Is it possible to reduce the dark current of all-PPDs using NDI-based acceptor polymers while maintaining the high EQE achieved in all-PSCs?*” is answered.

Based on the concerted efforts of the scientific community and the results presented in this thesis, we are now moving closer to understanding the correlation between polymer structure, blend morphology, and device performance. Nevertheless, the results achieved in the course of this work also opened several questions that motivate future studies. First, the inferior performances of the all-PSCs based on the acceptor polymers PyDPP, IID and TDQ units were presumed to be mainly due to suboptimal morphology. It is, thus, essential to gain a better control of intermixing between donor and acceptor polymers, and understand the interplay between all the dynamic processes in the devices to produce a high-performing all-PSCs. Especially, since the TDQ-based acceptor polymers showed strong absorption in the NIR region, investigation into further structural modifications of these polymers may exert significant impact on increased all-PSCs and all-PPDs applications.

Secondly, in addition to efficiency limitation, device stability is another primary challenge for all-PSCs, hindering their commercial application. In this thesis, preliminary studies were conducted on device

stability issues, which unraveled undesired fast decays in PCEs and increase in  $J_d$  in the efficient all-PSCs and all-PPDs, including PTB7-Th:PNDI-T10, PTB7-Th:PNDI-FT10, and PBDTS-TPD:PNDI-T systems. So far, the device stabilities of all-PSCs have not been widely investigated. In order to achieve highly-stable all-PSCs for future industrial manufacturing, an in-depth investigation of the device degradation mechanisms with oxygen, water, irradiation, heating and mechanical stress is required.

Finally, considerable batch-to-batch variations were observed in the synthesis of polymers and in device fabrication, which led to variable photovoltaic parameters. The lack of reproducibility is a huge challenge for all-PSCs and all-PPDs to overcome before commercialization. Applying continuous flow chemistry as a viable method for intermediate-scale product synthesis has been reported.<sup>[128]</sup> It is encouraging to note that up to 5% PCE has been achieved by roll-to-roll printed large-area all-PSCs.<sup>[129]</sup> However, the above and other more technical issues pertaining to the performances of all-PSCs and all-PPDs have to be addressed by the scientific community before such devices become commercially viable.



## 9 Methods

---

---

### 9.1 All-PSCs and All-PPDs Fabrication

*Conventional all-PSCs and all-PPDs* were fabricated using the configuration of indium tin oxide (ITO)/PEDOT:PSS (40 nm)/active layer/LiF (1 nm)/Al (100 nm). As a buffer layer, PEDOT:PSS (Baytron P VP Al 4083) was spin-coated onto the ITO at a spin-coating rate of 3000 rpm for 60 s, followed by annealing at 150 °C for 10 mins. The thickness of the PEDOT:PSS layer was around 40 nm, as determined by a Dektak 6 M surface profilometer. Different weight ratios of the donor and acceptor polymers were mixed together and then dissolved in CB at 70 °C-80 °C overnight (depending on the solubility of the polymers) or in CF at 30 °C for 5 h. The active layer was spin-coated from warm CB or CF solution onto the PEDOT:PSS layer in a glove box. LiF (1 nm) and Al (100 nm) were sequentially deposited onto the active layers through a shadow mask which defined the active cell area of 0.09 cm<sup>2</sup> or 0.16 cm<sup>2</sup> under a pressure of 10<sup>-6</sup> kPa.

*Inverted all-PSCs and all-PPDs* were fabricated using an ITO/ ZnO (40 nm)/ Active layer/ MoO<sub>3</sub> (10 nm)/ Ag (100 nm) structure. Sol-gel ZnO (thickness of around 40 nm, determined by a Dektak 6 M surface profilometer) was spin-coated onto the ITO-coated glass substrate at a spinning rate of 4000 rpm for 60 s, followed by annealing at 150 °C for 5 mins. The active layer was then spin-coated on top of the ZnO layer in the glove box. After spin-coating, the films were directly transferred to a vapor deposition system inside of the glove box. MoO<sub>3</sub> (10 nm) and Ag (100 nm) were deposited via a mask under 10<sup>-6</sup> kPa vacuum onto the active layer. The active area of the device was 0.09 cm<sup>2</sup> or 0.16 cm<sup>2</sup>, which was defined by the overlap of the ITO and electrodes and was measured carefully using a microscope.

*Sol-gel method:* Zinc acetate dihydrate (109.7 mg) was mixed with 2-methoxy ethanol (1 mL) and ethanol amine (30.2 µL). The mixture was then stirred at room temperature for 1 h and put into use immediately.

*For solvent annealing treatment* of the active layer, the mixed polymer solution was spin-coated from warm CB solution onto the PEDOT:PSS layer or ZnO layer for around 15 sec. Then the wet film was transferred into a petri dish inside the glove box with a few drops of CB solvent till the film dried. The amount of CB could be varied to control the solvent annealing time.

## 9.2 EQE Measurements

EQE measurements were performed in a home-built setup. All devices were kept in a nitrogen-filled box with a quartz window, and illuminated through a circular aperture with 2 mm diameter. The white light of a 50 W tungsten halogen lamp was modulated with a mechanical chopper and passed through a monochromator. For the EQE under bias light, a 530 nm high power LED was used to illuminate the solar cell simultaneously under the mechanically modulated monochromatic light. For both unbiased and bias EQE measurements, the differential photocurrent density was picked up by a lock-in amplifier. The current was recorded as the voltage over a 50  $\Omega$  resistance, and was converted to EQE profile by comparing the data with a calibrated silicon reference cell. The  $J_{sc}^{EQE}$  was determined by integrating the EQE spectrum with the AM1.5G solar spectrum.

## 9.3 SCLC Mobility Measurements

The charge carrier drift mobility measured by the SCLC method was based on the analysis of  $J$ - $V$  characteristics in the dark.<sup>[130]</sup> At low applied voltage, the  $J$ - $V$  characteristics were generally linear, showing Ohmic behavior. While at high applied voltage, the  $J$ - $V$  characteristics became space-charge-limited, due to the injection of charge carriers from one electrode. When the contact between the electrode and the active layer was Ohmic and the current was transport-limited instead of injection-limited, the *space-charge-limited photocurrent density* was described by the Mott-Gurney equation:<sup>[131]</sup>

$$J = \frac{9}{8} \varepsilon_0 \varepsilon_r \mu \frac{V^2}{d^3} \quad (9.1)$$

where the  $\varepsilon_r$  was assumed to be 3.

For blend devices, the presence of Ohmic contacts at both interfaces could lead to a SCLC, which was from a combination of both electrons and holes. To measure the SCLC of only one type of charge carrier, the other one was suppressed by a large injection barrier, resulting in an electron or hole only device. In this thesis, the  $\mu_h$  was measured in a device composed of ITO (170 nm)/PEDOT:PSS (40 nm)/active layer/MoO<sub>3</sub> (10 nm)/Ag(100 nm). The blend films were spin-coated on ITO substrates covered with 40 nm PEDOT:PSS. Then MoO<sub>3</sub> (10 nm) and Ag (100 nm) were vacuum-deposited on the active layer as the cathode. The  $\mu_e$  is measured in a device composed of ITO (170 nm)/ZnO (40 nm)/active layer/LiF(1 nm)/Al (100 nm). The blend films are spin-coated on ITO substrates covered with a layer of ZnO (40 nm). Then 1 nm LiF and 100 nm Al are vacuum-deposited on the active layers as the cathode. The mobility  $\mu$  was determined by fitting the  $J^{1/2}$ - $V$  curve to the model of a single carrier SCLC.

## 9.4 Photon Absorptance Simulation

The refractive index ( $n$ ), extinction coefficient ( $k$ ) and thicknesses of the glass substrate, active layer, interlayers and electrodes were included as input to simulate the actual absorption distribution of the all-PSC. The absorbed photon flux was calculated using a simulation of the optical absorption and reflection within a full stack of layers by transfer matrix formalism (TMF).<sup>[132]</sup> The wavelength-dependent  $n$  and  $k$  values of the active layer were calculated from the transmittance and reflection. The

*n* value was calculated using the python script which was provided by Dr. Harm van Eersel. The total absorption of the active layer was simulated based on Glass (100 nm)/SiO<sub>2</sub> (20 nm)/ITO (170 nm)/PEDOT:PSS (40 nm)/active layer (optimized film thickness in the device)/Al (100 nm) for conventional device structure and Glass (100 nm)/SiO<sub>2</sub> (20 nm)/ITO (170 nm)/ZnO (40 nm)/active layer (optimized film thickness in the device)/MoO<sub>3</sub> (10 nm)/Ag (100 nm) for inverted device structure. The thicknesses of the active layer, charge transport layer and electrodes were the same as those in PSCs and PPDs.

## References

---

---

- [1] P. Bhattacharya, *Semiconductor optoelectronic devices*, Prentice-Hall, Inc., 1994.
- [2] a) N. S. Lewis, Mrs. Bull. 2007, 32, 808; b) M. Tao, *Terawatt solar photovoltaics: roadblocks and opportunities*, Springer, 2014.
- [3] a) E. R. Fossum, D. B. Hondo, IEEE J. Electron Devices Soc. 2014, 2, 33; b) P. Dennis, *Photodetectors: an introduction to current technology*, Springer Science & Business Media, 2012.
- [4] a) S. Gong, W. Cheng, Adv. Energy Mater. 2017, 1700648; b) A. E. Ostfeld, A. C. Arias, Flex. Print. Electron. 2017, 2, 013001.
- [5] G. Li, R. Zhu, Y. Yang, Nat. Photon. 2012, 6, 153.
- [6] a) N. Espinosa, M. Hösel, D. Angmo, F. C. Krebs, Energy Environ. Sci. 2012, 5, 5117; b) S. B. Darling, F. You, RSC Adv. 2013, 3, 17633.
- [7] a) M. A. Green, Y. Hishikawa, W. Warta, E. D. Dunlop, D. H. Levi, J. Hohl-Ebinger, A. W. Ho-Baillie, Prog. Photovolt: Res. Appl. 2017, 25, 668; b) W. Zhao, S. Li, H. Yao, S. Zhang, Y. Zhang, B. Yang, J. Hou, J. Am. Chem. Soc. 2017, 139, 7148; c) Z. Fei, F. D. Eisner, X. Jiao, M. Azzouzi, J. A. Röhr, Y. Han, M. Shahid, A. S. Chesman, C. D. Easton, C. R. McNeill, Adv. Mater. 2018, 1705209.
- [8] S. Wu, B. Xiao, B. Zhao, Z. He, H. Wu, Y. Cao, Small 2016, 12, 3374.
- [9] a) R. Nie, Y. Wang, X. Deng, ACS Appl. Mater. Interfaces 2014, 6, 7032; b) L. Zhang, T. Yang, L. Shen, Y. Fang, L. Dang, N. Zhou, X. Guo, Z. Hong, Y. Yang, H. Wu, Adv. Mater. 2015, 27, 6496; c) E. Saracco, B. Bouthinon, J. M. Verilhac, C. Celle, N. Chevalier, D. Mariolle, O. Dhez, J. P. Simonato, Adv. Mater. 2013, 25, 6534; d) S. F. Tedde, J. Kern, T. Sterzl, J. Furst, P. Lugli, O. Hayden, Nano Lett. 2009, 9, 980; e) S. H. Eom, S. Y. Nam, H. J. Do, J. Lee, S. Jeon, T. J. Shin, I. H. Jung, S. C. Yoon, C. Lee, Polym. Chem. 2017, 8, 3612; f) S. Xiong, J. Tong, L. Mao, Z. Li, F. Qin, F. Jiang, W. Meng, T. Liu, W. Li, Y. Zhou, J. Mater. Chem. C 2016, 4, 1414; g) E. Y. Choi, S. H. Eom, C. E. Song, S. Y. Nam, J. Lee, H. Y. Woo, I. H. Jung, S. C. Yoon, C. Lee, Org. Electron. 2017, 46, 173.
- [10] C. K. Chiang, C. Fincher Jr, Y. W. Park, A. J. Heeger, H. Shirakawa, E. J. Louis, S. C. Gau, A. G. MacDiarmid, Phys. Rev. Lett. 1977, 39, 1098.
- [11] M. Barón, K.-H. Hellwich, M. Hess, K. Horie, A. D. Jenkins, R. G. Jones, J. Kahovec, P. Kratochvíl, W. V. Metanomski, W. Mormann, Pure Appl. Chem. 2009, 81, 1131.
- [12] a) H. Kang, W. Lee, J. Oh, T. Kim, C. Lee, B. J. Kim, Accounts. Chem. Res. 2016, 49, 2424; b) H. Benten, D. Mori, H. Ohkita, S. Ito, J. Mater. Chem. A 2016, 4, 5340.
- [13] M. S. Vezie, S. Few, I. Meager, G. Pieridou, B. Dörling, R. S. Ashraf, A. R. Goñi, H. Bronstein, I. McCulloch, S. C. Hayes, Nat. Mater. 2016, 15, 746.
- [14] H. Yao, L. Ye, H. Zhang, S. Li, S. Zhang, J. Hou, Chem. Rev. 2016, 116, 7397.

- [15] T. Kim, J.-H. Kim, T. E. Kang, C. Lee, H. Kang, M. Shin, C. Wang, B. Ma, U. Jeong, T.-S. Kim, *Nat. Commun.* 2015, 6, 8547.
- [16] J.-L. Bredas, *Mater. Horiz.* 2014, 1, 17.
- [17] J. C. Costa, R. J. Taveira, C. F. Lima, A. Mendes, L. M. Santos, *Opt. Mater.* 2016, 58, 51.
- [18] P. Bujak, I. Kuliszewicz-Bajer, M. Zagorska, V. Maurel, I. Wielgus, A. Pron, *Chem. Soc. Rev.* 2013, 42, 8895.
- [19] a) J. G. Osteryoung, R. A. Osteryoung, *Anal. Chem.* 1985, 57, 101; b) W. Mammo, S. Admassie, A. Gadisa, F. Zhang, O. Inganäs, M. R. Andersson, *Sol. Energ. Mat. Sol. C.* 2007, 91, 1010.
- [20] C. M. Cardona, W. Li, A. E. Kaifer, D. Stockdale, G. C. Bazan, *Adv. Mater.* 2011, 23, 2367.
- [21] a) J.-L. Brédas, *J. Chem. Phys.* 1985, 82, 3808; b) P. von Ragué Schleyer, *Chem. Rev.* 2001, 5, 1115.
- [22] a) Y.-J. Cheng, S.-H. Yang, C.-S. Hsu, *Chem. Rev.* 2009, 109, 5868; b) C. Liu, K. Wang, X. Gong, A. J. Heeger, *Chem. Soc. Rev.* 2016, 45, 4825.
- [23] F. Wudl, M. Kobayashi, A. Heeger, *J. Org. Chem.* 1984, 49, 3382.
- [24] J. Brédas, A. Heeger, F. Wudl, *J. Chem. Phys.* 1986, 85, 4673.
- [25] J. Brédas, A. Heeger, *Chem. Phys. Lett.* 1994, 217, 507.
- [26] a) M. Wang, X. Hu, P. Liu, W. Li, X. Gong, F. Huang, Y. Cao, *J. Am. Chem. Soc.* 2011, 133, 9638; b) M. C. Scharber, D. Mühlbacher, M. Koppe, P. Denk, C. Waldauf, A. J. Heeger, C. J. Brabec, *Adv. Mater.* 2006, 18, 789.
- [27] a) C. Kitamura, S. Tanaka, Y. Yamashita, *Chem. Mater.* 1996, 8, 570; b) G. Brocks, A. Tol, J. Phys. Chem. 1996, 100, 1838.
- [28] H. Zhou, L. Yang, S. Stoneking, W. You, *ACS Appl. Mater. Interfaces* 2010, 2, 1377.
- [29] G. R. Hutchison, M. A. Ratner, T. J. Marks, *J. Am. Chem. Soc.* 2005, 127, 16866.
- [30] J. Hou, Z. a. Tan, Y. Yan, Y. He, C. Yang, Y. Li, *J. Am. Chem. Soc.* 2006, 128, 4911.
- [31] a) G. C. Schmidt, D. Höft, K. Haase, A. C. Hübner, E. Karpov, R. Tkachov, M. Stamm, A. Kiriy, F. Haidu, D. Zahn, *J. Mater. Chem. C* 2014, 2, 5149; b) B. Carsten, F. He, H. J. Son, T. Xu, L. Yu, *Chem. Rev.* 2011, 111, 1493; c) A. Marrocchi, A. Facchetti, D. Lanari, C. Petrucci, L. Vaccaro, *Energy Environ. Sci.* 2016, 9, 763.
- [32] T. Yamamoto, A. Morita, Y. Miyazaki, T. Maruyama, H. Wakayama, Z. H. Zhou, Y. Nakamura, T. Kanbara, S. Sasaki, K. Kubota, *Macromolecules* 1992, 25, 1214.
- [33] a) J. Kuwabara, T. Yasuda, S. J. Choi, W. Lu, K. Yamazaki, S. Kagaya, L. Han, T. Kanbara, *Adv. Funct. Mater.* 2014, 24, 3226; b) K. Okamoto, J. Zhang, J. B. Housekeeper, S. R. Marder, C. K. Luscombe, *Macromolecules* 2013, 46, 8059; c) R. Matsidik, H. Komber, A. Luzio, M. Caironi, M. Sommer, *J. Am. Chem. Soc.* 2015, 137, 6705.
- [34] N. Miyaura, A. Suzuki, *Chem. Rev.* 1995, 95, 2457.
- [35] C. Amatore, A. Jutand, G. Le Duc, *Chem-eur. J.* 2011, 17, 2492.
- [36] S. M. Menke, N. A. Ran, G. C. Bazan, R. H. Friend, *Joule* 2018, 2, 1.

- [37] a) J. Liu, S. Chen, D. Qian, B. Gautam, G. Yang, J. Zhao, J. Bergqvist, F. Zhang, W. Ma, H. Ade, Nat. Energy 2016, 1, 16089; b) P. Cheng, M. Zhang, T. K. Lau, Y. Wu, B. Jia, J. Wang, C. Yan, M. Qin, X. Lu, X. Zhan, Adv. Mater. 2017, 29, 1605216.
- [38] a) B. Kippelen, J.-L. Brédas, Energy Environ. Sci. 2009, 2, 251; b) Y. Jiang, Y. Li, J. Tong, L. Mao, Y. Zhou, F. Zhang, in *Molecular Devices for Solar Energy Conversion and Storage*, Springer, 2018, 45; c) M. Scharber, N. Sariciftci, in *Nanostructured Materials for Type III Photovoltaics*, Vol. 45, 2017, 33.
- [39] a) J.-M. Verilhac, Eur. Phys. J. Appl. Phys. 2013, 63, 14405; b) M. R. Esopi, M. Calcagno, Q. Yu, Adv. Mater. Technol. 2017, 1700025.
- [40] C. W. Tang, Appl. Phys. Lett. 1986, 48, 183.
- [41] N. Sariciftci, D. Braun, C. Zhang, V. Srdanov, A. Heeger, G. Stucky, F. Wudl, Appl. Phys. Lett. 1993, 62, 585.
- [42] P. W. Blom, V. D. Mihailescu, L. J. A. Koster, D. E. Markov, Adv. Mater. 2007, 19, 1551.
- [43] a) J. Halls, C. Walsh, N. C. Greenham, E. Marseglia, R. H. Friend, S. Moratti, A. Holmes, Nature 1995, 376, 498; b) G. Yu, J. Gao, J. C. Hummelen, F. Wudl, A. J. Heeger, Science 1995, 270, 1789.
- [44] S. Rühle, Sol. Energy 2016, 130, 139.
- [45] W. Shockley, H. J. Queisser, J. Appl. Phys. 1961, 32, 510.
- [46] O. Ostroverkhova, Chem. Rev. 2016, 116, 13279.
- [47] K. Vandewal, A. Gadisa, W. D. Oosterbaan, S. Bertho, F. Banishoeib, I. Van Severen, L. Lutsen, T. J. Cleij, D. Vanderzande, J. V. Manca, Adv. Funct. Mater. 2008, 18, 2064.
- [48] D. Bartesaghi, I. del Carmen Pérez, J. Kniepert, S. Roland, M. Turbiez, D. Neher, L. J. A. Koster, Nat. Commun. 2015, 6, 7083.
- [49] a) K. J. Baeg, M. Binda, D. Natali, M. Caironi, Y. Y. Noh, Adv. Mater. 2013, 25, 4267; b) H. Dong, H. Zhu, Q. Meng, X. Gong, W. Hu, Chem. Soc. Rev. 2012, 41, 1754.
- [50] a) M. Kielar, O. Dhez, G. Pecastaings, A. Curutchet, L. Hirsch, Sci. Rep. 2016, 6, 39201; b) X. Zhou, D. Yang, D. Ma, Adv. Optical Mater. 2015, 3, 1570.
- [51] Y. Yao, Y. Liang, V. Shrotriya, S. Xiao, L. Yu, Y. Yang, Adv. Mater. 2007, 19, 3979.
- [52] a) T. W. Holcombe, C. H. Woo, D. F. Kavulak, B. C. Thompson, J. M. Fréchet, J. Am. Chem. Soc. 2009, 131, 14160; b) D. Mori, H. Benten, H. Ohkita, S. Ito, K. Miyake, ACS Appl. Mater. Interfaces 2012, 4, 3325; c) M. Granström, K. Petritsch, A. Arias, A. Lux, M. Andersson, R. Friend, Nature 1998, 395, 257; d) C. R. McNeill, A. Abrusci, J. Zaumseil, R. Wilson, M. J. McKiernan, J. H. Burroughes, J. J. Halls, N. C. Greenham, R. H. Friend, Appl. Phys. Lett. 2007, 90, 193506.
- [53] a) T. Kietzke, H.-H. Hörlold, D. Neher, Chem. Mater. 2005, 17, 6532; b) X. He, F. Gao, G. Tu, D. Hasko, S. Huttner, U. Steiner, N. C. Greenham, R. H. Friend, W. T. Huck, Nano Lett. 2010, 10, 1302.

- [54] a) X. Zhan, Z. a. Tan, B. Domercq, Z. An, X. Zhang, S. Barlow, Y. Li, D. Zhu, B. Kippelen, S. R. Marder, *J. Am. Chem. Soc.* 2007, 129, 7246; b) Y. Guo, Y. Li, O. Awartani, J. Zhao, H. Han, H. Ade, D. Zhao, H. Yan, *Adv. Mater.* 2016, 28, 8483.
- [55] a) E. Zhou, M. Nakano, S. Izawa, J. Cong, I. Osaka, K. Takimiya, K. Tajima, *ACS Macro Lett.* 2014, 3, 872; b) J. Yang, B. Xiao, K. Tajima, M. Nakano, K. Takimiya, A. Tang, E. Zhou, *Macromolecules* 2017, 50, 3179.
- [56] a) X. Long, Z. Ding, C. Dou, J. Zhang, J. Liu, L. Wang, *Adv. Mater.* 2016, 28, 6504; b) Z. Ding, X. Long, C. Dou, J. Liu, L. Wang, *Chem. Sci.* 2016, 7, 6197.
- [57] a) W. Li, Y. An, M. M. Wienk, R. A. Janssen, *J. Mater. Chem. A* 2015, 3, 6756; b) A. Zhang, Q. Wang, R. A. Bovee, C. Li, J. Zhang, Y. Zhou, Z. Wei, Y. Li, R. A. Janssen, Z. Wang, *J. Mater. Chem. A* 2016, 4, 7736.
- [58] a) S. Liu, Z. Kan, S. Thomas, F. Cruciani, J. L. Brédas, P. M. Beaujuge, *Angew. Chem.* 2016, 128, 13190; b) S. Liu, Y. Firdaus, S. Thomas, Z. Kan, F. Cruciani, S. Lopatin, J. L. Bredas, P. M. Beaujuge, *Angew. Chem. Int. Ed.* 2018, 57, 531.
- [59] Z. G. Zhang, Y. Yang, J. Yao, L. Xue, S. Chen, X. Li, W. Morrison, C. Yang, Y. Li, *Angew. Chem. Int. Ed.* 2017, 56, 13503.
- [60] Y. Wang, Z. Yan, H. Guo, M. A. Uddin, S. Ling, X. Zhou, H. Su, J. Dai, H. Y. Woo, X. Guo, *Angew. Chem. Int. Ed.* 2017, 56, 1.
- [61] B. Fan, L. Ying, P. Zhu, F. Pan, F. Liu, J. Chen, F. Huang, Y. Cao, *Adv. Mater.* 2017, 1703906.
- [62] P. E. Keivanidis, S.-H. Khong, P. K. Ho, N. C. Greenham, R. H. Friend, *Appl. Phys. Lett.* 2009, 94, 123.
- [63] a) J. Qi, W. Qiao, X. Zhou, D. Yang, J. Zhang, D. Ma, Z. Y. Wang, *Macromol. Chem. Phys.* 2016, 217, 1683; b) L. Hu, W. Qiao, X. Zhou, X. Zhang, D. Ma, Y. Li, Z. Y. Wang, *Polymer* 2017, 114, 173; c) I. K. Kim, B. N. Pal, M. Ullah, P. L. Burn, S. C. Lo, P. Meredith, E. B. Namdas, *Adv. Optical Mater.* 2015, 3, 50.
- [64] Q. Wang, J. Qi, W. Qiao, Z. Y. Wang, *Dyes. Pigments* 2015, 113, 160.
- [65] X. Wang, L. Lv, L. Li, Y. Chen, K. Zhang, H. Chen, H. Dong, J. Huang, G. Shen, Z. Yang, *Adv. Funct. Mater.* 2016, 26, 6306.
- [66] L. Hu, W. Qiao, J. Han, X. Zhou, C. Wang, D. Ma, Z. Y. Wang, Y. Li, *Polym. Chem.* 2017, 8, 528.
- [67] L. Hu, J. Han, W. Qiao, X. Zhou, C.-L. Wang, D. Ma, Y. Li, Z. Y. Wang, *Polym. Chem.* 2018, 9, 327.
- [68] C. M. Proctor, M. Kuik, T.-Q. Nguyen, *Prog. Polym. Sci.* 2013, 38, 1941.
- [69] V. Mihailetti, L. Koster, J. Hummelen, P. Blom, *Phys. Rev. Lett.* 2004, 93, 216601.
- [70] a) S. Albrecht, W. Schindler, J. Kurpiers, J. Kniepert, J. C. Blakesley, I. Dumsch, S. Allard, K. Fostiropoulos, U. Scherf, D. Neher, *J. Phys. Chem. Lett.* 2012, 3, 640; b) S. Albrecht, S. Janietz, W. Schindler, J. Frisch, J. Kurpiers, J. Kniepert, S. Inal, P. Pingel, K. Fostiropoulos, N. Koch, *J. Am. Chem. Soc.* 2012, 134, 14932.

- [71] R. Street, S. Cowan, A. Heeger, Phys. Rev. B 2010, 82, 121301.
- [72] a) G. Lakhwani, A. Rao, R. H. Friend, Annu. Rev. Phys. Chem. 2014, 65, 557; b) S. R. Cowan, N. Banerji, W. L. Leong, A. J. Heeger, Adv. Funct. Mater. 2012, 22, 1116.
- [73] S. Roland, M. Schubert, B. A. Collins, J. Kurpiers, Z. Chen, A. Facchetti, H. Ade, D. Neher, J. Phys. Chem. Lett. 2014, 5, 2815.
- [74] a) L. Koster, M. Kemerink, M. M. Wienk, K. Maturová, R. A. Janssen, Adv. Mater. 2011, 23, 1670; b) D. J. Wehenkel, K. H. Hendriks, M. M. Wienk, R. A. Janssen, Org. Electron. 2012, 13, 3284.
- [75] T. Kirchartz, F. Deledalle, P. S. Tuladhar, J. R. Durrant, J. Nelson, J. Phys. Chem. Lett. 2013, 4, 2371.
- [76] G. Wetzelar, M. Kuik, M. Lenes, P. Blom, Appl. Phys. Lett. 2011, 99, 153506.
- [77] V. Brus, Org. Electron. 2016, 29, 1.
- [78] L. J. A. Koster, V. D. Mihailescu, R. Ramaker, P. W. Blom, Appl. Phys. Lett. 2005, 86, 123509.
- [79] M. Schubert, B. A. Collins, H. Mangold, I. A. Howard, W. Schindler, K. Vandewal, S. Roland, J. Behrends, F. Kraffert, R. Steyrleuthner, Adv. Funct. Mater. 2014, 24, 4068.
- [80] a) C. R. McNeill, Energy Environ. Sci. 2012, 5, 5653; b) P. K. Watkins, A. B. Walker, G. L. Verschoor, Nano Lett. 2005, 5, 1814.
- [81] G. Strobl, in *The physics of polymers-concepts for understanding their structures and behavior*, Springer, 2007, 106.
- [82] Y.-J. Hwang, T. Earmme, B. A. Courtright, F. N. Eberle, S. A. Jenekhe, J. Am. Chem. Soc. 2015, 137, 4424.
- [83] S. Shi, J. Yuan, G. Ding, M. Ford, K. Lu, G. Shi, J. Sun, X. Ling, Y. Li, W. Ma, Adv. Funct. Mater. 2016, 26, 5669.
- [84] S. Feng, C. Liu, X. Xu, X. Liu, L. Zhang, Y. Nian, Y. Cao, J. Chen, ACS Macro Lett. 2017, 6, 1310.
- [85] a) C. Duan, R. E. Willems, J. J. van Franeker, B. J. Bruijnaers, M. M. Wienk, R. A. Janssen, J. Mater. Chem. A 2016, 4, 1855; b) C. Cui, Z. He, Y. Wu, X. Cheng, H. Wu, Y. Li, Y. Cao, W.-Y. Wong, Energy Environ. Sci. 2016, 9, 885; c) J. Yuan, L. Qiu, Z. Zhang, Y. Li, Y. He, L. Jiang, Y. Zou, Chem. Commun. 2016, 52, 6881.
- [86] C. Lee, H. Kang, W. Lee, T. Kim, K. H. Kim, H. Y. Woo, C. Wang, B. J. Kim, Adv. Mater. 2015, 27, 2466.
- [87] J. W. Jung, J. W. Jo, C. C. Chueh, F. Liu, W. H. Jo, T. P. Russell, A. K. Y. Jen, Adv. Mater. 2015, 27, 3310.
- [88] H.-H. Cho, T. Kim, K. Kim, C. Lee, F. S. Kim, B. J. Kim, J. Mater. Chem. A 2017, 5, 5449.
- [89] a) S. Chen, Y. An, G. K. Dutta, Y. Kim, Z. G. Zhang, Y. Li, C. Yang, Adv. Funct. Mater. 2017, 27, 1603564; b) J. Jung, W. Lee, C. Lee, H. Ahn, B. J. Kim, Adv. Energy Mater. 2016, 6, 1600504.

- [90] N. Zhou, A. S. Dudnik, T. I. Li, E. F. Manley, T. J. Aldrich, P. Guo, H.-C. Liao, Z. Chen, L. X. Chen, R. P. Chang, *J. Am. Chem. Soc.* 2016, 138, 1240.
- [91] G. Wang, N. D. Eastham, T. J. Aldrich, B. Ma, E. F. Manley, Z. Chen, L. X. Chen, M. O. de la Cruz, R. P. Chang, F. S. Melkonyan, *Adv. Energy Mater.* 2018, 1702173.
- [92] D. Mori, H. Benten, J. Kosaka, H. Ohkita, S. Ito, K. Miyake, *ACS Appl. Mater. Interfaces* 2011, 3, 2924.
- [93] X. Liu, S. Huettner, Z. Rong, M. Sommer, R. H. Friend, *Adv. Mater.* 2012, 24, 669.
- [94] H. Kang, K.-H. Kim, J. Choi, C. Lee, B. J. Kim, *ACS Macro Lett.* 2014, 3, 1009.
- [95] H. Kang, M. A. Uddin, C. Lee, K.-H. Kim, T. L. Nguyen, W. Lee, Y. Li, C. Wang, H. Y. Woo, B. J. Kim, *J. Am. Chem. Soc.* 2015, 137, 2359.
- [96] L. Ye, X. Jiao, H. Zhang, S. Li, H. Yao, H. Ade, J. Hou, *Macromolecules* 2015, 48, 7156.
- [97] H.-H. Cho, G. Han, R. Younts, W. Lee, B. R. Gautam, S. Lee, C. Lee, T. Kim, F. S. Kim, K. Gundogdu, *J. Mater. Chem. A* 2017, 5, 21291.
- [98] P. Cheng, L. Ye, X. Zhao, J. Hou, Y. Li, X. Zhan, *Energy Environ. Sci.* 2014, 7, 1351.
- [99] H. I. Kim, M. Kim, C. W. Park, H. U. Kim, H.-K. Lee, T. Park, *Chem. Mater.* 2017, 29, 6793.
- [100] F. Laquai, D. Andrienko, C. Deibel, D. Neher, in *Elementary Processes in Organic Photovoltaics*, Springer, 2017, 267.
- [101] a) Y. J. Hwang, B. A. Courtright, A. S. Ferreira, S. H. Tolbert, S. A. Jenekhe, *Adv. Mater.* 2015, 27, 4578; b) D. Mori, H. Benten, H. Ohkita, S. Ito, *Adv. Energy Mater.* 2015, 5, 1500304.
- [102] a) L. Gao, Z. G. Zhang, L. Xue, J. Min, J. Zhang, Z. Wei, Y. Li, *Adv. Mater.* 2016, 28, 1884; b) B. Fan, L. Ying, Z. Wang, B. He, X.-F. Jiang, F. Huang, Y. Cao, *Energy Environ. Sci.* 2017, 10, 1243; c) W. Huang, M. Li, F. Lin, Y. Wu, Z. Ke, X. Zhang, R. Ma, T. Yang, W. Ma, Y. Liang, *Mol. Syst. Des. Eng.* 2018, 3, 103.
- [103] D. Mori, H. Benten, I. Okada, H. Ohkita, S. Ito, *Energy Environ. Sci.* 2014, 7, 2939.
- [104] S. A. Jenekhe, L. Lu, M. M. Alam, *Macromolecules* 2001, 34, 7315.
- [105] L. Ye, S. Zhang, W. Zhao, H. Yao, J. Hou, *Chem. Mater.* 2014, 26, 3603.
- [106] a) N. Zhou, H. Lin, S. J. Lou, X. Yu, P. Guo, E. F. Manley, S. Loser, P. Hartnett, H. Huang, M. R. Wasielewski, *Adv. Energy Mater.* 2014, 4, 1300785; b) C. Mu, P. Liu, W. Ma, K. Jiang, J. Zhao, K. Zhang, Z. Chen, Z. Wei, Y. Yi, J. Wang, *Adv. Mater.* 2014, 26, 7224; c) Y. Xia, C. Musumeci, J. Bergqvist, W. Ma, F. Gao, Z. Tang, S. Bai, Y. Jin, C. Zhu, R. Kroon, *J. Mater. Chem. A* 2016, 4, 3835.
- [107] Y.-J. Hwang, T. Earmme, S. Subramaniyan, S. A. Jenekhe, *Chem. Commun.* 2014, 50, 10801.
- [108] C. Müller, E. Wang, L. M. Andersson, K. Tvingstedt, Y. Zhou, M. R. Andersson, O. Inganäs, *Adv. Funct. Mater.* 2010, 20, 2124.
- [109] Z. Genene, J. Wang, X. Meng, W. Ma, X. Xu, R. Yang, W. Mammo, E. Wang, *Adv. Electron. Mater.* 2016, 2, 1600084.
- [110] C. M. Proctor, J. A. Love, T. Q. Nguyen, *Adv. Mater.* 2014, 26, 5957.

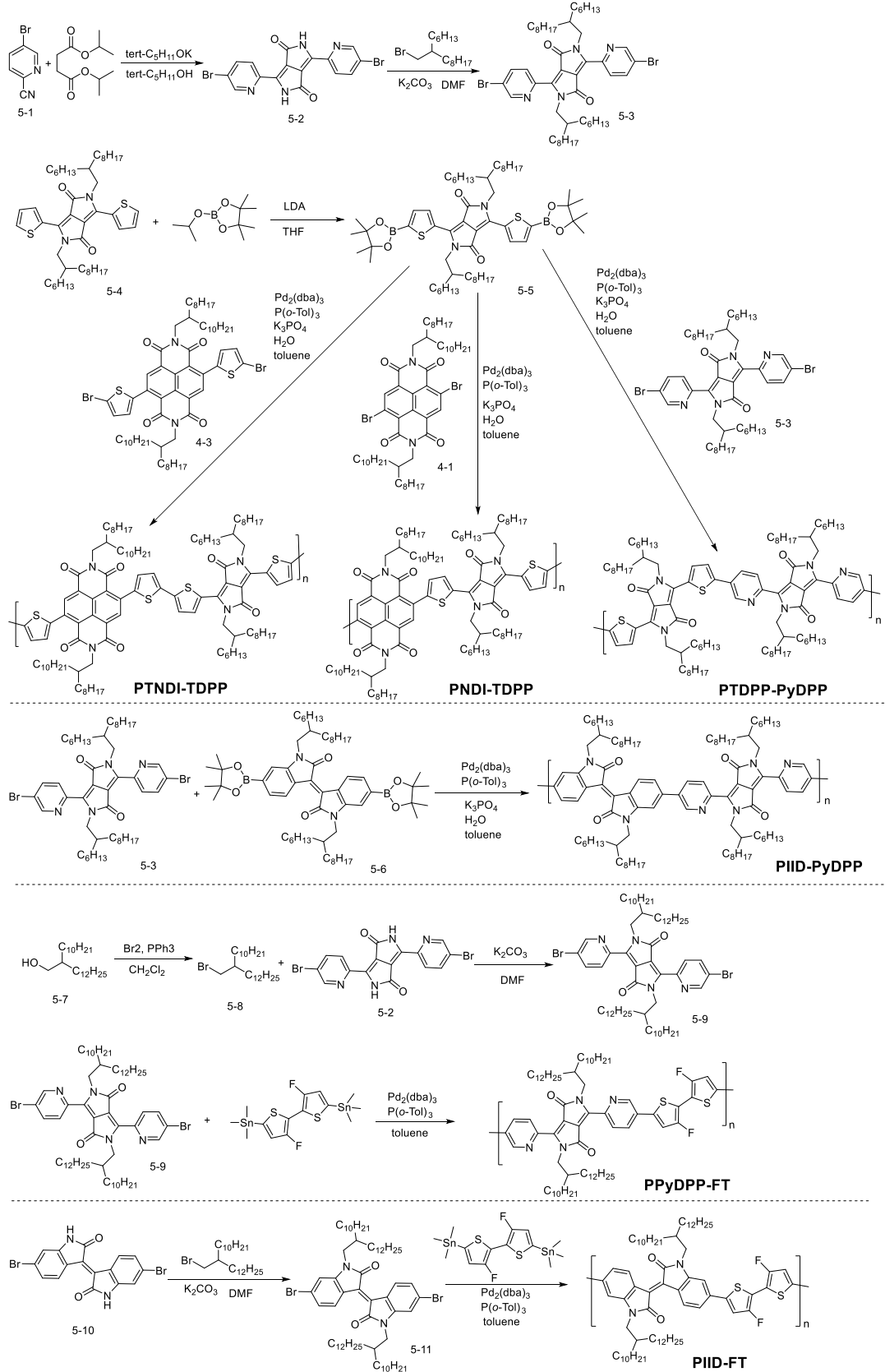
- [111] L. Lu, M. A. Kelly, W. You, L. Yu, *Nat. Photon.* 2015, 9, 491.
- [112] a) E. Wang, W. Mammo, M. R. Andersson, *Adv. Mater.* 2014, 26, 1801; b) C. B. Nielsen, M. Turbiez, I. McCulloch, *Adv. Mater.* 2013, 25, 1859; c) X. Guo, A. Facchetti, T. J. Marks, *Chem. Rev.* 2014, 114, 8943.
- [113] a) R. Stalder, J. Mei, J. Subbiah, C. Grand, L. A. Estrada, F. So, J. R. Reynolds, *Macromolecules* 2011, 44, 6303; b) W. Li, W. Roelofs, M. Turbiez, M. M. Wienk, R. A. Janssen, *Adv. Mater.* 2014, 26, 3304.
- [114] a) J. W. Jung, F. Liu, T. P. Russell, W. H. Jo, *Chem. Commun.* 2013, 49, 8495; b) B. Sun, W. Hong, Z. Yan, H. Aziz, Y. Li, *Adv. Mater.* 2014, 26, 2636.
- [115] a) K. D. Deshmukh, T. Qin, J. K. Gallaher, A. C. Liu, E. Gann, K. O'Donnell, L. Thomsen, J. M. Hodgkiss, S. E. Watkins, C. R. McNeill, *Energy Environ. Sci.* 2015, 8, 332; b) J. Choi, K.-H. Kim, H. Yu, C. Lee, H. Kang, I. Song, Y. Kim, J. H. Oh, B. J. Kim, *Chem. Mater.* 2015, 27, 5230.
- [116] S. H. Liao, H. J. Jhuo, Y. S. Cheng, S. A. Chen, *Adv. Mater.* 2013, 25, 4766.
- [117] T. T. Steckler, P. Henriksson, S. Mollinger, A. Lundin, A. Salleo, M. R. Andersson, *J. Am. Chem. Soc.* 2014, 136, 1190.
- [118] a) A. P. Zoombelt, M. Fonrodona, M. M. Wienk, A. B. Sieval, J. C. Hummelen, R. A. Janssen, *Org. Lett.* 2009, 11, 903; b) J. Yu, Q. An, J. Hai, X. Nie, B. Zhou, F. Zhang, W. Tang, *Polymer* 2015, 79, 12; c) M. Keshtov, S. Kuklin, N. Radychev, A. Y. Nikolaev, E. Koukaras, A. Sharma, G. Sharma, *RSC Adv.* 2016, 6, 14893.
- [119] C. An, S. R. Puniredd, X. Guo, T. Stelzig, Y. Zhao, W. Pisula, M. Baumgarten, *Macromolecules* 2014, 47, 979.
- [120] S.-i. Kato, K. Watanabe, M. Tamura, M. Ueno, M. Nitani, Y. Ie, Y. Aso, T. Yamanobe, H. Uehara, Y. Nakamura, *J. Org. Chem.* 2017, 82, 3132.
- [121] J. R. Lakowicz, in *Principles of Fluorescence Spectroscopy, Third Edition*, Springer, 2008, 687.
- [122] S. D. Dimitrov, B. C. Schroeder, C. B. Nielsen, H. Bronstein, Z. Fei, I. McCulloch, M. Heeney, J. R. Durrant, *Polymers* 2016, 8, 14.
- [123] P. E. Keivanidis, P. K. Ho, R. H. Friend, N. C. Greenham, *Adv. Funct. Mater.* 2010, 20, 3895.
- [124] a) M. Kielar, O. Dhez, G. Pecastaings, A. Curutchet, L. Hirsch, *Sci. Rep.* 2016, 6; b) S. Yoon, J. Cho, K. M. Sim, J. Ha, D. S. Chung, *Appl. Phys. Lett.* 2017, 110, 083301; c) J. Jeong, S. Nam, H. Kim, Y. Kim, *IEEE. J. Sel. Top. Quant* 2014, 20, 130.
- [125] M. Jørgensen, K. Norrman, S. A. Gevorgyan, T. Tromholt, B. Andreasen, F. C. Krebs, *Adv. Mater.* 2012, 24, 580.
- [126] Z. Li, F. Gao, N. C. Greenham, C. R. McNeill, *Adv. Funct. Mater.* 2011, 21, 1419.
- [127] a) C. R. McNeill, I. Hwang, N. C. Greenham, *J. Appl. Phys.* 2009, 106, 024507; b) C. Sun, Z. Wu, Z. Hu, J. Xiao, W. Zhao, H.-W. Li, Q.-Y. Li, S.-W. Tsang, Y.-X. Xu, K. Zhang, *Energy Environ. Sci.* 2017, 10, 1784.

- [128] G. Pirotte, J. Kesters, P. Verstappen, S. Govaerts, J. Manca, L. Lutsen, D. Vanderzande, W. Maes, ChemSusChem 2015, 8, 3228.
- [129] X. Gu, Y. Zhou, K. Gu, T. Kurosawa, Y. Guo, Y. Li, H. Lin, B. C. Schroeder, H. Yan, F. Molina-Lopez, Adv. Energy Mater. 2017, 7, 1602742.
- [130] S. Tiwari, N. Greenham, Opt. Quant. Electron 2009, 41, 69.
- [131] P. M. Murray A. Lampert, *Current injection in solids*, Academic Press, New York, 1970.
- [132] G. Dennler, M. C. Scharber, C. J. Brabec, Adv. Mater. 2009, 21, 1323.

# Appendix I

---

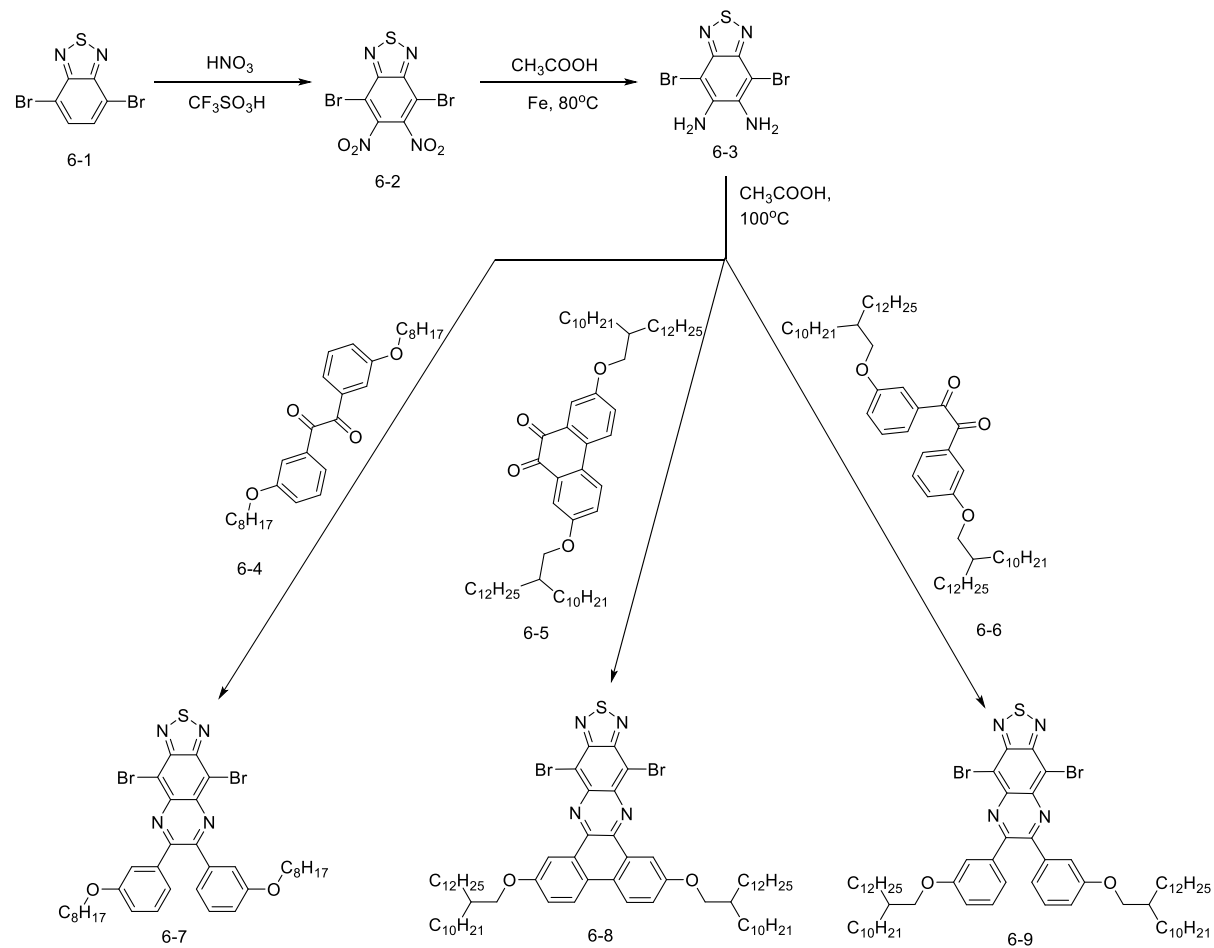
Detailed synthetic routes of polymers described in Chapter 5:



## Appendix II

Synthetic routes for the monomers described in Chapter 6:

Compound 6-4 was synthesized by Timothy Steckler, Chalmers. Compounds 6-5 and 6-6 were synthesized by Desta Antenehe Gedefaw, Chalmers.



# Acknowledgements

---

First, I would like to express my sincere gratitude to my supervisor Dr. Ergang Wang and co-supervisor Prof. Mats Andersson, for employing me as a Ph.D. student and for all the patient guidance through the past four years. Especially thanks to my supervisor for the edification in work and life.

I would like to thank my former and present group members, Tao for the help to introduce me to the lab; Desta for providing regents and sharing his experience; Petri for being helpful with work and reports through our project, and particularly thankful to his excellent function as GPS during all our business trips; Cedrik for reading my thesis and helpful suggestions; Kim, Zewdneh and Birhan for all the nice discussions. Special thanks to Xiaofeng, who helped me with my research through my PhD studies. I am grateful to all the help I got from my colleagues on 8<sup>th</sup> floor. Particularly thanks to Tina for helping me struggle through my first lab teaching course; Jonas for teaching me draw wonderful figures, Mattias for helping me with DSC measurements, and Anders Mårtensson for helping me with IR measurements and measuring GPC for me through my Ph.D. My nice and caring officemates Sandra, Mariza and Kajsa. Many thanks as well to Frida and Lotta, who are always patient and helpful with my questions and problems.

Thank OSNIRO project for funding my research and enabling me to go to visit other universities and research institutes during my Ph.D. study. I would like to extend my thanks to Deping for all the instructions to work in the device lab in Linköping University. I am grateful with all the help from Dr. Sybille Allard, Sebnem, Amaranda and Kai during my visit in the University of Wuppertal. Thanks to Cindy and Sandro at Siemens for a wonderful experience in Erlangen, Germany. I have been in Eindhoven University of Technology for more than seven months during my Ph.D. study. I would like to express my deep gratitude to Prof. Janssen for all the stimulating discussions. And I would like to thank all the group members for making my visit a wonderful journey. Special thanks to Giulio, Junke, Stefan, Martijn, Koen, Mengmeng, Mike, Bardo, Chunhui, Robin, Ruurd, Fallon, Aart, Marco and Wijnand for helping me out. Especially thanks to Dario for the training in the device lab and being helpful through my time there. A big thank to Margot, who makes my visit run smoothly and helps me with any problem occurring during my stay. And my research cannot be conducted without all the help from the collaborators. Thank you all! Special thanks to Wei Zhang for all the TRPL measurements, Xiangyi Meng for all the GIWAX measurements, and Prof. Mammo for thoroughly going through my thesis.

Four years' studying in Sweden has changed me in so many positive ways. Many thanks to my supportive friends in Gothenburg: Bo, Lanlan, Xin, Gaowa, Zhihang, Liangjian, Liyang and Wenjing. A special thanks to my family. 感谢我的爸爸妈妈对我无条件的支持，爱和关怀。尽管中国与瑞典有七个小时的时差，在我孤单和心情低落的时候，你们总在那里。我爱你们！Thanks to my parents-in-law for all the caring I received and being the best parents-in-law I can expect. In the end, I want to thank my husband, who is always my support in all the situations I have been through. Thank you for being my sunshine in the dark Swedish winter. I love you!